Wesleyan University Physics Department

Signatures of Phase Transition in Wave Dynamics of Complex Systems

by

Gim Seng Ng

Class of 2008

A thesis submitted to the
faculty of Wesleyan University
in partial fulfillment of the requirements for the
Degree of Bachelor of Arts
with Departmental Honors in Physics

Middletown, Connecticut April, 2008

Abstract

This thesis investigates wave dynamics and stability (against small perturbations or interactions) of complex systems where phase transition from localized to delocalized behavior can be achieved by changing an external or internal parameter. The main emphasis is on: (a) the stability of dynamics (under perturbed time-reversal experiments) of systems at a metal-to-insulator transition (MIT), (b) the effects of interaction-induced nonlinearity on wavepacket dynamics of systems at a MIT and (c) the statistical properties of current relaxation of systems where a nonlinearity-induced localization-delocalization phase transition occurs.

Acknowledgments

This work would not have been possible without all the great people around me. I would like to thank Tsampikos Kottos for his passion for physics, dedication to teaching, inspiring ideas, and being a mentor more than anything a student could ever wish for.

I owe it to Joshua Bodyfelt and Moritz Hiller for having 'initiated' me to the world of computational physics, and all their help throughout the years. I also want to thank Carl West, Holger Hennig, Ragnar Fleischmann, and Tomaz Prozen for fruitful collaborations that have taught me a lot. I would like to thank Theo Geisel and his institute members for my hospitable stays during the past few summers. I would like to thank all the physics professors in the department. I have been fortunate enough to have learned a great deal from each one of them.

I would like to thank the Wesleyan Freeman Asian Scholarship Program for providing me with the financial support to study at Wesleyan. I also want to thank all the friends that have supported me in various ways. I thank my family for their constant support. Finally, I would like to acknowledge Wesleyan University, the USA Israel Binational Science Foundation (BSF) and the DFG Forschergruppe 760 for their financial support.

Contents

List of Figures

Chapter 1

Introduction

Propagation of waves in complex media (natural or man-made) is an interdisciplinary problem of great theoretical and applied interest. It covers diverse areas ranging from light propagation in fog or clouds, to electronic, electromagnetic and atomic-matter waves, used to transmit energy and information, as well as to control, probe and image our world. Despite this diversity of physical systems involving different types of waves and various interactions among them, their common characteristics provide a framework for understanding wave propagation and often point to new applications.

Although propagation of waves through a random medium could be naively thought of as a simple diffusive process, interference effects give us richer phenomena and deeper physics. A very important consequence of interference effects in a random medium is *localization*, i.e. the existence of an exponentially high concentration of wave density in a certain region in space. In fact, localization phenomena also arise from other mechanisms, such as chaotic dynamics exhibited by deterministic systems, where the origin of localization comes from chaos. Another source of localization is associated with the interplay of nonlinearity and discreteness of translationally invariant lattices. In this case, spatially localized, time-periodic solutions can be created (called discrete breathers) and lead to halt of transport.

This work focuses on the study of wave dynamics and its stability to small perturbations in complex systems, where localization phenomena play a prominent role. As an overarching theme, we aim to search for signatures of criticality (which originate from localized-delocalized transitions) in the framework of fidelity studies, wavepacket dynamics, and current relaxation in complex media with absorbing boundaries. We will establish a link between the multifractal dimension and fidelity decay at the metal-insulator transition, as well as study the role of multifractality in the spreading of wavepackets of critical systems in the presence of nonlinearity. Finally, in the case of leaking nonlinear lattices, we present a novel phenomenon associated with the existence of intrinsic localized modes – the discrete breathers – supported by such systems, namely we find that the current decays in avalanches, whose sizes show a scale-free statistics similar to macroscopic systems with self-organized critical behavior [4].

The structure of this thesis is as follows:

- In Chapter 2, we will briefly review background physics in the field. In particular, we will introduce the Anderson localization and the metal-insulator transition in disordered systems. The subjects of quantum chaos and dynamical localization will then follow, with a discussion on Random Matrix Theory (RMT). This chapter will end with a brief introduction to discrete breathers, which appear in discrete nonlinear lattices.

- In Chapter 3, we will introduce the Wigner Lorentzian Random Matrix ensemble which describes systems at criticality. We will use this ensemble to understand the behavior of fidelity (which is a measure of quantum stability) and identify the traces of a metal-insulator transition (MIT) in this dynamical observable [1].

- In Chapter 4, we will study wavepacket spreading in critical systems with nonlinearity. Our analysis will rely on the nonlinear Harper model, which for appropriate parameter values possesses a MIT. We will find the critical nonlinearity above which the anomalous diffusion (shown by the linear system) at the tran-

sition point is altered, and provide a simple theoretical model that explains the emerging dynamics [2].

- Chapter 5 deals with dynamics of BECs in leaking optical lattices [3]. This system is described by the Discrete Nonlinear Schrödinger Equation (DNLSE) with absorbing boundaries. Such a model allows discrete breathers as solutions. We will study the role of discrete breathers in the decay process of the atomic population. Specifically, we will show that due to their existence, the atomic population (outgoing atomic current) decays in avalanches which (for appropriate nonlinearity strength) follow a scale-free distribution. This behavior is a clear indication of a phase transition [4]. We will develop a physical understanding of the avalanche's statistics by studying the hierarchical structure of islands of a mixed phase space in a reduced system.

- Finally, in Chapter 6 we summarize the main points of this work and discuss some further perspectives.

Chapter 2

Overview: Systems with Delocalization-to-Localization Phase Transition

In low temperature crystalline solids, Bloch theory describes an electron moving in a periodic lattice[1]. The wave function of the electron (called the Bloch wave) is the product of a periodic function, which reflects the spatial periodicity of the lattice, with a plane wave. Such wave functions are extended over the whole lattice, i.e. the spatial probability of finding the electron is the same over the entire crystal. Since extended states contribute to transport of electrons, they naturally lead to metallic behavior of the medium.

However, random arrangements of atoms or molecules are the rule rather than the exception in realistic systems. Noncrystalline materials, for example amorphous metals and semiconductors, no longer possess lattice periodicity – hence Bloch's theorem is no longer valid. In fact, when the effect of disorder is dominant, the electron states are

[1] See any standard solid-state textbook, for e.g. Ref. [5].

exponentially localized in (real) space. In such a situation, the localized states prevent transport of electrons and lead to insulating behavior. This localization phenemonon is called *Anderson Localization* [6]. In fact, depending on the dimensionality of the system, one can induce a phase transition from a metallic to an insulating behavior by tuning the degree or the strength of randomness. Such a phase transition is called *Metal-Insulator Transition* (MIT) and was at the heart of solid state research activity during the past 50 years.

Anderson localization is a wave interference phenomenon and as such is not unique to electronic (quantum wave) systems. In fact, classical waves (such as microwaves or acoustic waves) in random media can show Anderson localization as well [7]. Despite being a generic wave phenomenon, Anderson localization is very sensitive to external noise and one needs to preserve the phase coherence of the system in order to keep intact the delicate wave interference phenomena that are responsible for the localization phenomenon. In fact, this was why Anderson localization was not observed experimentally. However, recent experimental achievements in the mesoscopic scale (where phase-coherence is preserved) have allowed us to probe wave localization and investigate its emergence as the degree of complexity or randomness of the potential is increased.

Until recently, it was argued that a necessary condition to observe Anderson localization is that the medium under investigation has to possess some degree of randomness. A surprising result came about 25 years ago from a subfield of mathematical physics now known as quantum chaos. It was found that classically chaotic systems, upon quantization, show the same type of wave interference phenomena which lead to suppression of classical (chaotic) diffusion and the appearance of localization albeit in energy space (instead of configuration space where Anderson localization is observed) [8]. This localization effect is known as *dynamical localization* in order to distinguish its dynamical origin from that of a disordered system.

However, disorder and chaos are not the only mechanisms that lead to localization of

wavefunctions. Another source of localization is nonlinearity [9]. It is often the case that when interaction effects are considered, nonlinearity emerges in the equations of motion of the system. For example, in the Holstein model the electron-phonon interaction is introduced as a nonlinear term in the Schrödinger equation [9]. Another example comes from optical waveguides [9,10] in which propagating media may have a nonlinear dielectric coefficient (Kerr media [11]) while a third example is the mean-field description of Bose-Einstein Condensates loaded in an optical lattice, in which case the interatomic interaction translates into nonlinearity [12]. All of the systems mentioned above can be described by a unified mathematical equation – *the Discrete Nonlinear Schrödinger Equation* (DNLSE).

In this chapter, we will review the background physics of localization in disordered, chaotic and discrete nonlinear systems. The theory of Anderson localization will be the framework to describe disorder-induced localization whereas the kicked rotor will be a prototype model to illustrate dynamical localization through chaos. Due to its ubiquity, the DNLSE will be used as our representative equation of a discrete nonlinear system to discuss nonlinearity-induced localization.

2.1 Disordered Systems and Transition from Metal to Insulator

In 1958, Anderson proposed that strong enough disorder can halt the propagating waves and thus stop the diffusion of the wave through a random medium [6]. In the context of crystalline solids, this phenomenon translates into electron localization. Prior to Anderson's work, it was commonly thought that scattering by a random potential would cause Bloch waves to lose phase coherence on the length scale of the mean free path, but the wave function was expected to stay extended throughout the sample, leading to Ohmic behavior in the conductance. Therefore, Anderson's proposal was revolutionary,

contradicting what was widely believed [13].

In one dimension, it has been proven rigorously that the states of a random medium become localized for an infinitesimal amount of disorder [14–16] and it has been shown through one-parameter scaling theory that the same applies to two-dimensional systems [16]. For $d > 2$ there exists some critical disorder above which all electron states will be localized, i.e. there exists a metal-insulator transition [6, 17–23]. The formation of localized states, taking orthogonalization with different states into account, has presumably some (not yet fully understood) similarities to bound state formation [24]. For example, both happen in 1D and 2D, while in 3D there needs to be a critical disorder or potential depth.

In Anderson's paper, a perturbation theory (locator expansion) for the self-energy was constructed, taking the uncoupled sites as a zero-th order problem and the coupling as the perturbation. Anderson proved that for large enough values of the dimensionless ratio between the on-site potential mismatch and the tunneling rate, this perturbation theory converges 'in probability'. On a heuristic level, this means that starting from an initial site, the contributions of very distant sites fall off sufficiently strongly and thus the wavefunctions remain localized around their center of localization.

Although Anderson's seminal work dates back to 1958, experimental realization of such an effect has been extremely difficult in atomic crystals. This is because electron-electron interaction is not negligible, and phonon modes (i.e. excitations of the lattice) are thermally excited. While the earlier work of Anderson was mainly on electronic systems, in 1984 Sajeev John reinterpreted the Anderson localization as a pure interference effect through multiple scattering [7]. This means that such phenomena are *generic* wave phenomena. Fig. 2.1 illustrates the basic ideas of the origin of localization as a result of interference phenomena due to multiple elastic scattering.

Subsequently any classical wave, such as an electromagnetic, acoustic or seismic wave, in principle could be trapped in a medium, given that the random scattering event is

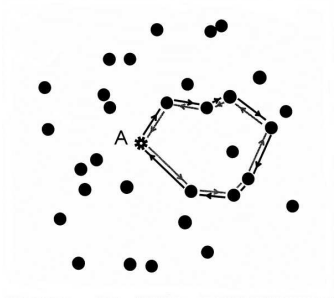

Figure 2.1: Localization effect through multiple elastic scattering. Consider a light source (or in general, any wave source) denoted as a star at position A in a disordered medium. The solid circles represent random scatterers. A random light path that returns back to the light source can be traced by the same path in two opposite directions. Waves that propapagate through these two paths will accumulate the same phase and thus interfere constructively. This then leads to a higher return probability to point A and thus reduces the mean free path because of lower probability to propagate away from A. With more random scatterers (disorder) one can see that light could eventually be 'trapped' in the sample, leading to localization. Figure from [27].

dominant. This provides a new ground for applications of Anderson localization theory, such as in the field of optics [7, 25]. Unlike electrons, photons do not interact with each other and thus give us a more controllable environment to study Anderson localization[2]. Experimental observation of Anderson localization has been realized in very strongly scattering semiconductor powders [27] and has recently been seen in a 2D photonic crystal [28] (see Fig. 2.2). In addition, hopes are high in its application towards random lasing with coherent feedback in order to amplify lasing gain [29–31].

[2]We point out that in optics there are other problems which are associated with absorption [26]. Recent advancement, however, have increased the Q-factor in optics experiments, thus allowing the observation of Anderson localization.

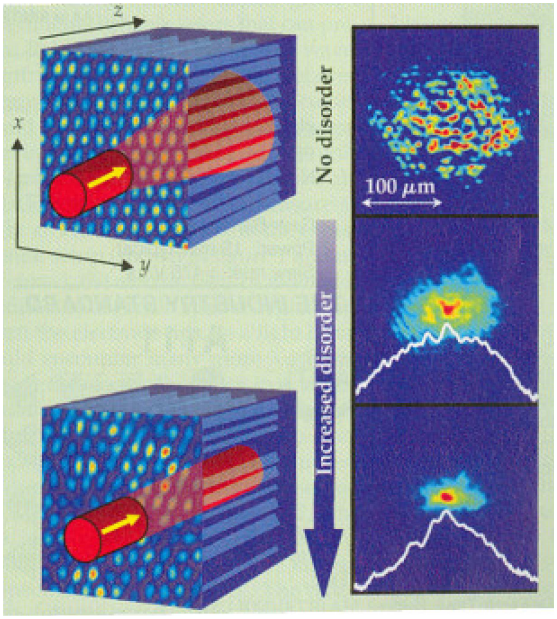

Figure 2.2: Anderson localization in a two-dimensional photonic lattice. In the x-y plane, a periodic variation in the refractive index is produced by the interference pattern of three intersecting plane waves, thus giving an ordered lattice (top left). A beam propagates through the sample in the z-direction, where the refractive index is uniform. Disorder is introduced through random fluctuations in the periodic refractive index (bottom left). The output profile (right) is imaged using a CCD camera. The output beam width (white line) is plotted on top of the image with the logarithm of intensity versus distance from the center of the beam. In the ordered lattice, the symmetry of the lattice is seen in the CCD image(top right). As disorder increases (from top to bottom), the output profile narrows and eventually decays exponentially (bottom right) – a signature of Anderson localization. Figure from [32], adapted from [28].

2.1.1 Anderson Model and Localization in 1D

We shall now proceed to prove the existence of *exponentially* localized states in the 1D Anderson model. Let us consider an electron in a lattice consisting of N sites, each site being placed a distance a apart from the other. Without loss of generality, we will assume that $a = 1$. In the tight-binding limit, the Hamiltonian reads

$$\mathbf{H} = \sum_{n=1}^{N} \epsilon_n |n\rangle \langle n| + T \sum_{n=1}^{n=N} \sum_{,m \in n.n.} (|n\rangle \langle m| + |m\rangle \langle n|) \tag{2.1}$$

where ϵ_n is the on-site energy level (we assume one energy level per site), T is the hopping matrix element connecting site n and nearest neighbor site m, and $|n\rangle$ is the orbital state (or the Wannier state) at site n. In the case where ϵ_n is periodic, the eigenfunctions are the Bloch waves, yielding extended wave functions.

For a disordered system, the on-site energy ϵ_n is randomly chosen for each site n from an uniform distribution of width W. In this case, Eq. (2.1) is called the Anderson model.

We expand a wavefunction $|\Psi\rangle$ in the basis of $|n\rangle$: $|\Psi\rangle = \sum_n \psi_n |n\rangle$ and use $\mathbf{H}|\Psi\rangle = E|\Psi\rangle$ to find the amplitude ψ_n associated with the eigenfunction of energy E

$$E\psi_n = \epsilon_n \psi_n + T \sum_{m \in n.n.} \psi_m. \tag{2.2}$$

We set $T = 1$ for the sake of convenience, and rearrange the 1D version of Eq. (2.2) into

$$\psi_{n+1} = (E - \epsilon_n)\psi_n - \psi_{n-1}. \tag{2.3}$$

These equations can be analyzed through the transfer matrix formalism by writing Eq. (2.3) in matrix form

$$\mathbf{u_{n+1}} = \mathbf{T_n u_n}, \tag{2.4}$$

where

$$\mathbf{T_n} = \begin{pmatrix} E - \epsilon_n & -1 \\ 1 & 0 \end{pmatrix} \quad \text{and} \quad \mathbf{u_n} = \begin{pmatrix} \psi_n \\ \psi_{n-1}. \end{pmatrix} \tag{2.5}$$

Through successive application of $\mathbf{T_n}$ to an inital vector $\mathbf{u_1}$, we can construct the total wavefunction associated with an energy E, i.e.

$$\mathbf{u_{n+1}} = \tilde{\mathbf{T}}_\mathbf{n}\mathbf{u_1} \quad \text{where} \quad \tilde{\mathbf{T}}_\mathbf{n} = \mathbf{T_n} \cdot \mathbf{T_{n-1}} \cdot \ldots \cdot \mathbf{T_1}. \tag{2.6}$$

Let us define the following quantity γ, called the 'inverse localization length',

$$\gamma \equiv \lim_{n\to\infty} \frac{1}{n} \ln ||\mathbf{u_n}|| > 0 \tag{2.7}$$

Since $\tilde{\mathbf{T}}_\mathbf{n}$ is a product of unimodular random matrices, Furstenberg's theorem [33] guarantees the existence of γ. For arbitrary boundary condition, this leads to exponential growth of wavefunctions and gives solutions that are not normalizable. Seeking physical states, i.e. normalizable wavefunctions, let us take a finite long chain and start applying the transfer matrix from both ends with arbitrary initial conditions and with arbitary energy E. In general, the wave function will grow exponentially away from the ends. Suitable choices for initial conditions and energies can be found so that a wavefunction iterated from the left matches one iterated from the right at some point n_0 on the lattice [15, 34]. This yields an eigenstate which is exponentially localized at site n_0

$$u_n = Cv(n)e^{-|n-n_0|/\xi}, \tag{2.8}$$

where $\xi = 1/\gamma$ is the localization length, $v(n)$ is a function that oscillates rapidly between values of unit magnitude and C is the normalization constant. For an example of an exponentially localized wave function, see the bottom-right inset of Fig. 2.2.

Furthermore, from the work of Thouless [35], γ is also related to an integral over the density of states through the Thouless formula

$$\gamma(E) = \int dE' \ln \left|E - E'\right| \rho(E') \ , \tag{2.9}$$

where $\rho(E')$ is the density of states.

In the special case of the Lloyd model [36], where the ϵ_n's are drawn from a Lorentzian distribution of width δ,

$$P(\epsilon_i) = \frac{\delta}{\pi\left(\epsilon_i^2 + \delta^2\right)} \ , \tag{2.10}$$

the inverse localization length is exactly known and is given by [35]

$$\cosh\gamma = \frac{1}{4}\left[\sqrt{(2+E)^2+\delta^2} + \sqrt{(2-E)^2+\delta^2}\right]. \tag{2.11}$$

2.1.2 Geometry at the Metal-Insulator Transition: Multifractality and its Statistical Measures

Between the extrema of localized and extended systems flourishes very rich and interesting physics. At the metal-insulator transition, the eigenfunctions (and in some special cases, the energy spectra as well) are multifractal with strong fluctuations on all scales. These states are called 'critical states'. Physical systems that exhibit metal-insulator transition include disordered systems in $d > 2$ dimensions, two-dimensional systems in strong magnetic fields (quantum Hall transition), quasi-periodic 1D systems (e.g. the Harper model), and periodically kicked systems with a logarithmic potential singularity [37]. Examples of localized, critical and extended wave functions are shown in Fig. 2.3.

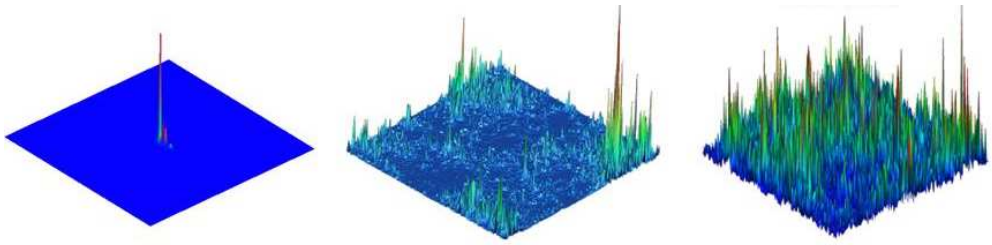

Figure 2.3: Examples of localized, critical and extended wave functions (from left to right) for a non-interacting electron moving in a random potential. Notice the fluctuations on all scales for the critical case. Figure from [38].

To understand the idea of wavefunction multifractality, we first need to discuss a measure of their dimensionality. We consider an electron wavefunction $\psi(\vec{r})$ embedded in a finite d-dimensional hypercube of hypervolume L^d. Then, the probability of finding the electron in a hypercube B_i of linear size $L_b = \lambda L$ is given by the box probability $P_i(\lambda)$ defined by

$$P_i(\lambda) = \int_{B_i} d^d r |\psi(\vec{r})|^2. \tag{2.12}$$

Let us cover the system with a mesh of $\tilde{N}(L_b, L)$ hypercubes, each of linear size L_b. Let $N(\lambda)$ be the number of boxes with non-zero $P_i(\lambda)$ for a given λ. Due to normalization of the probability function, $\sum_{i=1}^{N(\lambda)} P_i(\lambda) = 1$.

In the case of a single-fractal, this is just the box-counting method with $P_i(\lambda) = 1/N(\lambda)$ if there is non-zero probability in the hypercube B_i, or $P_i(\lambda) = 0$ if the hyperbuce B_i covers nothing. It is then immediate that $N(\lambda) = \lambda^{-D}$ with D being the box-counting dimension corresponding to the fractal dimension of a single-fractal (see Fig. 2.4 for an illustration of the box-counting method).

While D is useful in a single-fractal system, this quantity is not able to characterize critical wavefunctions. Box-counting method fails to capture the details within a covering box. For a wavefunction that has fluctuations on all scales, since the wavefunction is never exactly zero in any box, $N(\lambda) = \tilde{N}(\lambda)$. For example in the case of a 2D system, $N(\lambda) = \lambda^{-2}$ gives $D = 2$, the dimension of the embedded space – fails to extract anything interesting about a critical wave function.

To propose a useful measure of multifractality, let us first look at the scaling behavior of the average box probability in a single fractal. Normalization of the probability function gives the following scaling law for the average box probability

$$\langle P(\lambda) \rangle \equiv \frac{1}{N(\lambda)} \sum_{i=1}^{N(\lambda)} P_i(\lambda) \Rightarrow \langle P(\lambda) \rangle \propto \lambda^D \tag{2.13}$$

To capture more features of the wavefunction, let us consider the same averaging process for higher moments of the box probability. For systems where a length scale is absent,

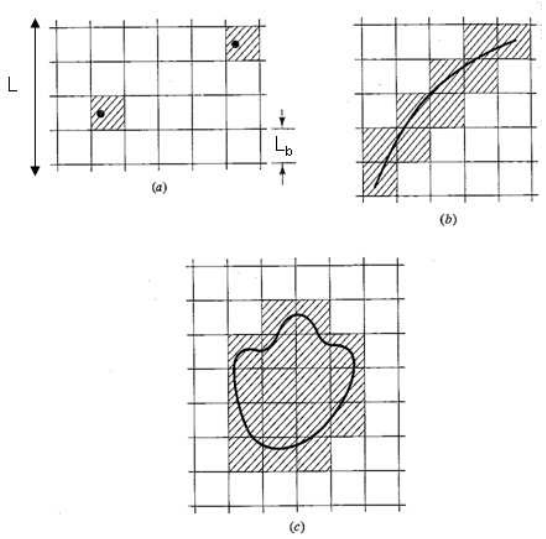

Figure 2.4: Illustration of the box-counting method for 2-dimensional covering. In (a), we have two separated points whereas in (b) a curve and in (c) an area enclosed by the solid line. We start with a mesh of $\tilde{N} = \lambda^{-2}$ boxes to cover the whole $L \times L$ area. Boxes that contain part of the 'figure' will be counted and yield $N(\lambda)$. For (a), it is trivial to see that since $N = \lambda^{-D}$ and $N = 2$ for all λ, then $D = 0$. As for (b), $N \approx l/L_b \propto \lambda^{-1}$ where l is the length of the curve. This gives $D = 1$. Similary, in (c) $N \approx A/L_b^2 \propto \lambda^{-2}$ where A is the area. This yields $D = 2$. Figure is taken from [39].

such that there are fluctuations at all scales, we assume that the moments $\langle P(\lambda)^q \rangle$ show a power-law scaling but with nontrivial exponents $\tau(q)$

$$\langle P^q(\lambda) \rangle \propto \lambda^{D+\tau(q)}. \tag{2.14}$$

For the special case of a uniform box probability distribution such that $P_i(\lambda) = 1/N(\lambda)$ for all i's, which corresponds to an extended wave function, we have

$$\langle P^q(\lambda) \rangle \propto N^{-q} = \lambda^{qD} \tag{2.15}$$

Comparing Eq. (2.14) and Eq. (2.15) yields $\tau(q) = (q-1)D$. Motivated by this, the generalized dimension $D(q)$ is defined such that the following holds

$$\tau(q) = (q-1)D(q). \tag{2.16}$$

With this definition, the fractal dimension D is just a special case of $D(q)$ with $D(0) = D$. Indeed, one can take this as a definition of a single-fractal system, i.e. a system which is characterized completely by one dimensionality only and thus $D(q) = D =$ constant for all q. In general, a multifractal wavefunction needs an infinite set of critical exponents $D(q)$ to fully capture all moments of the wave function and the fluctuations on all scales.

We shall now turn to the discussion of the correlation dimension $D_2^\psi \equiv D(2)$ because of its many applications and appearance in a variety of physical observables, such as the conductance distribution [40, 41], the anomalous spreading of a wave packet [42], the spatial dispersion of the diffusion coefficient [43–45], and the anomalous scaling of Wigner delay times [46].

Explicitly, D_2^ψ is defined through the second moment of the wavefunction, called the inverse participation number P_2

$$P_2 = \int d^d r |\psi(\vec{r})|^4 \propto L^{-D_2^\psi} \tag{2.17}$$

where d is the dimensionality of the embedded system and L the system size. In the case of a lattice, the inverse participation number is

$$P_2 = \sum_{n=1}^{N} |\psi_n|^4 \tag{2.18}$$

where $|\psi_n|^2$ is the probability of finding the particle at site n of a lattice with N sites.

It is perhaps more intuitive to discuss localization through the participation ratio P_R, which is defined as

$$P_R = \frac{1}{NP_2} \ . \tag{2.19}$$

The participation ratio gives an estimation of the fraction of sites where the wavefunction is significantly distributed.

2.2 Quantum Chaos and Dynamical Localization

There are, in general, two types of motions in classical Hamiltonian systems: *regular* and *chaotic* motion. Chaotic systems are often characterized by an *exponential* divergence of nearby trajectories, with the Lyapunov exponent measuring the degree of divergence. This leads to extreme sensitivity to initial conditions and rapid (exponential) loss of correlations. For regular systems, the rate of divergence may increase polynomially with time, but never exponentially – equivalently the Lyapunov exponent vanishes.

In a quantum system, however, the concept of trajectory is ill-defined due to the uncertainty principle. The notion of sensitivity to initial conditions fails due to unitarity and linearity of quantum evolution. Mathematically speaking, the overlap of two wavefunctions $|\phi(t)\rangle$ and $|\psi(t)\rangle$ remain independent of time, i.e. $|\langle\phi(t)\,|\psi(t)\,\rangle|^2 = |\langle\phi(0)\,|\psi(0)\rangle\,|^2$ under the same Hamiltonian evolution. Hence, the 'distance' stays constant throughout the evolution. There seems to be some trouble in defining chaos in quantum systems.

However, the famous Bohr correspondence principle says that classical and quantum mechanics must coincide in the limit of $\hbar \to 0$. Therefore, a quantum system with a classically chaotic counterpart should carry fingerprints of classical chaos in the semi-classical limit. This is exactly the goal in the study of *quantum chaos*: the search for *traces* of *classical chaos* in quantum mechanical systems.

Similar to the classification of a classical Hamiltonian system based on regularity of motion, quantum chaos has yielded criteria to distinguish between quantum systems with different underlying classical dynamics. For example, the notion of sensitivity to initial conditions is given an alternative perspective through the idea of sensitivity to slight changes in the Hamiltonian that describes the dynamics – an idea which is applicable in both classical and quantum systems. A measure of such sensitivity, called the *fidelity*, quantifies the overlap of an evolving wavefunction with the same wavefunction evolved under a slightly perturbed Hamiltonian. We shall introduce this quantity in Chapter 4 more formally, but one result that is worth mentioning is the appearance of the classical Lyapunov exponent in the quantum fidelity decay – a signature of the underlying classical chaos [47–49].

Another route in distinguishing a chaotic quantum system from a regular one comes from Random Matrix Theory (RMT). More elaborate discussion will be presented later in Sec. 2.2.3 but here we would like to mention that there exist universality classes in RMT that differentiate quantum systems with different types of motion in their classical counterparts. For a regular quantum system, the level spacing distribution exhibits a *Poisson* distribution whereas for a chaotic system, in general one finds a Wigner distribution [50]. The main difference lies in the fact that in the former case there exists no *repulsion* between the energy levels, whereas the Wigner distribution has vanishingly low probability of having very nearby energy levels (see Fig. 2.9).

Until recently, the connection between the statistical properties of the spectrum of quantum chaotic systems and RMT predictions was mainly based on numerical evidence. In

recent years, however, the creation of user-friendly models like the quantum graphs [51] and the advancement of semiclassical methods [52, 53] have allowed us to understand this relation more in depth. One of the remarkable achievements was the calculation of the two-point spectral correlation function in terms of periodic orbits and the appropriate evaluation of the contribution of families (of periodic orbits) defined according to their length spectrum [52, 54].

2.2.1 Kicked Rotor as a Prototype Model of Quantum Chaos

The kicked rotor (KR) is the prototype system of quantum chaos. It is defined through the Hamiltonian

$$\mathcal{H} = \mathcal{H}_0 + V \tag{2.20}$$

where $\mathcal{H}_0 = \frac{p^2}{2I}$ is the integrable part, which represents the kinetic energy – the 'free motion' – of a planar rotor with moment of inertia I and angular momentum p, whereas

$$V = \bar{K}\cos\theta \sum_{m\in\mathbb{Z}^+} \delta(t - mT) \tag{2.21}$$

is the nonlinear time-dependent perturbation in the form of a periodic kick with period T. The Hamiltonian in Eq. (2.20) represents a free rotor that is 'kicked' periodically by a gravitational field. For values of the gravitational constant $\bar{K}$ larger than some critical value $\bar{K}_c$, the classical dynamics is chaotic and the system absorbs energy in a diffusive manner. A schematic illustration of the KR is given in Fig. 2.5.

Using the angle θ and the angular momentum p as conjugate pairs in the Hamiltonian, we get the following equations of motion:

$$\begin{aligned} \dot{\theta} &= \frac{\partial \mathcal{H}}{\partial p} = \frac{p}{I} \\ \dot{p} &= -\frac{\partial \mathcal{H}}{\partial \theta} = \bar{K}\sin\theta \sum_{m\in\mathbb{Z}^+} \delta(t - mT) \end{aligned} \tag{2.22}$$

We can see from the above equations that the momentum stays constant except during the kicks. Therefore, θ varies linearly (with time) between consecutive kicks. Denoting

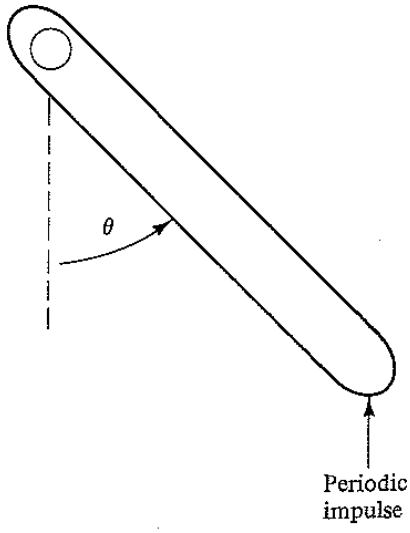

Figure 2.5: A schematic illustration of the kicked rotor. There is no friction in the pivot. The rotor rotates with angular position θ and is subjected to periodic kicks in the momentum. Figure from [39].

the angle and the momentum immediately after the m-th kick by θ_m and p_m, and integrating the delta-function during the $(m+1)$-th kick, we get

$$\begin{aligned} \theta_{m+1} &= (\theta_m + p_m\ T/I)\ \text{modulo}\ 2\pi\ , \\ p_{m+1} &= p_m + \bar{K}\sin\theta_{m+1}. \end{aligned} \tag{2.23}$$

Carrying out the transformation $pT/I \to p$, we then arrive at the standard map which depends only on *one* parameter $K = \bar{K}T/I$:

$$\begin{aligned} \theta_{m+1} &= (\theta_m + p_m)\ \text{modulo}\ 2\pi\ , \\ p_{m+1} &= p_m + K\sin\theta_{m+1}. \end{aligned} \tag{2.24}$$

For small K, the kicked rotor is integrable. As we increase K, KAM tori are destroyed[3]. There exists a critical value $K = K_c \approx 0.9716$ above which the last torus disappears

[3]For a discussion on KAM tori, we refer readers to standard classical chaos textbooks, such as Ref. [39].

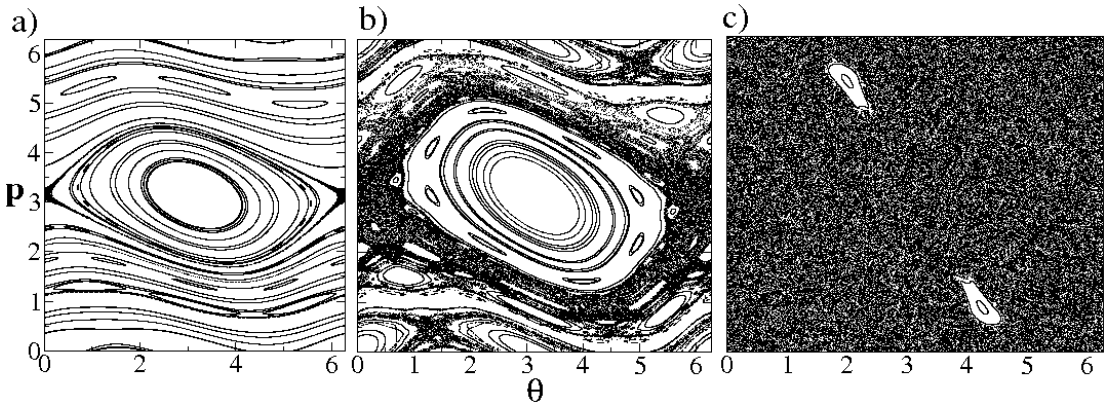

Figure 2.6: Phase space of the KR for (a) $K = 0.5$, (b) $K = 1.0$ and (c) $K = 5.0$. These figures plot p vs θ, both modulo 2π. Courtesy of Carl West.

and global diffusion in phase space sets in. Representative phase space plots of the KR are shown in Fig. 2.6.

In the large K limit, one can obtain the diffusion coefficient through random-phase approximation. In this regime, since the change in momentum is of order much larger than 2π, the θ_m's are uncorrelated due to the randomness in modulo (by 2π) of large numbers (see Eq. (2.24)). Averaging over intial conditions, one finds that after t iteration

$$\left\langle (p_t - p_0)^2 \right\rangle = K^2 \sum_{m=1}^{t} \left\langle \sin^2 \theta_m \right\rangle + K^2 \sum_{m \neq m'} \left\langle \sin\theta_m \sin\theta_{m'} \right\rangle = \frac{K^2}{2} t \tag{2.25}$$

with diffusion coefficient

$$D_\infty = \frac{K^2}{2}. \tag{2.26}$$

In contrast, the quantum kicked rotor, which we will discuss next, absorbs energy more slowly after some 'break time' (see Fig. 2.7). This intriguing effect is termed *dynamical localization*. Experiments have realized the quantum kicked rotor using atoms in a pulsed optical lattice and confirmed the effect of dynamical localization [55, 56] (see Fig. 2.7).

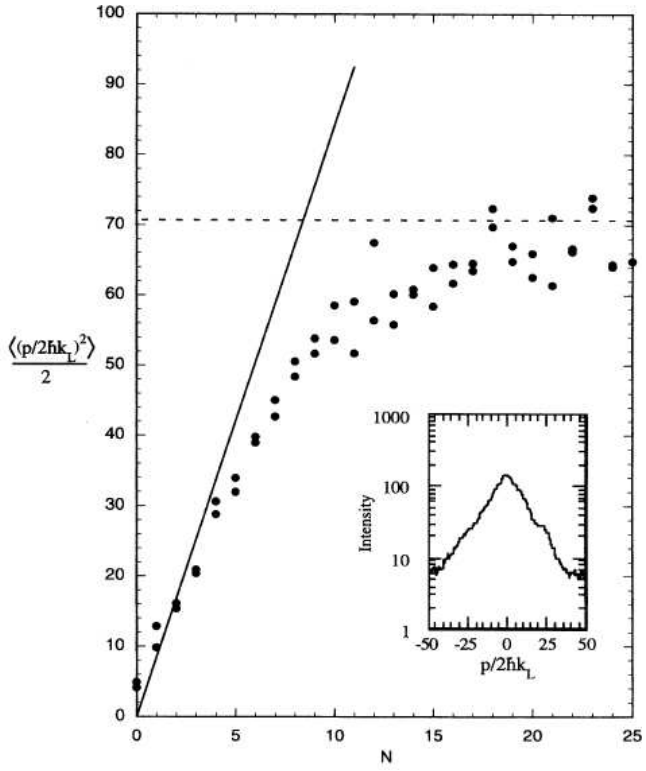

Figure 2.7: Experimental realization of the quantum kicked rotor using atoms in a pulsed optical lattice. The figure plots energy $\left\langle (p/2\hbar k_L)^2 \right\rangle /2$ vs number of kicks N. The solid dots are the experimental results whereas the solid line is the prediction from classical diffusion. The dashed line is the saturation value computed from the theoretical localization length ξ. The inset shows an experimentally observed localized state. Figure from [55].

2.2.2 Kicked Rotor and Anderson Localization

While there exists no rigorous proof of dynamical localization of the quantum kicked rotor, there exists a suggestive map from the quantum kicked rotor to a pseudo-Anderson model – a variant of the Anderson model with *pseudo-randomness*. We shall present this mapping following the discussion in Ref. [57].

The quantum kicked rotor is obtained by the substitution $p \to \hbar\hat{n} = -i\hbar\partial/\partial\theta$, where the commutator is $[\hat{n}, \hat{\theta}] = -i\hbar$. This leads to the Hamiltonian

$$\hat{\mathcal{H}} = \frac{\hbar^2}{2I}\hat{n}^2 + \bar{K}\cos\hat{\theta}\sum_m \delta(t - mT) \ . \tag{2.27}$$

Carrying out the transformation $t/T \to t$, $\mathcal{H}/(\hbar/T) \to \mathcal{H}$, we get

$$\hat{\mathcal{H}} = \frac{1}{2}\tau\hat{n}^2 + k\cos\hat{\theta}\sum_m \delta(t - m) \ , \tag{2.28}$$

with $\tau = \hbar T/I$ and $k = \bar{K}/\hbar$. The classical limit corresponds to taking $k \to \infty$ and $\tau \to 0$, but keeping $k\tau = K$ constant to preserve the underlying classical dynamics.

Since the KR Hamiltonian is periodic in time, we introduce the Floquet operator, which is a unitary time evolution operator that transforms a wave function $|\psi(\theta, t)\rangle$ from t to $t + 1$

$$\hat{U}\,|\psi(\theta, t)\rangle = |\psi(\theta, t + 1)\rangle \ . \tag{2.29}$$

The time t in Eq. (2.29) is the time just before a kick. In the case of the quantum KR, the evolution operator (i.e. the Floquet operator) is[4]

$$\hat{U} = e^{-i\mathcal{H}_0}e^{-iV(\theta)}. \tag{2.30}$$

where $H_0 = \frac{1}{2}\tau n^2$ and $V(\theta) = k\cos\theta$.

Let us define the eigenstates of $\hat{U}$ to be the quasi-energy states $|\psi_w(\theta, t)\rangle$ with the corresponding eigenvalues w (called the quasi-energies) satisfying the following equation

[4]For the sake of convenience, from now on we will drop the hat notation on operators.

[58]

$$\hat{U}\left|\psi_w(\theta,t)\right\rangle = e^{-iw}\left|\psi_w(\theta,t)\right\rangle \ . \tag{2.31}$$

In an exact analogue with the Bloch wave in a spatial periodic lattice, due to the temporal periodicity, the $|\psi_w\rangle$ (which is called the Bloch-Floquet state) can be written as [58]

$$\left|\psi_w(\theta,t)\right\rangle = e^{-iwt}\left|u_w(\theta,t)\right\rangle \tag{2.32}$$

with $|u_w\rangle$ having the same periodicity as the Hamiltonian, i.e. $|u_w(\theta,t)\rangle = |u_w(\theta,t+1)\rangle$.

We can expand any evolving function $|\psi(\theta,t)\rangle$ in terms of the quasi-energy states [58]

$$\left|\psi(\theta,t)\right\rangle = \sum_w A_w \left|\psi_w(\theta,t)\right\rangle \ . \tag{2.33}$$

Therefore, the dynamics are completely determined by the nature of the quasi-energy states (or the states $|u_w\rangle$) in the same way that the eigenvalues and eigenvectors of a Hamiltonian characterize the dynamics of a system in which energy is conserved.

Next, we shall derive an equation for their projections onto the angular-momentum states, i.e. the eigenstates of $\mathcal{H}_0$. Let us define $|u_w^-\rangle$ and $|u_w^+\rangle$ as the states of $|u_w\rangle$ just before and after a kick, respectively. The corresponding quasi-energy state then reads $|\psi_w^\pm\rangle = e^{-iwt}|u_w^\pm\rangle$.

We now divide the problem into two parts: during two consecutive kicks and during a particular kick. Between a kick at $t = m$ and the consecutive one at $t = m+1$, the evolution is given by

$$\left|\psi_w^-(\theta,t=m+1)\right\rangle = e^{-i\mathcal{H}_0}\left|\psi_w^+(\theta,t=m)\right\rangle, \tag{2.34}$$

and thus

$$\left|u_w^-(\theta,t=m+1)\right\rangle = e^{i(w-\mathcal{H}_0)}\left|u_w^+(\theta,t=m)\right\rangle. \tag{2.35}$$

Projecting these states onto an angular momentum state $|n\rangle$, one obtains

$$u_n^-(t=m+1) = \exp\left[i\left(w-\frac{1}{2}\tau n^2\right)\right]u_n^+(t=m) \tag{2.36}$$

with $u_n^{\pm}(t=m) \equiv \langle n|u_w^{\pm}(\theta, t=m)\rangle$.

During a kick at time $t = m$, the state is evolved under $V(\theta)$ and the state right after the kick is

$$\left|u_w^{+}(\theta, m)\right\rangle = e^{-iV(\theta)} \left|u_w^{-}(\theta, m)\right\rangle. \tag{2.37}$$

For the sake of convenience, we introduce a unitary Hermitian operator W [57]

$$W(\theta) = -\tan\left(V(\theta)/2\right) \tag{2.38}$$

so that

$$\exp\left[-iV(\theta)\right] = \frac{1+iW(\theta)}{1-iW(\theta)}. \tag{2.39}$$

We then define

$$|\bar{u}(\theta, m)\rangle = \frac{1}{2}\left[\left|u_w^{+}(\theta, m)\right\rangle + \left|u_w^{-}(\theta, m)\right\rangle\right]. \tag{2.40}$$

Putting Eq. (2.37), Eq. (2.39) and Eq. (2.40) together yields [57]

$$\begin{aligned} \left|u_w^{+}(\theta)\right\rangle &= |\bar{u}(\theta)\rangle\left(1+iW(\theta)\right) \\ \left|u_w^{-}(\theta)\right\rangle &= |\bar{u}(\theta)\rangle\left(1-iW(\theta)\right) \end{aligned} \tag{2.41}$$

Projecting these equations onto the angular momentum basis and after some straightforward manipulations, we arrive at

$$E\bar{u}_n = T_n\bar{u}_n + \sum_{r\neq n} W_{n-r}\bar{u}_r \tag{2.42}$$

where $\bar{u}_n$, W_n are the respective projections of $\bar{u}$ and W onto the angular momentum basis, $E = -W_0$, and

$$T_n = \tan\left[\frac{1}{2}\left(w - \frac{1}{2}\tau n^2\right)\right]. \tag{2.43}$$

Immediately, one notices the similarity of Eq. (2.42) with the Anderson model in Eq. (2.2), if one were to interpret T_n as the diagonal on-site energy, and W_{n-r} as the hopping matrix elements. However, unlike the Anderson model, the hopping term here

is not necessarily limited to nearest-neighbors, but is in general of some finite range [50]. Furthermore, T_n is not strictly random as in the Anderson model.

From Eq. (2.27), we note that all energy spacings of the unperturbed rotor are multiples of $\hbar^2/2I$, with corresponding frequencies multiples of $\tilde{\omega} = \hbar/2I$ and period multiples of $\tilde{T} = 4\pi I/\hbar$. Together with the definition of τ, one then obtains $\tau/4\pi = T/\tilde{T}$. This gives us the ratio between the period of the driving potential (i.e. the kick) T and the natural period of the rotor $\tilde{T}$. For rational values of $\tau/4\pi$ (i.e. $\tau/4\pi = r/q$, where r and q are integers), this is the quantum resonance case [59]. In this case, T_n is a periodic function of period q and hence from Bloch theory, we know that the quasi-energy states are extended in the momentum space.

For generic values of τ, where τ/π is a generic irrational number, the argument $w - \frac{1}{2}\tau n^2$ of the tangent in T_n is effective modulo π. According to a theorem of Weyl's [60], the sequence $w - \frac{1}{2}\tau n^2 \mod \pi$ is ergodic in the interval $I = [0, \pi]$ and covers this interval with uniform distribution. This means that the distribution of T_n will follow $\mathcal{P}(T_n)dT_n = dw/\pi$. Together with $dT_n/dw = 1 + T_n^2$, one obtains

$$\mathcal{P}(T_n) = \frac{1}{\pi\left(1 + T_n^2\right)} \ . \tag{2.44}$$

To push the analogue of the Anderson model further, if we replace the potential $V(\theta)$ in the KR with

$$V(\theta) = -2\arctan\left(\kappa\cos\theta - E\right) \ , \tag{2.45}$$

then we obtain the Lloyd model [36], which only has nearest-neighbour hopping.

For the sake of convenience, we drop the bars on $\bar{u}_n$ and turn Eq. (2.42) into

$$Eu_n = T_n u_n + \frac{1}{2}\kappa\left(u_{n+1} + u_{n-1}\right) \tag{2.46}$$

In Fig. 2.8, we compare the numerically evaluated localization length related to Eq. (2.46) and the theoretical results for the Lloyd model. The agreement is excellent, providing strong evidence that in this case, pseudo-randomness (in the T_n's) is enough to give rise to localization.

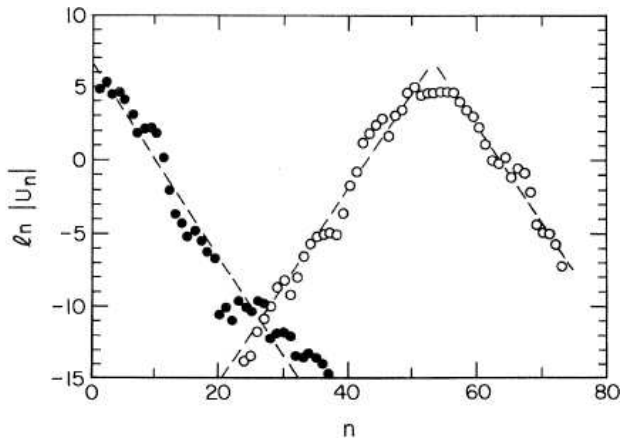

Figure 2.8: Two quasi-energy states for the Lloyd model. The circles are the numerical results whereas the dashed lines are the theoretical fits calculated from the localization length of the Lloyd model. Figure is from [57].

2.2.3 Random Matrix Theory

The spectra of simple molecules like atomic hydrogen and helium have been well understood using quantum mechanics. However, the application of quantum mechanics for heavier elements seems to be an enormously complicated task. One of the ways to study the spectral properties of such systems is to build models with *minimum* information without losing the *essential* physics. This is exactly the main principle behind Random Matrix Theory (RMT).

It was Wigner who first proposed the use of random matrix ensembles to model the extremely complicated Hamiltonian matrix of heavy nuclei [61]. A random matrix ensemble consists of square matrices H of size $n \times n$ (eventually we want to take the limit of $n \to \infty$), whose elements H_{nm} are obtained from a Gaussian distribution with zero mean and variance

$$\left\langle |H_{nm}|^2 \right\rangle = 1 + \delta_{nm}. \tag{2.47}$$

Additional symmetry requirements on the Gaussian random matrix ensemble give rise to the concept of *universality classes*. This corresponds to the classification of systems

into those with broken/unbroken time-reversal symmetry and those with/without spin-1/2 interaction. In matrix mechanics, this translates into invariance under orthogonal, unitary and symplectic transformations, leading to the three commonly known Gaussian ensembles that are of interest: the Gaussian Orthogonal Ensemble (GOE), the Gaussian Unitary Ensemble (GUE) and the Gaussian Sympletic Ensemble (GSE)[5].

The power of RMT lies on the idea of universality: if a generic quantum system falls under one of the universality classes, certain statistical properties of the spectrum will be described according to some universal predictions, regardless of microscopic system details. To date, there has been a plethora of numerical and experimental evidence supporting universality [63]. One of the successes of RMT is its correct prediction of the distribution of the energy level spacings

$$S_n = \frac{E_{n+1} - E_n}{\Delta(E)} \ , \tag{2.48}$$

where the E_n's are the ordered eigenenergies and $\Delta(E)$ is the mean level spacing. This distribution is one of the simplest statistical quantities that is measurable in experiment.

Here, we present a summary of level spacing distributions for each of the RMT ensembles discussed above (see Appendix A for a derivation):

$$P(S) \propto \begin{cases} S^1 e^{-\frac{\pi}{4}S^2} & \text{GOE} \ , \\ S^2 e^{-\frac{4}{\pi}S^2} & \text{GUE} \ , \\ S^4 e^{-\frac{64}{9\pi}S^2} & \text{GSE} \ . \end{cases} \tag{2.49}$$

While the above distributions are applicable for chaotic systems, in the case of integrable systems, one can show that $P(S)$ follows a Poisson distribution i.e. $P(S) = e^{-S}$ (see Appendix A). Figure 2.9 shows examples of level distributions of different universality classes. The RMT cases are called the Wigner distributions. We also observe that while integrable systems do not exhibit level repulsion, the other universality classes show vanishing probability of finding nearby energy levels.

[5]In fact, in recent years 7 more ensembles were introduced (see Ref. [62]).

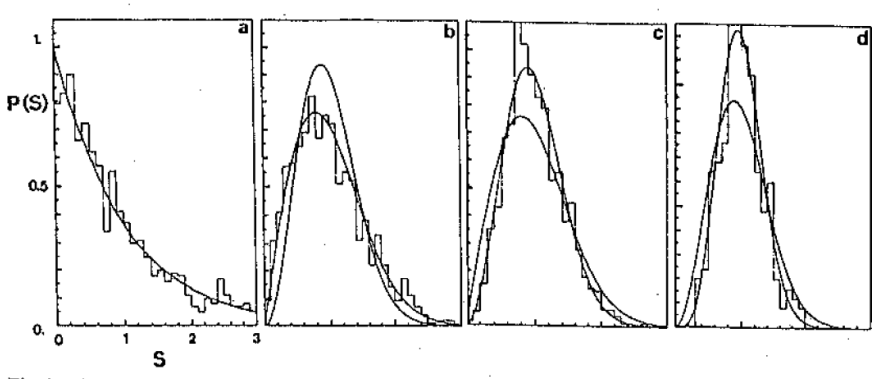

Figure 2.9: Level spacing distributions for kicked tops in (a) regular motion and (b-d) chaotic motion. The three curves on the right (b-d) correspond to different universality classes with (b) linear (GOE), (c) quadratic (GUE) and (d) quartic (GSE) level repulsion. Figure from [50]

Not only has RMT attracted a lot of attention in the framework of quantum chaos, its predictions could be extended to the studies of disordered systems as well [64]. In the metallic regime, the eigenstates of these systems are extended, and the statistical properties of their spectra are quite well described by the traditional RMT ensembles [65]. In particular, the level spacing distribution is very well fitted by the Wigner distribution of the appropriate symmetry class. Deep in the localized regime, the levels become uncorrelated leading to a Poissonian level spacing distribution and the eigenfunctions are exponentially localized. At the MIT, the eigenfunctions are critical, exhibiting multifractal structure characterized by strong fluctuations on all scales. The eigenvalue statistics are characterized by a new universal distribution [65, 66] and a new ensemble of random matrices was recently introduced to describe such systems [67]. We will introduce this ensemble in Chapter 3.

2.3 Discrete Breathers and Discrete Nonlinear Schrödinger Equation

One of the founders of nonlinear science, Stanislaw Ulam, once remarked that the use of the term 'nonlinear science' was like 'calling the bulk of zoology the study of non-elephants' [68]. This sharply captures the point that linear processes are usually the exception rather than the rule. Most realistic physical systems are indeed nonlinear [68]. On the other hand, the use of lattice geometry in physics is abundant. From the textbook example of crystalline solids in condensed matter to the recent use of optical lattices, careful manipulation of lattice stucture often yields new physical phenomena.

We have discussed localization phenomena in the context of solid-state physics and quantum chaos. In these cases, either disorder or chaos is needed to cause constructive interference that leads to spatial or dynamical localization. However, in an ordered lattice, there exist localized excitations that are due to the interplay of interaction-induced nonlinearity and discreteness. These are the *discrete breathers* (DBs), also known as *intrinsic localized modes* (ILMs).

A DB is a spatially localized, time-periodic, and stable excitation in extended, periodic, discrete nonlinear systems. To understand roughly the existence of breathers, let us consider the 'anti-continuum limit' [69], where we start with a set of uncoupled nonlinear oscillators. For simplicity's sake, let us restrict our discussion to the case of two classical nonlinear pendula. In the case where the amplitude of oscillation is small, we are back to the linear pendulum problem, where the period depends only on the length of the pendulum and gravity. However, when the amplitude gets larger, the period of the oscillation is, in general, dependent on the amplitude.

Now, we excite both pendula, so that the first pendulum is oscillating strongly relative to the second one. In this case, most of the energy is initially concentrated in the first oscillator. Since the frequency of a nonlinear oscillator is dependent on the amplitude,

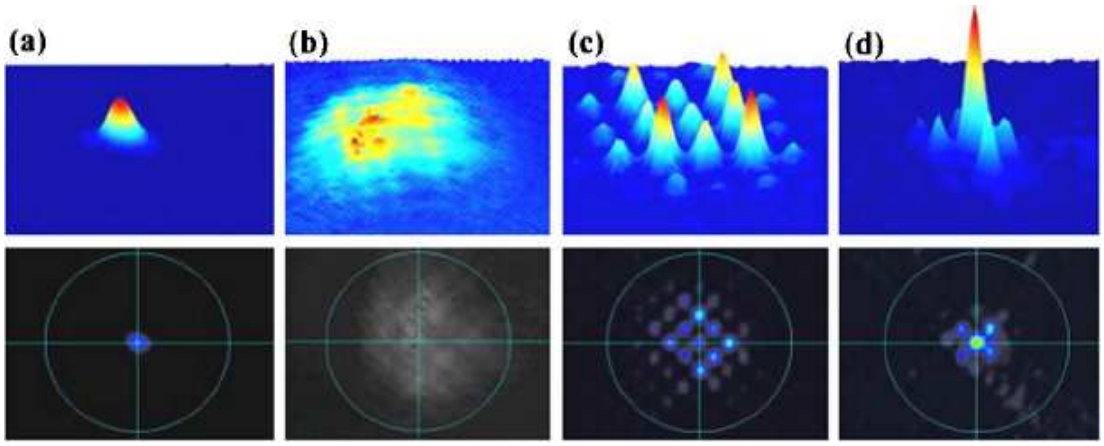

Figure 2.10: Experimental realization of DBs in a 2D photonic lattice, created by optical induction in a photorefractive crystal. A second laser beam provides the input, which is centered on a single site in the photonic lattice. The 3D intensity plots for the top figures show (a) the input intensity, (b) the linear diffraction output in the absence of a photonic lattice, (c) the discrete linear diffraction, induced by the photonic lattice for weak nonlinearity and (d) a DB that appers due to large nonlinearity. The bottom figures shows a 2D transverse patterns. Figure is taken from [71].

we can choose the frequency of the strongly oscillating pendulum to be incommensurate with the other pendulum. When we turn on the coupling, intuition suggests that transfer of energy from one to the other is extremely difficult or maybe even impossible. This is the basic idea of how nonlinearity supports localized solutions like the DBs.

Since the discovery of DBs in the late 1980s, many experimental observations of the DBs have been made in various physical systems, such as electronic and magnetic solids, microengineered structures including Josephson junctions and optical waveguide arrays, and laser-induced photonic crystals. Hopes are high in the applications of the DBs in all-optical logic and switching devices, BEC systems, and biopolymers [70]. Fig. 2.10 shows an example of DBs in a photonic lattice. For a comprehensive review on DBs, see [72].

In this work, we will investigate one of the most ubiquitous discrete nonlinear models –

the Discrete Nonlinear Schrödinger Equation (DNLSE):

$$i\frac{\partial \psi_n}{\partial t} = U|\psi_n|^2\psi_n + \epsilon_n\psi_n + V(\psi_{n-1} + \psi_{n+1}). \tag{2.50}$$

Indeed, the applications of the DNLSE are incredibly wide. For example, it can describe the interaction of a quantum mechanical particle with the phonon modes [73] and account for the energy transfer in proteins [74]. It has also been used in the description of wave motion in nonlinear optical waveguides [75] (see Appendix B). Perhaps the most recent and exciting of its applications is in the field of Bose-Einstein condensates (BEC) in optical lattices. The DNLSE turns out to be the classical version of the Bose-Hubbard Hamiltonian, which describes the many-body interacting bosons loaded in a deep optical lattice (see Apppendix C).

The existence of DBs in the DNLSE only adds to the excitement of new phenomena that are unique to discrete nonlinear systems. It is therefore of interest to study the effect of these localized modes on the transport properties of a DNLSE system. In Chapter 5, we shall explore and study in depth the dynamics of the DBs in leaking optical lattices and how they give rise to very rich and intriguing critical behavior.

Chapter 3

Quantum Stability of Critical Systems

Although Newtonian mechanics does not preclude the possibility of reversing a process by inverting the velocities of all particles combining a macroscopic system, our everyday experience tell us that this is impossible. A classical example is the process where an ice cube and a cup of boiling water turn into lukewarm water after some time. The reverse process, i.e. that of a cup of lukewarm water turning into boiling water with an ice cube, has not been observed in reality. This is the so-called reversibility paradox, which is usually attributed to Josef Loschmidt who questioned Boltzmann's monotonic approach towards equilibrium [76].

In this chapter, we will review the familiar explanations of irreversibility in classical physics using the ideas of *mixing* and *coarse graining*. We will introduce a measure of stability in the framework of fidelity, and give a summary of previous fidelity studies. The RMT ensemble of Wigner Lorentzian Random Matrices will be used as a model to study systems at a metal-insulator transition. We will study fidelity decay in different regimes of perturbation strengths and seek for the signatures of criticality in the fidelity

decay. Finally, this chapter will end with conclusions that sum up the main results of the study.

3.1 Fidelity as a Measure of Quantum Stability

Following the discussion in [77, 78], we now provide the explanations of irreversibiliy in classical physics. The central idea is that irreversible processes occupy such a small part of the phase space that one needs to have incredibly high control over the preparation – impossible to make happen in practice. To understand the notion of mixing in chaotic systems, let us consider two finite but fixed subsets V_1 and V_2 of a phase space, whose measures are fractions μ_1 and μ_2 of the total phase space respectively. Suppose that the distribution $f_1(p, q)$ is uniform in V_1 at time t_1 with $\int f_1 dV_1 = 1$. Then, for any time t_2 *sufficiently remote* from t_1 (in the future or in the past) and for sufficiently large μ_1 and μ_2, $\left|\int f_2 dV_2 - \mu_2\right| < \delta$ with arbitary small $\delta > 0$ regardless of where V_1 is. This is called *mixing*, which is a property of chaotic systems. A crude (but useful) rephrasing of mixing is that chaotic trajectories fill up the whole phase space if one waits long enough. Notice that the idea of mixing is *time symmetric*, so that by itself it can not explain irreversibility. It is also worth noting that the smaller δ, μ_1 or μ_2, the larger the time $|t_1 - t_2|$ needed for mixing.

In our ice cube example, μ_1 represents an ice cube plus boiling water while μ_2 represents the lukewarm water , with $\mu_1 \ll \mu_2 \approx 1$. With suitable value of the total energy, *almost* every evolution will lead to a cup of lukewarm water, with perhaps only extremely small inhomogeneties. Nonetheless, we *can*, conceptually, prepare the lukewarm water at time t_2, so that at a *later* time t_1, it will separate into ice cube and boiling water. However, this scenario requires a very special preparation (not just any cup of lukewarm water, but one with delicate correlations between all the molecules) and this preparation has a μ_2 so small that mixing will not yet be valid after the given *finite* time $t_1 - t_2$.

Furthermore, we may not be able to achieve such high-precision control over the preparation due to the coarseness of our instruments. This is the idea of *coarse graining*. Because of our instrumental limitations, we can not locate the initial state within such a small V_2 (i.e. with μ_2 so small that mixing has not yet ocurred after a finite $t_1 - t_2$). Therefore, we can not prepare the system at time t_2 so that after a finite time $t_1 - t_2$, it will be located with certainty in the desired small region V_1 of phase space. Thus, there are classical processes (e.g. from lukewarm water to an ice cube in boiling water) which can not be made to occur due to mixing and coarse-graining. What happens if we bring the ideas of mixing and coarse graining to the quantum world?

Due to the uncertainty principle, a distribution in phase space can not develop structures on scales which are smaller than $\hbar$. Therefore, the property of mixing has an ill-defined analogue in the quantum case. In addition, coarse graining seems to make no sense in the context where dynamical quantities occur with *discrete* values, such as that in quantum mechanics. In principle, it is possible to prepare arbitarily pure quantum states. Even with small error in the preparation of the initial state, the error will not grow because the Hamiltonian evolution is *unitary*. Initially neighbouring states remain close throughout the evolution since their scalar product is invariant.

To motivate a new idea of analyzing stability (and hence reversibility) that works both classically and quantum mechanically, Peres [77] proposed that instead of assuming that our preparations are marred by limited accuracy, we may assume that they are perfect, but on the other hand, the *Hamiltonian* is not *exactly* known. This is justifiable because in practice we can not perfectly insulate a physical system from its environment, e.g. from ambient fields (like electromagnetic or gravitational field) that are present in the lab. There is an unavoidable difference between the Hamiltonian $\mathbf{H}_1$ used for the forward evolution and $\mathbf{H}_2$ the time-reversed Hamiltonian. This difference is formally investigated through the *fidelity* , defined as:

$$F(t) \equiv |\left\langle \psi_0 \left| e^{iH_2 t} e^{-iH_1 t} \right| \psi_0 \right\rangle|^2; \quad \hbar = 1 \tag{3.1}$$

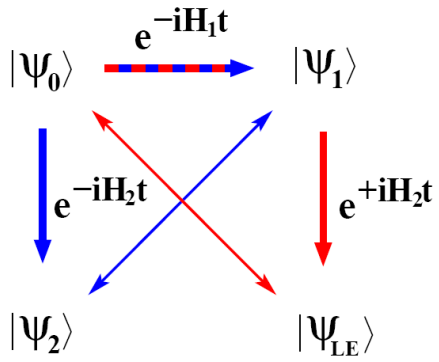

Figure 3.1: Schematic illustration of the two equivalent interpretations of fidelity. Here, $\mathbf{H_1}$ represents some forward unperturbed Hamiltonian and $\mathbf{H_2}$ the backward perturbed Hamiltonian. The absolute-value-square of the bracket between $|\psi_1\rangle$ and $|\psi_2\rangle$ yields the fidelity whereas the absolute-value-square of the result of bracketing $|\psi_0\rangle$ with $|\psi_{LE}\rangle$ gives the Loschmidt Echo, but the two end results are mathematically equivalent. Figure from [78].

where $\mathbf{H}_1$ and $\mathbf{H}_2 = \mathbf{H}_1 + x_\mathrm{e}\mathbf{B}$ represent the unperturbed Hamiltonian and its perturbed variant respectively, while $|\psi_0\rangle$ is an initial state. The Hamiltonian $\mathbf{B}$ represents a perturbation due to interaction with the environment, and x_e is an external parameter which controls the perturbation strength.

In fact, one can interpret fidelity in Eq. (3.1) in two equivalent ways (see Fig. 3.1). It can be considered as the overlap of an initial state $|\psi_0\rangle$ with the state $|\psi_{LE}\rangle$, where $|\psi_{LE}\rangle$ is obtained after a forward (in time) unperturbed evolution, followed by a backward (in time) perturbed evolution (the red path). Equivalently, it is the overlap of the state $|\psi_1\rangle$ obtained after a forward unperturbed evolution and the state $|\psi_2\rangle$ after a forward perturbed evolution (the blue path).

The first interpretation is the original proposal by Peres [77] to study quantum-classical correspondence and identify traces of classical (chaotic or integrable) dynamics. It is also inspired by nuclear magnetic resonance experiments which explore whether it is possible to evolve a complex system backwards in time under certain circumstances [79]. In this

context, fidelity is also known as the Loschmidt Echo (hence $|\psi_{LE}\rangle$), which is related to the *gedanken* experiment of the Boltzmann-Loschmidt controversy over the issue of the arrow of time [80].

The latter interpretation is closely linked to the concept of dephasing [81] in mesoscopic devices and coherent manipulation of a quantum state. Sustaining the coherence of a superposition of state vectors is at the heart of quantum parallelism in quantum computation schemes [82–84]. The role of fidelity in the context of dephasing will be discussed further in Appendix D.

The theory of fidelity [77] has been a subject of intensive research activity during the last years (for a recent review see [85]). This interest has been motivated by various areas of physics, ranging from atomic optics [86–88], microwaves [89] and elastic waves [90] to quantum information [84] and quantum chaos [47, 91–100]. It has been adopted as a standard measure for quantum reversibility and stability of quantum motion with respect to changes in an external parameter $x_{\rm e}$.

3.1.1 Previous Fidelity Studies and Critical Systems as a New Universality Class

For a quantum system with a classical chaotic counterpart, the decay of the fidelity depends on the strength of the perturbation parameter $x_{\rm e}$. Recent studies indicated that there are three strength regimes: the standard perturbative regime, the Fermi Golden Rule regime (FGR), and the nonperturbative regime. The first two can be described by Linear Response Theory (LRT) leading to a decay which depends on the perturbation strength $x_{\rm e}$ as

$$F(t) \sim e^{-(x_{\rm e}t)^2} \tag{3.2}$$

and

$$F(t) \sim e^{-x_{\rm e}^2 t} \tag{3.3}$$

respectively [91, 94, 95]. In the nonperturbative regime, the decay is

$$F(t) \sim e^{-\lambda t} \ , \tag{3.4}$$

with a rate that is perturbation independent and is given by the Lyapunov exponent λ of the underlying classical system [47, 91, 100].

The investigation of the fidelity has recently been extended to systems that have integrable classical dynamics. It was shown [92] that the decay follows a power law

$$F(t) \sim t^{-3d/2}, \tag{3.5}$$

where d is the dimensionality of the system. A similar algebraic decay was found for disordered systems with diffractive scatterers, where now the power law is governed by the diffusive dynamics [101].

Despite the progress in the understanding of fidelity of various systems, a significant class was left out of the investigation. These are systems which show critical behavior as an external parameter changes, such as that at the Anderson MIT, which was discussed in Sec. 2.1. Therefore, we want to bring the study of fidelity into a new arena – that of disordered systems with a metal-to-insulator transition (MIT) – and propose it as a new measure of critical behavior. Our calculations will be performed in the framework of a recently proposed RMT ensemble [67] which models critical behaviour.

3.2 Critical RMT Models

The RMT ensemble of Wigner Lorentzian Random Matrices (WLRM) was introduced in [67], and is defined as:

$$\mathbf{H} = \mathbf{H_0} + x\mathbf{B} \tag{3.6}$$

Both $\mathbf{H_0}$ and $\mathbf{B}$ are real symmetric matrices of size $L \times L$ with matrix elements randomly drawn from a normal distribution with zero mean and a variance depending on the

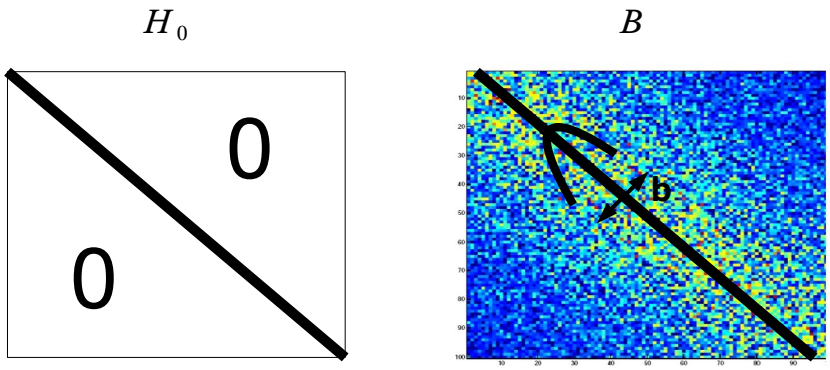

Figure 3.2: Absolute-value-square of the matrix elements of $\mathbf{H_0}$ and $\mathbf{B}$ (in the basis where $\mathbf{H_0}$ is diagonal). The width b gives an effective bandwidth of the matrix. The color scale is such that blue colors are closer to zero whereas more positive values correspond to the red end of the spectrum.

distance of the matrix element from the diagonal

$$\langle \sigma_{nm}^2 \rangle = \frac{1}{1 + |\frac{n-m}{b}|^2}. \tag{3.7}$$

Above, $b \in (0, L)$ is a free parameter that controls the critical properties of the system (see Fig. 3.5). A typical view of the absolute-value-square of the matrix elements of these two matrices (in the basis where $\mathbf{H_0}$ is diagonal) is shown in Fig. 3.2.

Random matrix models with variance given by Eq. (3.7) were introduced in [67] and further studied in [102–105]. Field-theoretical considerations [67, 102, 103] and detail numerical investigations [104,105] have verified that the models show all the key features of the Anderson MIT, including multifractality of eigenfunctions and non-trivial spectral statistics at the critical point. A theoretical estimation for the correlation dimension of the critical eigenstates D_2^{ψ} (see Sec. 2.1.2) gives [106]

$$D_2^{\psi} = \begin{cases} 4b\Gamma(3/2)[\sqrt{\pi}\ \Gamma(1)]^{-1} & ,\ b \ll 1 \\ 1 - 2(2\pi b)^{-1} & ,\ b \gg 1 \end{cases}$$

where Γ is the Gamma function, and $D_2^{\mu} = D_2^{\psi}/d$ is the correlation dimension of the Local Density of States (LDoS) with d is the actual dimensionality of the system [107].

For the WLRM model, $D_2 \equiv D_2^{\mu} = D_2^{\psi}$ since $d = 1$. The correlation dimension D_2^{ψ} is usually defined through the inverse participation number P_2 (see Eq. (2.17)). It is also related to the spectral compressibility $\chi = (d - D_2^{\psi})/2d$, defined through the level number variance $(\delta N)^2 \approx \chi\langle N\rangle$ [104, 108, 109], where N is the number of energy levels in a sufficiently large (relative to the mean level spacing) energy window. We will operate in the basis where $\mathbf{H_0}$ is diagonal. In this basis, the perturbation matrix $\mathbf{B}$ is $x-$invariant [110], i.e. it preserves the same Lorentzian power-law shape (as in Eq. 3.7), while its critical properties (like the multifractal dimension D_2^{ψ}) remain unchanged.

3.3 Fidelity for the WLRM Model

The forward and backward Hamiltonians used for the calculation of the fidelity following Eq. (3.1) are[1]

$$\mathbf{H}_1 = \mathbf{H}(x) \qquad \text{and} \qquad \mathbf{H}_2 = \mathbf{H}(-x) \tag{3.8}$$

For the numerical evaluation of $F(t)$, we have used two types of initial conditions $|\psi_0\rangle$: an eigenstate of $\mathbf{H_0}$ (ES) and a generic 'random' state (RS). In both cases, the results are qualitatively the same. Therefore, we will not distinguish between them. In our numerical experiments we used matrices of size varying from $L = 1000$ to $L = 5000$. We have performed an averaging over different initial states and realizations of the perturbation matrix $\mathbf{B}$ (typically more than 1000).

3.3.1 Standard Perturbative and Fermi Golden Rule Regime

In Fig. 3.3, we report an overview of the temporal behavior of the fidelity $F(t)$ for three representative perturbation strengths. For perturbation strengths smaller than $x_c \approx \frac{\Delta}{\sqrt{\pi}}\sqrt{1+\frac{1}{b}}$, the decay of $F(t)$ is gaussian (see Fig. 3.3a). The perturbative border

[1] From Eq. (3.1) and Eq. (3.8), we see that $x_e = 2x$.

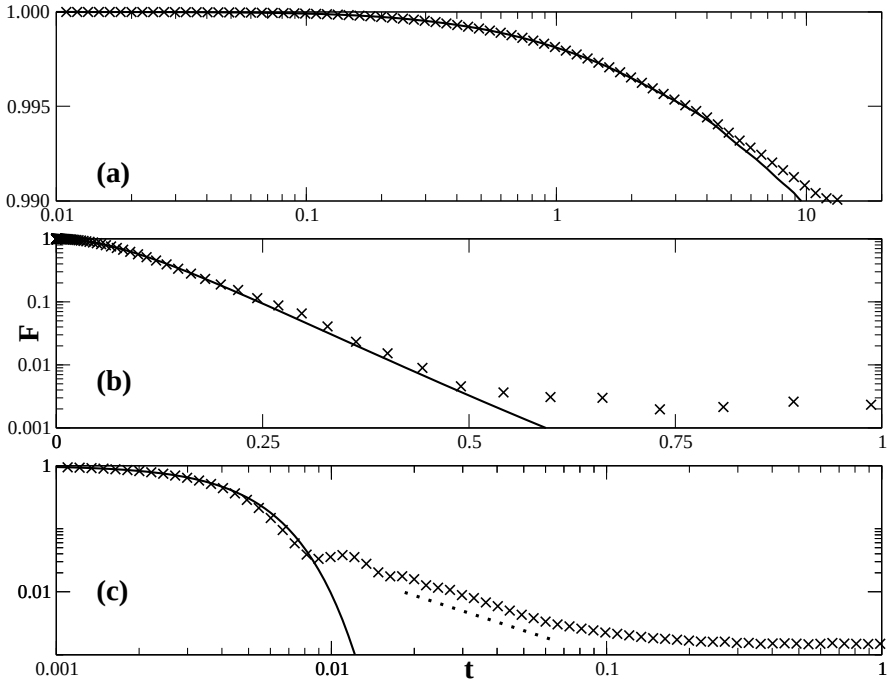

Figure 3.3: Fidelity of an ES, for (a) $x = 0.01$ (the standard perturbative regime), (b) $x = 0.8$ (FGR regime) and (c) $x = 20$ (nonperturbative regime). The solid lines are the LRT results from Eq. (3.9) while the crosses are the outcomes of the numerical simulations with the WLRM model from Eq. (3.6) and Eq. (3.7). In these simulations, $L = 1000$ and $b = 10$. The mean level spacing of the unperturbed system is set to $\Delta \approx 1$. In this case, $x_c \approx 0.59$ and $x_{prt} \approx 1.88$. The dotted line in (c) is plotted to guide the eye on the power-law behavior.

x_c is the perturbation strength needed in order to mix levels within a distance of the mean level spacing Δ [110](see Appendix E).

Above this border, one typically expects an exponential FGR decay of fidelity [91], with a rate given by the width of the Local Density of States (LDoS) [110] (see Fig. 3.3b). We can apply Linear Response Theory (LRT) [1] to evaluate the decay of $F(t)$ in these two regimes. The resulting expression reads

$$\langle F(t)\rangle_{B,n_0} \approx 1-(2x)^2\mathcal{C}(t) \approx \exp^{-(2x)^2\mathcal{C}(t)} \tag{3.9}$$

where $\langle\ldots\rangle_{B,n_0}$ represents a double average over $\mathbf{B}$ and initial states[2]. The right-hand side of expression (3.9) assumes the validity of infinite order perturbation theory. The correlator $\mathcal{C}(t)$ is [1]

$$\mathcal{C}(t)=\int_0^t d\tau_1\int_0^{\tau_1} d\tau_2 \sum_n |c_n|^2\tilde{C}_n(\tau_1-\tau_2)-2\mathcal{I}t^2 \tag{3.10}$$

where $\mathcal{I}=\sum_n |c_n|^4$ is the inverse participation ratio of the initial state, $\tilde{C}_n(t-t')\equiv 2\left(1+\sum_\gamma \sigma^2_{n,\gamma}\cos\left[(E^{(0)}_\gamma-E^{(0)}_n)(t-t')\right]\right)$, and $E^{(0)}_n$ denotes an eigenvalue of $\mathbf{H_0}$. In the case of standard GOE ensembles with $\sigma^2_{nm}=1$, Eq. (3.9) reduces to the expression derived in [85, 94, 95]. The prediction of LRT in Eq. (3.9) is plotted together with the numerical results in Fig. 3.3 for different perturbation strengths. A good agreement between Eq. (3.9) and the numerical data is observed for perturbation strengths less than $x_{\rm prt}$ (see Fig. 3.3a and Fig. 3.3b), where $x_{\rm prt}\approx \Delta\sqrt{b}\frac{\sqrt{\pi-2[\pi/2-\arctan(1/b)]}}{2[\pi/2-\arctan(1/b)]}$. The values of x_c and $x_{\rm prt}$ were derived on the basis of the LDoS analysis [110] (see Appendix E for derivations).

3.3.2 Nonperturbative Regime

For x larger than $x_{\rm prt}$, the decay of $F(t)$ can not be captured by the LRT. The nonperturbative character of this regime was identified already in the frame of the parametric

[2]The derivation is extremely lengthy and readers are refered to [111].

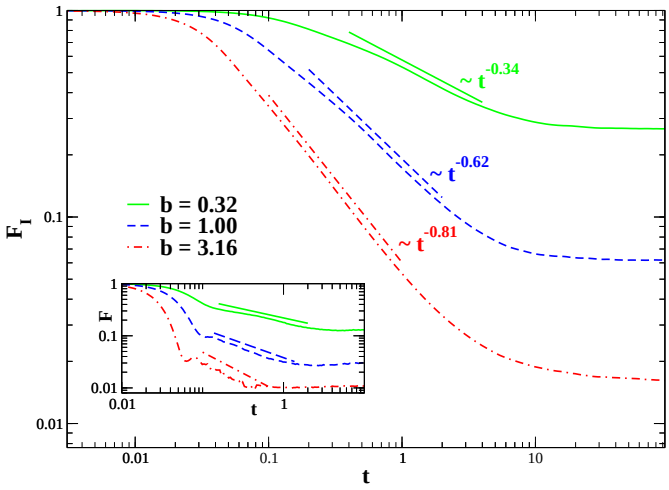

Figure 3.4: F_I for $b = 0.32$, 1.00, and 3.16. The initial state was chosen to be an ES. The mean level spacing of the unperturbed Hamiltonian is set to be $\Delta \approx 1$, while the size of the matrices is $L = 5000$. The perturbation is $x = 5$ for all the cases reported here. In the inset, we also present the fidelity for RS with the same parameters except $L = 1000$. The straight lines are plotted to guide the eye.

evolution of LDoS [110]. A representative temporal behavior of $F(t)$ for $x > x_{\rm prt}$ is reported in Fig. 3.3c. For short times the decay of $F(t)$ is Gaussian, but for longer times one observes a transition to a power law decay. The initial Gaussian decay $F(t) \sim e^{-x^2t^2}$ is universal and can be identified with the quantum Zeno effect [77, 85]. It is valid up to times $t_Z \sim 1/x$. We will focus on the observed power-law decay which takes place for $t > t_Z$.

To reduce statistical fluctuations for further investigation, we use the time-averaged fidelity $F_I(t)$, defined as

$$F_I(t) \equiv \langle F(t) \rangle_t = \frac{1}{t} \int_0^t F(t)dt \ . \tag{3.11}$$

The numerical results $F_I(t)$ for three different b values, $b = 0.32$, 1, and 3.16 are reported in Fig. 3.4. In the inset, we have also included the raw data of the fidelity decay. The fidelity $F(t)$ clearly displays a power-law decay

$$F(t) \propto t^{-\gamma} \tag{3.12}$$

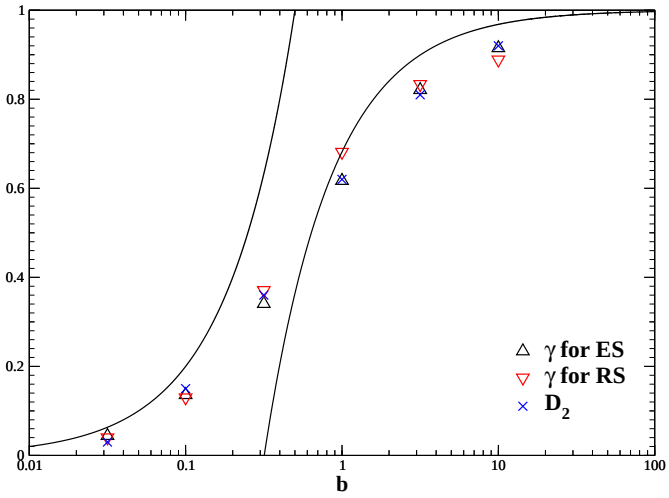

Figure 3.5: D_2 and γ versus b. The parameters are $\Delta = 1$ and $x = 5$. Here, γ comes from power-law fitting from our numerical simulations and the lines are analytical estimations from Eq. (3.8) [67]. The crosses are numerically extracted D_2 from Eq. (2.17) [113] .

with γ being a bandwidth b-dependent exponent.

In the special case of the initial state $|\psi_0\rangle$ being an eigenstate of the backward Hamiltonian $\mathbf{H_2}$, the fidelity is simply the survival probability of wavepacket dynamics

$$P(t) \equiv \left|\left\langle \psi_0 \left| e^{-iH_1 t} \right| \psi_0 \right\rangle\right|^2 \ . \tag{3.13}$$

It is known that the survival probability for a critical system decays as [112]

$$P(t) \sim t^{-D_2^\mu} \tag{3.14}$$

However, in these fidelity experiments, the initial state is neither an eigenstate of H_2 nor of H_1. In fact, Ref. [97] shows that the physics of quantum fidelity involves subtle cross correlations which in general are not captured by the survival probability (or the LDoS which is its Fourier transform) alone.

Nevertheless, motivated by this equivalence between fidelity and survival probability for the specific choice of initial condition, in Fig. 3.5 we compare the extracted power-law exponents γ with the correlation dimension $D_2^\mu = D_2^\psi = D_2$. The D_2's are calculated

numerically [113] from the inverse participation number relation in Eq. (2.17), while the solid lines are estimates from Eq. (3.8) [67]. As can be seen, the agreement between γ and D_2^μ is excellent for all b's, both for the ES and the RS initial conditions, thus establishing the following relation

$$F(t) = t^{-D_2^\mu} \tag{3.15}$$

for the fidelity decay of the WLRM model.

The connection between the exponent γ and the fractal dimension D_2^μ calls for an argument for its explanation. The following heuristic argument provides some understanding of the power-law decay in Eq. (3.15). For any finite Hilbert space, the fidelity $F(t)$ approaches the value $F_\infty \sim 1/L$, being the inverse of the dimension of the Hilbert space. If the dynamics, however, take place in a space with an effective reduced dimension[3] D_2^ψ, we will have $F_\infty = 1/L^{D_2^\psi}$. Assuming a power-law decay in Eq. (3.12) for the fidelity, we can estimate how the time t_* at which $F(t_*) = F_\infty$ scales with L, i.e. $t_* \sim L^{D_2^\psi/\gamma}$. On the other hand, the dynamics of a critical system is characterized by an anomalous diffusive law $L^2 \sim t_*^{2D_2^\mu/D_2^\psi}$ [112], which defines the time $t_* \sim L^{D_2^\psi/D_2^\mu}$ needed to explore the available space L. Equating the two expressions for t_*, we finally get $\gamma = D_2^\mu$. Fig. 3.6 gives an illustration of this argument. Although the numerical results leave no doubt on the validity of Eq. (3.15), a rigorous mathematical proof is more than desirable.

3.4 Conclusions

In conclusion, we have investigated the fidelity decay of systems at MIT, using a critical RMT model. We have identified three distinct regimes of fidelity decay, based on the perturbation strength x. In the regime where $x < x_c$, the fidelity decay is Gaussian, while for $x_c < x < x_{prt}$ the decay is exponential. These two regimes are well-described

[3] For $x > x_{prt}$, the wave functions are fractal and therefore fill only a fraction of the available space with an effective dimensionality given by D_2^ψ.

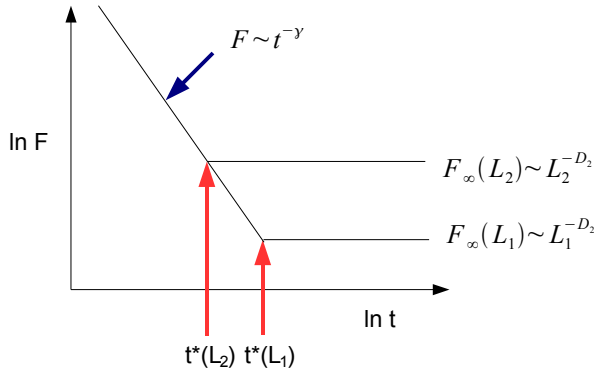

Figure 3.6: Heuristic argument for the exponent of the power-law decay. For a given system of size L, the fidelity saturation will be $F_\infty(L) \sim L^{-D_2}$. Assuming a power-law decay in Eq. (3.12), i.e. $F \sim t^{-\gamma}$, the time to reach this plateau is $t_*(L) \sim L^{D_2/\gamma}$. On the other hand, the dynamics for a critical system is governed by an anomalous diffusive law $L^2 \sim t_*^{2D_2^\mu/D_2^\psi}$. For our model, $D_2 \equiv D_2^\mu = D_2^\psi$, and thus $L \sim t_*$. Equating the two expressions for t_* gives $\gamma = D_2$.

by LRT. The third regime (where $x > x_{prt}$) is nonperturbative and the fidelity decay follows a power law which is dictated by the critical nature of the system. Specifically, we have found that the power-law exponent is equal to the correlation dimension of the critical eigenstates.

Chapter 4

Wavepacket Dynamics of Critical Systems with Nonlinearity

The spreading of a quantum mechanical wavepacket for a particle moving in a periodic lattice is a textbook example. The width increases ballistically with time and the corresponding eigenstates are extended (Bloch states). In the opposite case of strongly disordered systems, however, the eigenstates are exponentially localized, resulting in a total halt of the wavepacket spreading in the long-time limit [6]. Between these extremes flourishes the world of quantum systems with anomalous diffusion. These include systems studied in the early days of quantum mechanics, such as Bloch electrons in a magnetic field [114] as well as quasicrystals [115] and disordered systems at the metal-insulator transition [116]. In these cases, the eigenfunctions (or even the spectrum) show a fractal structure which dictates the wavepacket spreading.

The physical motivation to study such systems, along with the mathematically intriguing nature of their spectra, led to a series of works that eventually advanced our understanding of their dynamical properties. Most of these works have focused on the analysis of the temporal decay of the survival probability $P(t)$ at the initial position n_0

and the growth of the wavepacket's second moment $m_2(t)$ [112, 117–119].

Recently, a lot of research efforts have focused on understanding the effects of interaction-induced nonlinearity in the wavepacket dynamics. Much of this attention was motivated by recent experimental achievements with ultracold atoms in optical lattices, while at the same time the effects of nonlinearity in wave propagation is a long-standing problem in the field of nonlinear optics. Both fields find a common mathematical framework, provided by the Discrete Nonlinear Schrödinger Equation (DNLSE) model. In particular, Ref. [120] has numerically studied the destruction of Anderson localization by weak nonlinearity in the framework of the disordered DNLSE model. They claimed that above a certain critical nonlinearity strength, the Anderson localization is destroyed, and hence the initial excitation will completely delocalize for infinite times. This leads to an unlimited subdiffusive spreading where the second moment grows as t^α with exponent $\alpha \approx 0.3 \sim 0.4$. On the other hand, Ref. [121] proved the statement that in the large amplitude regime, complete energy diffusion is impossible in the disordered DNLSE model, thus disproving the claims in Ref. [120]. They have further supported this statement by studying the temporal evolution of the participation number (see Sec. 2.1.2) and showing numerically that it does not diverge as a function of time as it should in the case of subdiffusion. Therefore, they concluded that wave packet diffusion is absent in the disordered DNLSE model.

Despite all this activity, nothing is known about the effects of nonlinearity in the wavepacket spreading for systems with fractal spectra and eigenfunctions. Noticeable exceptions are Refs. [122, 123] which numerically studied the wavepacket dynamics for the prototype one-dimensional (1D) tight-binding Harper model with nonlinearity. Their conclusions, however, are contradictory. Although both studies conclude that *infinitesimal* nonlinearity results in a short-time subdiffusive spreading of the variance $m_2 \sim t^\alpha$, they give different values for the power-law exponent. While Ref. [123] concludes that the subdiffusive spreading persists for longer time, Ref. [122] reports a saturation of the second moment. Moreover, they both fail to identify traces of mul-

tifractality (which are associated with the underlying linear model) in the dynamics generated by the corresponding nonlinear system.

In the present work, we address the nonlinearity-induced destruction of the anomalous diffusion. Our focus is on the 1D Harper model at criticality but we expect that our results will be applicable to other critical models, such as Fibonacci lattices. The first part of this chapter will give an overview of the linear Harper model at criticality. We will discuss its spectral and eigenfunction properties, and review the basic facts concerning wavepacket dynamics of critical systems. We will then introduce the nonlinear Harper model in the second part and investigate the effects of nonlinearity on the spreading and the evolving profile of a wavepacket both numerically and analytically [2]. Finally, our conclusions will be presented in the last section.

4.1 Linear Harper Model

In this section, we will briefly review the basic properties of the linear Harper model. Its dynamics is described by the standard 1D tight-binding model,

$$i\frac{\partial\psi_n(t)}{\partial t} = \psi_{n+1}(t) + \psi_{n-1}(t) + V_n\psi_n(t) \ , \tag{4.1}$$

where $\psi_n(t)$ denotes the probability amplitude for a particle to be at site n at time t. For the Harper model, the on-site potential V_n takes the specific form of

$$V_n = \lambda\cos(2\pi\sigma n + \phi) \ . \tag{4.2}$$

This model was originally proposed by Harper to describe Bloch electrons moving on a 2D periodic potential in the presence of a perpendicular magnetic field [124]. The dimensionless parameter $\sigma = a^2eB/hc$ in Eq. (4.2) represents the number of magnetic flux quanta per unit cell of area a^2. We work with the case where σ is an irrational number, so that the period of the on-site potential V_n is incommensurate with the lattice period. Such a quasiperiodic model turns out to show interesting critical behavior.

First, we would like to understand the properties of the eigenstates. Let us write $\psi_n(t) = c_n e^{-iEt}$ and turn Eq. (4.1) into

$$Ec_n = c_{n+1} + c_{n-1} + \lambda \cos(Qn + \phi)\ c_n \tag{4.3}$$

where $Q = 2\pi\sigma$.

Following Ref. [125], we make the ransformation to the reciprocal space

$$c_n = e^{ikn} \sum_{m=-\infty}^{\infty} g_m e^{im(Qn+\phi)} \tag{4.4}$$

where k is a wave vector.

Substituting Eq. (4.4) into Eq. (4.3) and after some algebraic manipulation, one obtains

$$Eg_m = \tfrac{1}{2}\lambda(g_{m+1} + g_{m-1}) + 2\cos(Qm + k)\ g_m. \tag{4.5}$$

One immediately notices that the transformed equation Eq. (4.5) for $\lambda = 2$ has the same form as Eq. (4.3).This is called the *Aubry duality* [125].

This duality enables us to investigate localization of eigenstates in the two spaces. We define γ_1 to be the inverse localization length (see Eq. (2.7)) in the real space, and from the Thouless formula [35] (see Eq. (2.9)), we have

$$\gamma_1(E) = \int dE' \ln\left|E - E'\right| \rho(E')\ . \tag{4.6}$$

Similarly, the inverse localization length in the reciprocal space γ_2 can be written as

$$\gamma_2(E) = \int dE' \ln\left|\frac{2(E - E')}{\lambda}\right| \rho(E')\ , \tag{4.7}$$

which leads to

$$\gamma_1(E) = \gamma_2(E) + \ln(\lambda/2). \tag{4.8}$$

In the case of $\gamma_2 = 0$,

$$\gamma_1 = \ln(\lambda/2) > 0 \tag{4.9}$$

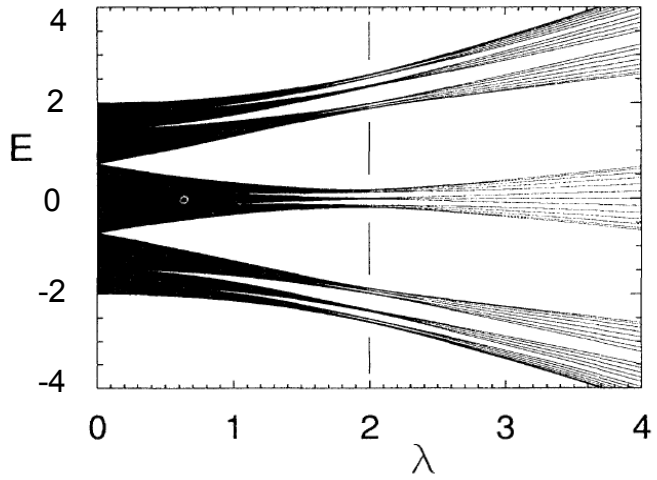

Figure 4.1: Energies of the linear Harper model as a function of λ for a rational approximant $\sigma = \frac{32}{55}$ of the golden mean. The point $\lambda = 2$ is at the transition between regimes of extended states ($\lambda < 2$) and localized states ($\lambda > 2$) for incommensurate σ. Figure taken from [126].

and γ_1 being non-negative gives $\lambda > 2$. This corresponds to localization of eigenstates in the real space but extended eigenstates in the reciprocal space. In this case, the spectrum(in the real space) is point-like and all states are exponentially localized (localized regime).

By similar arguments, the opposite scenario corresponds to the case of $\gamma_1 = 0$ with $\gamma_2 > 0$ and $\lambda < 2$. The eigenstates (in the real space) are extended and the spectrum consists of bands (ballistic regime). Fig. 4.1 illustrates the spectral changes for the Harper model.

At the critical point $\lambda = 2$, there exists a metal-insulator transition, where the spectrum is a zero measure Cantor set with fractal dimension $D_0^E \leq 0.5$ [127,128] and exhibits the rich Hofstadter's butterfly structure (see Fig. 4.2) [129]. Furthermore, the eigenstates are multifractal, showing self-similar fluctuations on all scales, with D_2^μ, the correlation dimension of the Local Density of States (LDoS) and D_2^ψ, the correlation dimension of the fractal eigenfunctions [124–126, 130, 131].

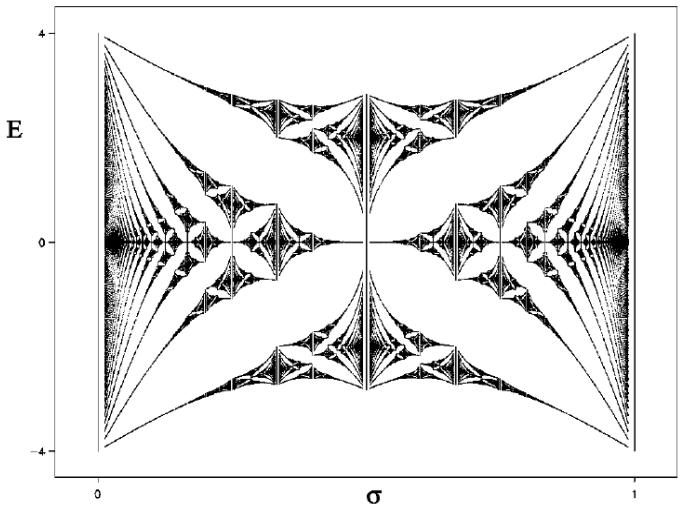

Figure 4.2: The energy spectrum of the Harper model for $\lambda = 2$ vs the incommensurability parameter σ. The resulting graph is known as the Hofstadter's butterfly. Figure taken from [128].

Previous studies have also shown that, at the critical point, the temporal decay of the probability to remain at the original site n_0 up to time t goes as [1]

$$P(t) \equiv |\psi_{n_0}(t)|^2 \sim t^{-D_2^\mu} \tag{4.10}$$

while the wavepacket second moment grows as

$$m_2(t) \equiv \sum_n (n - n_0)^2 |\psi_n(t)|^2 \sim t^{2\beta} \quad \text{with} \quad \beta \geq D_2^\mu / D_2^\psi \tag{4.11}$$

where the exponent β depends on both D_2^μ and D_2^ψ [112] (see Fig. 4.3 and Fig. 4.4).

In fact, recent studies were able to demonstrate that the center of the wavepacket spatially decreases as $|n - n_0|^{D_2^\psi - 1}$ for $|n - n_0| \ll t^\beta$ while the front shape scales as [119]

$$P(n,t) = A(t) \exp(-|(n - n_0)/\sqrt{m}_2|^{1/(1-\beta)}) \tag{4.12}$$

[1] See inset in Fig. 4.5.

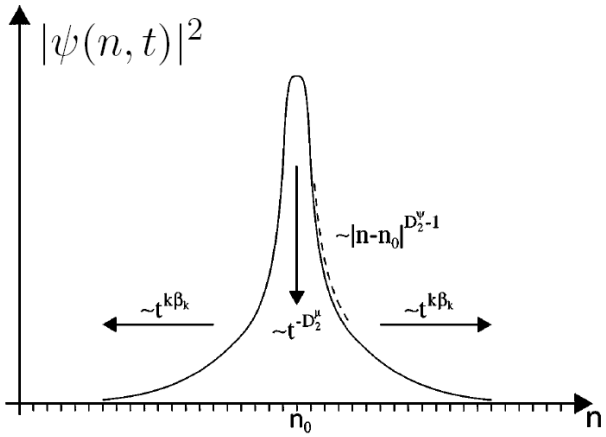

Figure 4.3: Quantum diffusion of a wave packet initially started at site n_0. The survival probability $P(t)$ decays as $t^{-D_2^\mu}$s, whereas the k-th moment increases as $t^{k\beta_k}$, where $\beta_k \geq D_2^\mu/D_2^\psi$. For the case of the second moment, i.e. $k = 2$, it grows as $t^{2\beta}$ with $\beta \geq D_2^\mu/D_2^\psi$. In any case, the center of the wave packet spatially decreases as $|n - n_0|^{D_2^\psi - 1}$ for$|n - n_0| \ll t^\beta$. Figure is taken from [112].

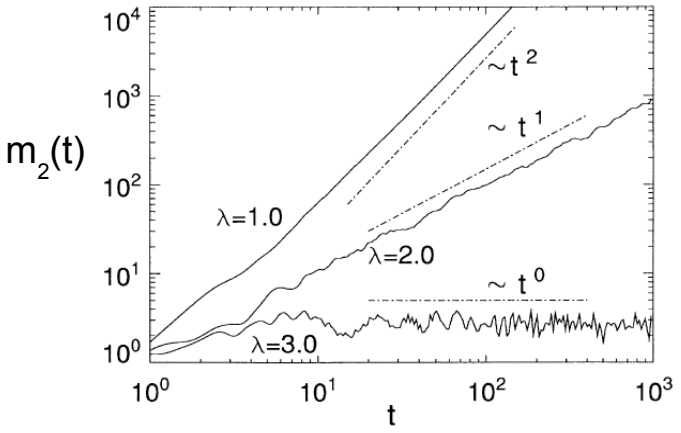

Figure 4.4: Time evolution of the variance of a wave packet. In the case of $\lambda = 2$, anomalous diffusion is observed. For the case of $\lambda < 2$, the spreading is ballistic, as expected in an extended system, while localized states in the case of $\lambda > 2$ halt diffusion. Figure taken from [126].

where $A(t)$ is the height of the wave profile at time t.

4.2 Effects of Nonlinearity in Wavepacket Spreading

We would like to study the effects of nonlinearity on the anomalous diffusion in the Harper model. Introducing an on-site nonlinear term into Eq. (4.1), we come out with the nonlinear Harper model (NLHM). Mathematically, it is described by the following discrete nonlinear Schrödinger equation (DNLSE),

$$i\frac{\partial\psi_n(t)}{\partial t} = \psi_{n+1}(t) + \psi_{n-1}(t) + V_n\psi_n(t) - \chi|\psi_n(t)|^2\psi_n(t) \tag{4.13}$$

We want to investigate the temporal behavior of the variance $\langle m_2(t)\rangle_\phi$ for the NLHM at the critical point $\lambda = 2$. The initial condition is always taken to be a δ-like localized state i.e. $\psi_n(t=0) = \delta_{n,n_0}$. An averaging $\langle\cdot\rangle_\phi$ over a random distribution of the phase ϕ (at least 50) in Eq. (4.2) [or equivalently over different initial positions n_0 of the δ function] is done. In our calculations, we take σ to be the golden mean $\sigma_G = (\sqrt{5}-1)/2$. Equation (4.13) has been integrated numerically using a finite-time-step fourth order Runge-Kutta algorithm on a self-expanding lattice in order to eliminate finite-size effects [132]. Whenever the probability of finding the particle at the edges of the chain exceeded 10^{-10}, ten new sites were added to each edge. Numerical precision was checked by monitoring the conservation of probability (norm) $\sum_n |\psi_n(t)|^2 = 1$. In all cases, the deviation from unity was less than 10^{-6}.

4.2.1 Wavepacket Spreading

In Fig. 4.5, we report our numerical results for some representative χ values in a double logarithmic plot. In all cases, the variance displays a power-law behavior $\langle m_2(t)\rangle \sim t^\alpha$. Leaving aside the very initial spreading $t \leq 1$ (which in all cases is ballistic), we observe that for $\chi \geq \chi^* \sim 5.5\times10^{-4}$ the spreading is subdiffusive with $\alpha < 2\beta$. This spreading

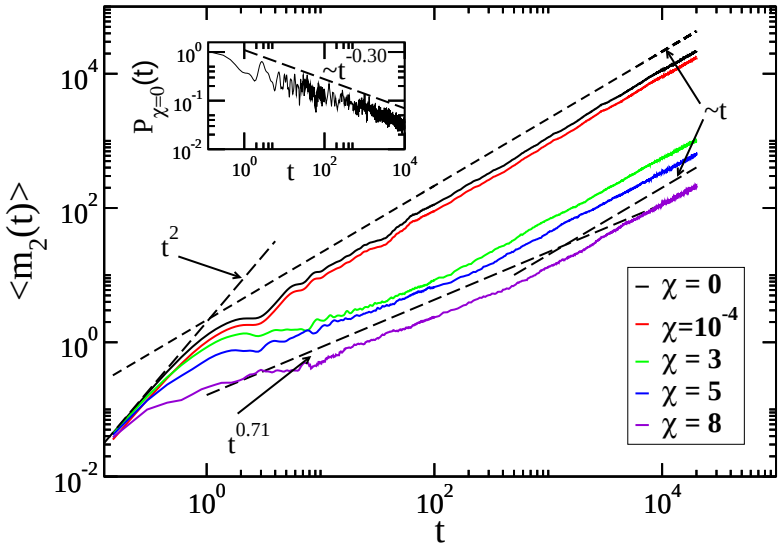

Figure 4.5: The variance $\langle m_2(t)\rangle_\phi$ for various χ values of the NLHM. The $\chi = 10^{-4}$ case is shifted downwards in order to distinguished it from the $\chi = 0$ case. Dashed lines have slopes as indicated in the figure and are drawn to guide the eye. Inset: the decay of $P(t) \sim t^{-D_2^\mu}$ for the linear Harper model ($\chi = 0$).

is valid up to time $t < t^*$ and then relaxes to the anomalous diffusion $\alpha = 2\beta$ that characterizes the linear Harper model.

To obtain the law of spreading for $t < t^*$, we consider the following simple model (see Fig. 4.6). The initial site together with its nearby sites $n = n_0 \pm \delta n$ is considered as a confined source [2]. Anything emitted from them moves according to the spreading law of the linear Harper i.e. $s(t) = \sqrt{\langle m_2(t)\rangle_\phi} = vt^\beta$ since for $t < t^*$ the leaking norm is small and therefore the nonlinear term in Eq. (4.13) is negligible with respect to the on-site potential V_n.

Initially, all probability is concentrated at the source. Due to the nonlinear nature of the system, the decay rate is not constant but depends on the remaining norm. Thus, the decay process is characterized by the nonlinear equation,

$$dP(t)/dt = -\Gamma_{P(t)}P(t) \tag{4.14}$$

[2]Our numerical simulations showed that, in general, $\delta n = 1$ or 2 sites.

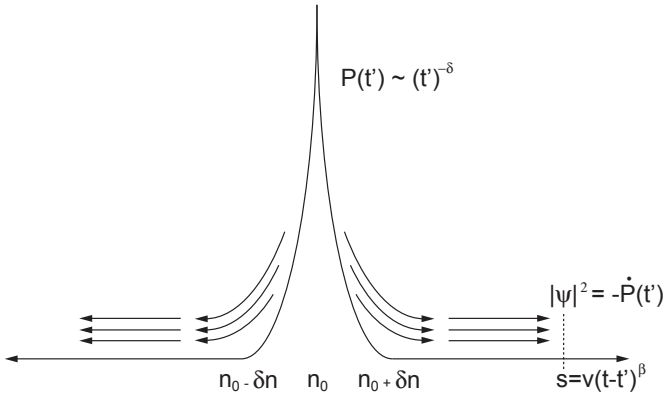

Figure 4.6: Illustration of the source model. The initial site n_0 together with nearby sites $n_0 \pm \delta n$ are considered as a source. The decay of the initial probability at the source is characterized by $P(t') \sim (t')^{-\delta}$ whereas the flux emitted from the source is $-\dot{P}(t')$. This emission moves according to the spreading law $s = v(t-t')^{\beta}$.

which leads to a non-exponential decay [133]. On the other hand, for $\chi = 0$, the decay is power-law

$$P(t) \sim t^{-\delta} \tag{4.15}$$

with $\delta = D_2^{\mu}$ (see Eq. (4.10) above). It is, therefore, natural to expect that for $\chi \neq 0$, we will have a slower decay with $\delta \leq D_2^{\mu}$ due to self-trapping [134–136]. The variance of the confined-source model is then given by [137]

$$M_{\rm PS}(t) \approx \int_0^{\infty} ds\ s^2 \int_0^t dt^{'} (-\dot{P}(t^{'}))\, \delta(s - v(t-t^{'})^{\beta}) \ , \tag{4.16}$$

where $-\dot{P}(t)$ is the flux emitted from the confined source. Substituting Eq. (4.15) for $P(t)$, we get

$$M_{\rm PS}(t) \sim v^2 \int_0^t dt^{'} (1/t^{'})^{\delta+1} (t-t^{'})^{2\beta}. \tag{4.17}$$

If we do a variable substitution $\tilde{t} = t^{'}/t$, we will get

$$M_{\rm PS}(t) \sim v^2\ t^{2\beta-\delta} \int_0^1 d\tilde{t}\ (1/\tilde{t})^{\delta+1} (1-\tilde{t})^{2\beta}, \tag{4.18}$$

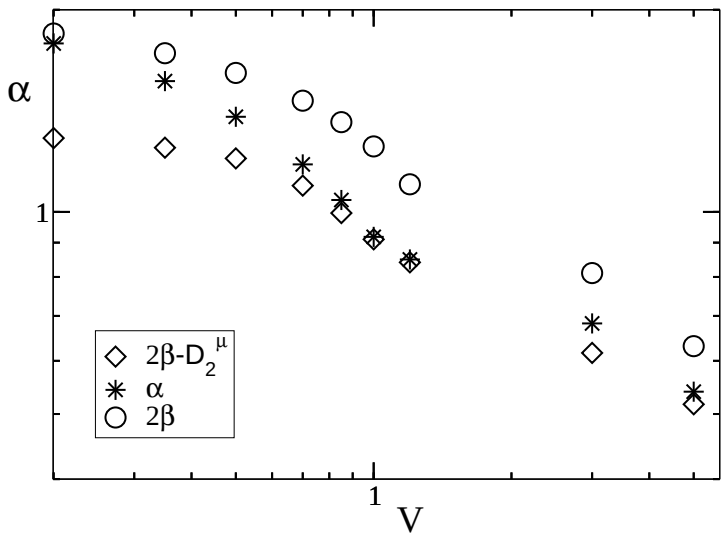

Figure 4.7: The fitting values (stars) of the power-law exponent α vs. V for the Fibonacci model. Circles are the fitting exponent 2β of the linear model for the spreading $\langle m_2(t)\rangle \sim t^{2\beta}$, while diamonds are the extracted exponents $2\beta - D_2^\mu$, where D_2^μ was obtained from the decay $P(t) \sim t^{-D_2^\mu}$ of the linear model.

which leads to

$$\langle m_2(t)\rangle = M_{\rm PS}(t) \propto t^\alpha \tag{4.19}$$

with $2\beta - D_2^\mu \leq \alpha \leq 2\beta$.

In order to compare the results of numerical simulations with the theoretical predictions of Eq. (4.19), we have calculated for the linear Harper model the decay exponent $\langle D_2^\mu\rangle_\phi$ of the survival probability (see inset of Fig. 4.5) and the power-law exponent of the variance $\langle m_2(t)\rangle_\phi$. The least-squares fit gives the values $\langle D_2^\mu\rangle_\phi \approx 0.30 \pm 0.03$ and $2\beta \approx 1.00 \pm 0.03$. The numerically extracted value of $\alpha = 0.71$ fulfills nicely the bound $2\beta - D_2^\mu = 0.70$ given by Eq. (4.19).

To further test the validity of Eq. (4.19), we have also performed simulations with the Fibonacci model, where D_2^ψ and D_2^μ (and hence β) can be varied according to the on-site potential V_n. The latter takes only two values $\pm V$ ($V \neq 0$) that are arranged in a Fibonacci sequence [115]. Again, we find a power-law spreading $\langle m_2(t)\rangle \sim t^\alpha$. The

extracted exponents α corresponding to various V's are reported in Fig. 4.7 together with the theoretical predictions and they confirm the validity of Eq. (4.19).

From Fig. 4.5, we see that the time scale t^* up to which the power law of Eq. (4.19) applies depends on the strength of the nonlinearity parameter χ. One can estimate t^* from the fact that the effective potential $V_\chi = -\chi|\psi_{n_0}(t)|^2$ is comparable with the on-site potential $V_{n_0} \sim \lambda$ of the linear model at t^*. After this time, one expects that the effect of nonlinearity on the wavepacket spreading is negligible and therefore the survival probability should decay as $P(t) = |\psi_{n_0}(t)|^2 \sim t^{-D_2^\mu}$. Following this line of argument, we have that

$$V_{n_0} \sim \chi|\psi_{n_0}(t^*)|^2 \rightarrow V_{n_0} \sim \chi(t^*)^{-D_2^\mu}, \tag{4.20}$$

leading to

$$t^* \sim \chi^\gamma \tag{4.21}$$

with $\gamma = 1/D_2^\mu$. To test this theoretical prediction, we have manually scaled the time axis so that the variance curve where Eq. (4.19) applies overlaps for various χ values. The extracted scaling parameters $t^*(\chi)$ are plotted in the inset of Fig. 4.8. One can clearly see that the numerical data confirms the theoretical prediction of Eq. (4.21).

Now, let us turn our discussion to the evolving wavefunction for $\chi \geq \chi^*$. For $t > t^*$, although the temporal behavior of the variance becomes the same as that of the linear Harper model, other moments differ. The profiles reported in Fig. 4.9 are snapshots of the average wavefunction at various times and for three representative values of $\chi = 1, 3$ and 5 (the linear case $\chi = 0$ is also plotted in the upper inset for comparison). They are plotted with the scaling assumption

$$P_{\rm s}(x,t) = \sqrt{\langle m_2(t)\rangle} P_\chi(n,t), \quad x \equiv \frac{n-n_0}{\sqrt{\langle m_2(t)\rangle}}. \tag{4.22}$$

The data collapse for $|x| \leq 8$ (different curves corresponding to various times t and nonlinearity strengths χ) reveals that this representation is not affected much by finite-

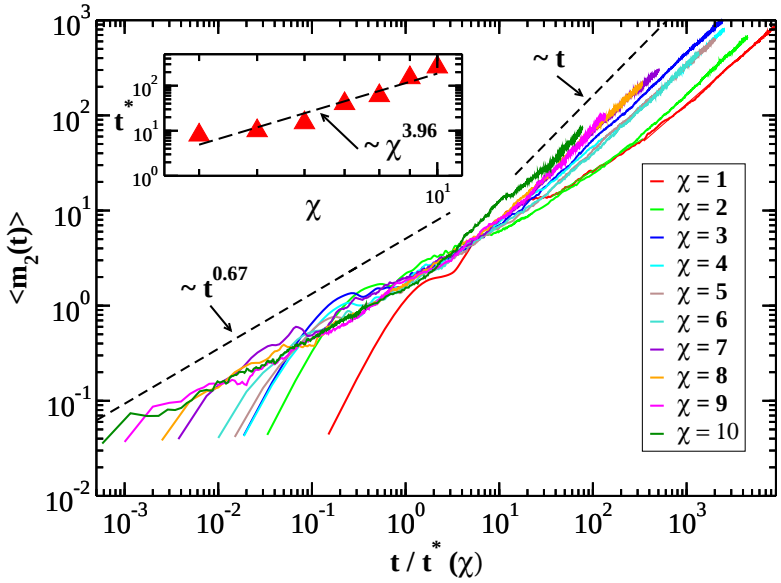

Figure 4.8: Variance vs. scaled time. The t^* is extracted by scaling the time-axis so that the variance curves overlap in the time-region where Eq.(4.19) is valid. Inset: the scaling of t^* versus χ. The dashed line indicates the least square fit with slope 3.96 [the theoretical prediction Eq. (4.21) estimates it to be 3.45 ± 0.35].

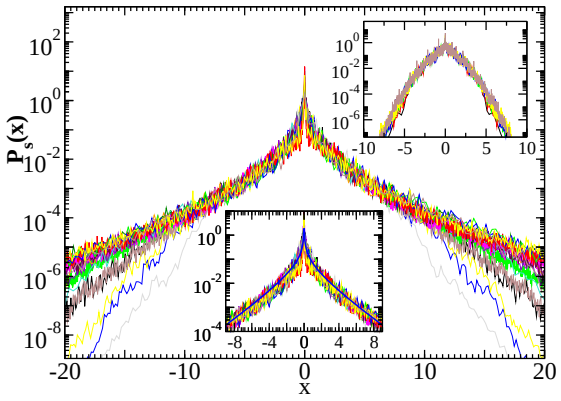

Figure 4.9: The scaled probability distributions $P_s(x)$ versus x of the NLHM at different time t (including $t > t^*$) and for various $\chi > \chi^*$. The nice overlap of the curves at the core $|x| \leq 8$ confirms the validity of the scaling law Eq. (4.22). The scaling is lost for $|x| > 8$. The lower inset shows the behavior near the origin. The blue solid line is the fitting curve Eq. (4.23). For comparison, we also report in the upper inset the probability distribution $P_s(x)$ of the linear Harper model.

χ corrections, although the tails of the profile are χ-dependent. In fact, we found that the probability distribution near the center can be described by the formula:

$$P_s(x) \sim |x|^{-\gamma} \exp(-|x|/l_\infty), \;\; |x| \leq 8, \tag{4.23}$$

where $\gamma \approx 0.7$ and $l_\infty \approx 1.82$. We note that a similar expression for the core of the probability distribution applies for 1D and quasi-1D disordered models with zero nonlinearity [132, 138].

4.2.2 Critical Nonlinearity

Going back to Fig. 4.5, we observe that the destruction of the anomalous diffusion of the linear model takes place for $\chi \geq \chi^*$. To quantify χ^*, we evaluate the time-average survival probability $\langle P(T) \rangle_T$, defined as [135, 136, 139]

$$\langle P(T) \rangle_T \equiv \lim_{T \to \infty} \frac{1}{T} \int_0^T |\psi_{n_0}(t)|^2 dt \tag{4.24}$$

for various values of the nonlinearity strength χ. In our numerical calculations, we took an average over a time interval of $T = 20000$. Our numerical results are reported in Fig. 4.10. We see that up to $\chi^* \approx 5.5 \times 10^{-4}$, the time-average survival probability $\langle P(T) \rangle_T$ remains unchanged. As the nonlinearity strength χ is increased further, a fraction of the excitation begins to localize at the initial site. As a result, the fraction of the excitation that can propagate is now effectively smaller, leading to smaller $\langle m_2(t) \rangle$ as χ is increased. We note that a similar type of self-trapping phenomenon [134, 135] was observed in various nonlinear lattices [122, 123, 136, 139–143], although in all these cases the value of χ^* was much larger, i.e. $\chi^* \sim O(1)$.

The following heuristic argument provides some understanding of the appearance of self-trapping phenomenon for the NLHM. We consider successive rational approximants $\sigma_i = p_i/q_i$ of the continued fraction expansion of σ. On a length scale q_i, the periodicity of the potential is not manifested and we may assume that for $\chi < \chi^*$ the eigenfunctions

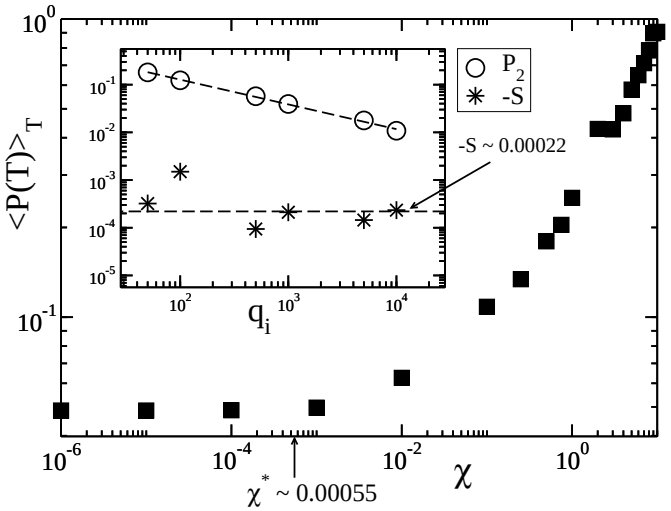

Figure 4.10: The integrated survival probability $\langle P(T)\rangle_T$ vs. χ. For $\chi \geq 5.5\times10^{-4}$, we observe an increase in $\langle P(T)\rangle_T$. The first point in the curve corresponds to $\chi = 0$ and is included in the log-log plot as a reference point. Upper inset shows the scaling of the P_2 and $-S$ vs. the system size q_i. The horizontal dashed line is $S = -2.2 \times 10^{-4}$.

preserve their critical structure as in the case of $\chi = 0$. In this case, the partitioning of the energy over the q_i sites is [3]

$$\mathcal{H} = -\frac{\chi}{2}\sum_{n=1}^{q_i}|\psi_n|^4 + \sum_{n=1}^{q_i}(\psi_n^*\psi_{n-1} + \psi_{n-1}^*\psi_n) + \sum_{n=1}^{q_i}V_n\,|\psi_n|^2 \tag{4.25}$$

Let us first estimate the energy $\mathcal{H}_{\rm ss}$ associated with the initial state δ_{n,n_0}. Since the probability distribution is located at a single site, we get an energy

$$\langle\mathcal{H}_{\rm ss}\rangle_\phi = -\frac{\chi}{2}\ . \tag{4.26}$$

Now we want to evaluate the partitioning of the energy $\mathcal{H}_{\rm ext}$ for a fractal wavefunction. In this case, the first term in Eq. (4.25) is the inverse participation number [4], which scales with the system size q_i as

$$P_2 \sim q_i^{-D_2^\psi} \tag{4.27}$$

[3]We recall that the DNLSE in Eq. (4.13) can be derived from the Hamiltonian Eq. (4.25) using the Poisson brackets $\{\psi_m, \psi_n^*\} = i\delta_{mn}$, $\{\psi_m, \psi_n\} = \{\psi_m^*, \psi_n^*\} = 0$ and the equation of motion $\dot{\psi}_n = \{H, \psi_n\}$.

[4]See previous discussion around Eq. (2.18) on the inverse participation number.

Hence, in the thermodynamic limit where $q_i \to \infty$, this term will go to zero. We define the sum of the two other terms as follows:

$$S = \left\langle \sum_{n=1}^{q_i} \left(\psi_n^* \psi_{n-1} + \psi_{n-1}^* \psi_n + V_n \left| \psi_n \right|^2 \right) \right\rangle_\phi \tag{4.28}$$

We found from numerical calculations (see inset of Fig. 4.10) that S goes to a finite value in the thermodynamic limit and therefore arrive at the equation $\langle \mathcal{H}_{\text{ext}} \rangle_\phi = S$.

If $\mathcal{H}_{\text{ext}}$ is higher than the initial energy H_{ss}, then conservation of energy prevents the partitioning of energy over all q_i sites. Therefore, in the thermodymanic limit, we get for the critical nonlinearity χ^* that

$$\chi^* \sim -2S. \tag{4.29}$$

Numerical results in Fig. 4.10 (inset) indicate that $S \sim -2.2 \times 10^{-4}$, which is consistent with our numerical evaluation of $\chi^* \sim 5.5 \times 10^{-4}$.

4.3 Conclusions

In this chapter, we have studied the nonlinear Harper model at criticality and found bounds for the power-law exponent of the temporal spreading of the wavepacket variance. These bounds reflect the fractal dimension of the LDoS of the linear system. This nonlinear spreading appears for nonlinearity strength above some value and persists up to time $t^* \sim \chi^{1/D_2^\mu}$,which depends parametrically on the nonlinearity strength. After this time, the linear spreading of the second moment is restored; other moments, however, are still affected by the nonlinearity. For the central part of the evolving profile, we have also found a scaling relation that applies to any time and any nonlinearity strength. Our results will find applications in quasiperiodic photonic structures (such as optical super-lattices [144]) and arrays of magnetic micro-traps for atomic BEC [145].

Chapter 5

Dynamics of BECs in Leaking Optical Lattices

One of the most fascinating experimental achievements of the last decade was the BECs of ultra-cold atoms in optical lattices (OLs) [146–150]. Extraordinary degree of precision and control is now available, not only over the design of the OLs, but also on the strength of the interatomic interactions and the preparation as well as the measurement of the atomic cloud. This enables investigation of complex solid state phenomena [149,151–156] and at the same time promises a new generation of nanoscale devices in the emerging field of atom-tronics. Therefore, it is both of fundamental and technological importance to understand the dynamics and the transport properties of BECs in OLs.

On the other hand, one of the most fundamental sources of physical information is time-resolved decay measurements in quantum mechanical systems which are coupled to a continuum via leads or absorbing boundaries. While radioactive decay is a prominent paradigm, there exist recent examples such as transport of atoms in optically generated lattices and billiards [157,158], the ionization of molecular Rydberg states [159], photo-luminescence spectroscopy of excitation relaxation in semiconductor quantum dots and

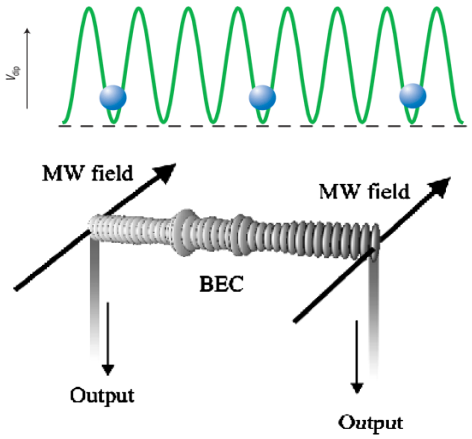

Figure 5.1: Top figure shows a schematic illustration of BECs loaded in an optical lattice. Bottom figure describes a schematic realization of leakage at the two edges of the lattice using continous microwave or Raman lasers to spin-flip atoms that reach the edges to a untrapped state. Thus, the atoms at the edges do not experience the magnetic trapping and hence are released through gravity. The released atoms are then measured at the detectors. Top figure is taken from [150] whereas the bottom figure is from [163].

wires [160], and pulse propagation studies with electromagnetic waves [161].

We consider the statistics of emitted atoms from an OL with leakage at the edges. The leakage can be realized experimentally by applying two separate continuous microwave fields or Raman lasers at the edges of the sample to locally spin-flip the atoms inside the BEC to a untrapped state [162–164]. Spatially localized microwave fields focused below the wavelength can be obtained at the tip of tapered waveguides. The spin-flipped atoms do not experience the magnetic trapping potential, and hence they are released through gravity at the ends of the OL (see Fig. 5.1). Thus, an accurate monitoring of the decay process can be utilized to probe the dynamical properties of BECs in an OL.

In this chapter, we investigate such a decay process and the existence of rare events such as avalanches in the temporal decay of the atomic population [3]. We will show that for a certain range of (rescaled) nonlinearity, there exists a power-law distribution

in the avalanches (jumps in atomic population's temporal decay), characterizing systems at a phase transition. We relate the observed power-law distribution of jumps to the hierachical structure of a mixed phase space shown by a reduced system of three nonlinear coupled oscillators. Furthermore, we propose an order parameter to describe the observed phase transition. It is important to realize that although we will focus our discussions in the framework of BEC system, our results are more general and find applications in many other realizations of the DNLSE (see Sec. 2.3), such as the description of light dynamics in arrays of coupled waveguides, where boundary leakage can be achieved with suitable mirrors.

5.1 Discrete Nonlinear Schrödinger Equation with Dissipation

The simplest model that captures the dynamics of a dilute gas of bosonic atoms in a deep OL, with chemical potential small compared to the vibrational level spacing, is the Bose-Hubbard Hamiltonian (BHH). A detailed discussion is presented in Appendix C, but we shall briefly mention a few essential points here.

In the case of weak interatomic interactions (superfluid limit) and/or a large number of atoms per well (so that the total number of atoms $N \sim \mathcal{O}(10^4 - 10^5)$ is much bigger than the number of wells M), a further simplification is available since the BEC's dynamics admits a semiclassical (mean-field) description. The resulting semi-classical Hamiltonian that describes the dynamics is

$$\mathcal{H} = \sum_{n=1}^{M} [U|\psi_n|^4 + \mu_n|\psi_n|^2] - \frac{T}{2} \sum_{n=1}^{M-1} (\psi_n^* \psi_{n+1} + c.c.) \tag{5.1}$$

where n is the lattice index, $|\psi_n(t)|^2 \equiv N_n(t)$ is the mean number of bosons at site n, $U = 4\pi\hbar^2 a_s V_{\text{eff}}/m$ describes the interaction between two atoms at a single site (V_{eff} is the effective mode volume of each site, m is the atomic mass, and a_s is the s-wave

atomic scattering length), μ_n is the on-site chemical potential, and T is the tunneling amplitude. The 'wavefunction amplitudes'

$$\psi_n(t) \equiv \sqrt{N_n(t)}\exp(-i\phi_n(t)) \tag{5.2}$$

can be used as conjugate variables with respect to the Hamiltonian $i\mathcal{H}$ leading to a set of canonical equations

$$\begin{aligned} i\frac{\partial\psi_n}{\partial t} &= \frac{\partial\mathcal{H}}{\partial\psi_n^*} \\ i\frac{\partial\psi_n^*}{\partial t} &= -\frac{\partial\mathcal{H}}{\partial\psi_n} \end{aligned} \tag{5.3}$$

which upon evaluation yields the DNLSE in Eq. (2.50).

To simulate the leaking process at the two edges, we supplement the standard DNLSE with local dissipation at the two edges of the lattice. The resulting equation reads:

$$i\frac{\partial\psi_n}{\partial\tau} = (\chi\left|\psi_n\right|^2 + \tilde{\mu}_n)\psi_n - \tfrac{1}{2}[\psi_{n-1} + \psi_{n+1}] - i\gamma\psi_n[\delta_{n,1} + \delta_{n,M}] \tag{5.4}$$

where $n = 1, \cdots, M$ is the index of lattice site, $\tau = Tt$ is the normalized time is defined as , $\tilde{\mu}_n = \mu_n/T$ is the rescaled chemical potential, and $\chi = 2U/T$ is the rescaled nonlinearity. We will assume that the chemical potential $\tilde{\mu}_n = \tilde{\mu}$ is the same for all lattice sites.

The atom emission probability γ can be estimated within a mean-field approximation [163]. Here, we consider the case of two output-coupler fields interacting with the atoms at the first and last lattice wells only. We can describe the output coupling through an external reservoir formed by an infinite number of states [163]. For a broadband coupling of strength κ, it was shown in [165] that the Born-Markov approximation leading to an exponentially decaying atomic density inside the BEC should satisfy

$$\frac{\omega^{3/2}}{\pi\kappa^2}\sqrt{\frac{\hbar}{2m}} \gg 1 \tag{5.5}$$

where ω is the 1D trapping frequency and m is the atomic mass. On the other hand, the characteristic delay time is given by [165]

$$t_D = \frac{1}{\pi\kappa^2}\sqrt{\frac{2\omega\hbar}{m}} = \frac{\hbar/T}{\gamma}, \tag{5.6}$$

which together with Eq. (5.5) gives

$$\frac{\hbar\omega}{2\gamma T} \gg 1. \tag{5.7}$$

Using typical parameter values of experiments of BECs in optical lattices, the above condition is fulfilled up to γ around 0.5 [151]. In our study, we have chosen $\gamma = 0.2$ for the case where leakage at the lattice edges is present.

5.2 Survival Probability and Order Parameter

5.2.1 Survival Probability

We describe the decay of the total atomic population remaining in the OL of L sites through the survival probability

$$P(\tau) = \sum_{n=1}^{L} |\psi_n(\tau)|^2 \ . \tag{5.8}$$

Its time derivate $I(\tau) = -\frac{\partial P(\tau)}{\partial \tau}$ is equal to the outgoing atomic flux. It is also useful to define a rescaled interatomic interaction $\Lambda = \chi\rho$ to characterize the initial effective interaction per site, with $\rho = P(\tau = 0)/M$ being the initial average density of atoms in the OL, so that for a different lattice size M, we maintain the same dynamics by keeping Λ constant.

In our numerical experiments, we have used initial conditions with randomly distributed phases, and a constant amplitude with small fluctuations across the lattice. The normalization was done in such a way that $P(\tau = 0) = 1$. Such initial conditions are first thermalized during a conservative (i.e. $\gamma = 0$) transient for times up to $\tau = 500$ typically. After such a transient is completed, dissipations at the lattice boundaries are switched on, leading to a progressive loss of atoms. Furthermore, we set $\tilde{\mu} = 0$ since it only introduces a constant shift in the energy. The dynamical evolution is done through numerical integration by the Runge-Kutta-Fehlberg method and deviations of

$P(\tau)$ from unity in a closed system (i.e. $\gamma = 0$) was of the order of $10^{-5} \sim 10^{-4}$ for the time scale that we are interested in.

In Fig. 5.2, we show the density plots that capture the dynamics of the leaking system (i.e. $\gamma \neq 0$) for some representative values of the rescaled nonlinearity Λ. The color represents the renormalized (with respect to the original population) atomic population $N_n(\tau) = |\psi(\tau)|^2$ at each site.

For small nonlinearity strengths $\Lambda \leq \Lambda_b \sim 0.25$ (see Fig. 5.2a), the system behaves as in the linear regime, i.e. the density is distributed uniformly across the whole lattice. As the rescaled nonlinearity is increased beyond Λ_b (see Fig. 5.2b), we observe that the system organizes itself and localized structures, i.e. the discrete breathers (DB) emerge.. As we have discussed in Sec. 2.3, a DB is a three site solution of the DNLSE, with high atomic density concentrated mainly at the middle site, and two low-density neighboring sites oscillating out-of-phase with respect to the middle site (self-trapped solutions). DBs were observed in various experimental setups [166–171] while their existence and stability was studied thoroughly during the last decade [69, 70, 72, 172–174].

As the rescaled nonlinearity Λ is increased, we see from Fig. 5.2(c-e) that the density of DBs increases. In fact, for $\Lambda = 16$, we observe that the number of breathers K is approaching the lattice size, i.e. $K \sim \mathcal{O}(M)$. We have also found the existence of moving breathers, i.e. breathers that are mobile with smaller density relative to the stationary breathers, for $\Lambda > 0.5$. In the case of $\Lambda \sim \mathcal{O}(1)$, we note the co-existence of both the stationary and moving breathers [1]. The interaction between these two high-density objects will be a subject of interest for our discussion later.

The role of DBs in relaxation phenomena of generic nonlinear lattices was already recognized in [175], where it has been shown that they act as virtual bottlenecks which slow down the decay process [69, 174, 175]. Indeed, Fig. 5.2c shows that for the case of

[1] Note that although moving breathers can survive for very long time, strictly speaking they are not stationary solutions of the DNLSE.

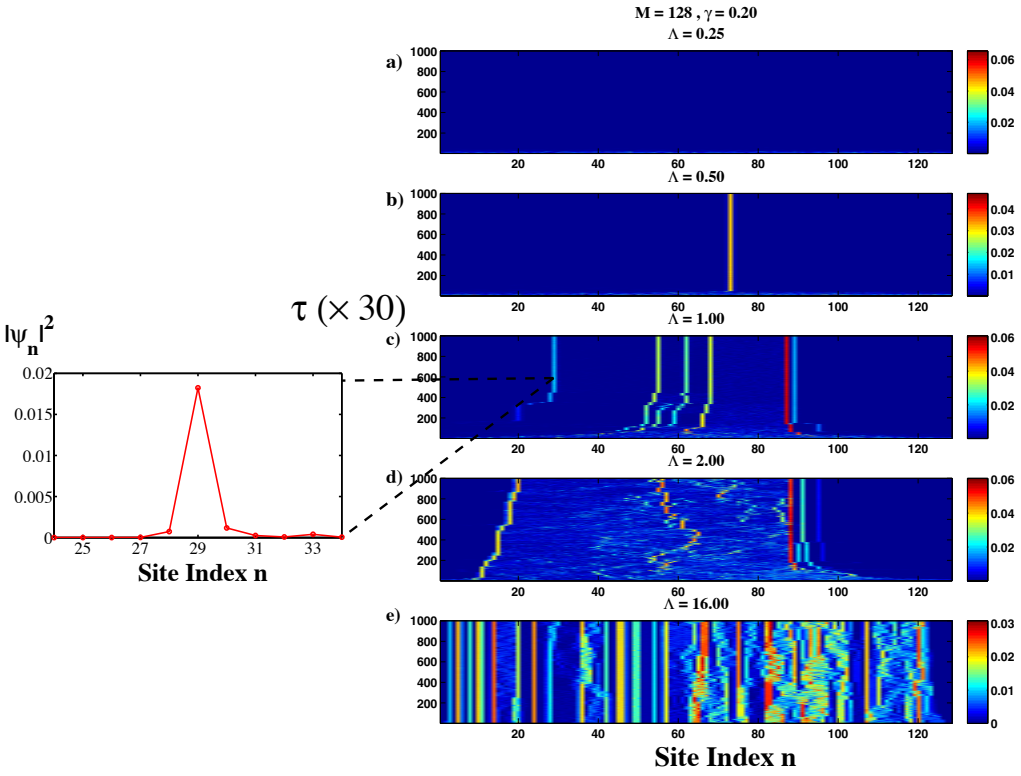

Figure 5.2: The right figure shows a density plot of evolutions of BECs in an optical lattice with leakages at the two edges. The color codes are the $N_n(\tau)$, where red color represents higher density. For (a) small nonlinearity strengths $\Lambda \leq \Lambda_b \sim 0.25$, the density is distributed uniformly across the whole lattice while for (b) $\Lambda > \Lambda_b \approx 0.25$, the first breather appears. At (c) $\Lambda \sim \mathcal{O}(1)$, stationary breathers co-exist with moving breathers. For higher Λ (c)-(e), one observes an increase in the number of breathers and changes in the stability of the breathers. For strong nonlinearity, for e.g. (e) $\Lambda = 16$, the number of breathers is of the order of M. DBs are observed to act as dynamical barriers, insulating the leaking boundaries from the central core. The left figure shows a zoom-in view of the profile a breather in (c) centered at site 29 at time $\tau \approx 600 \times 30$. In all cases, the parameters are $M = 128$ and $\gamma = 0.2$.

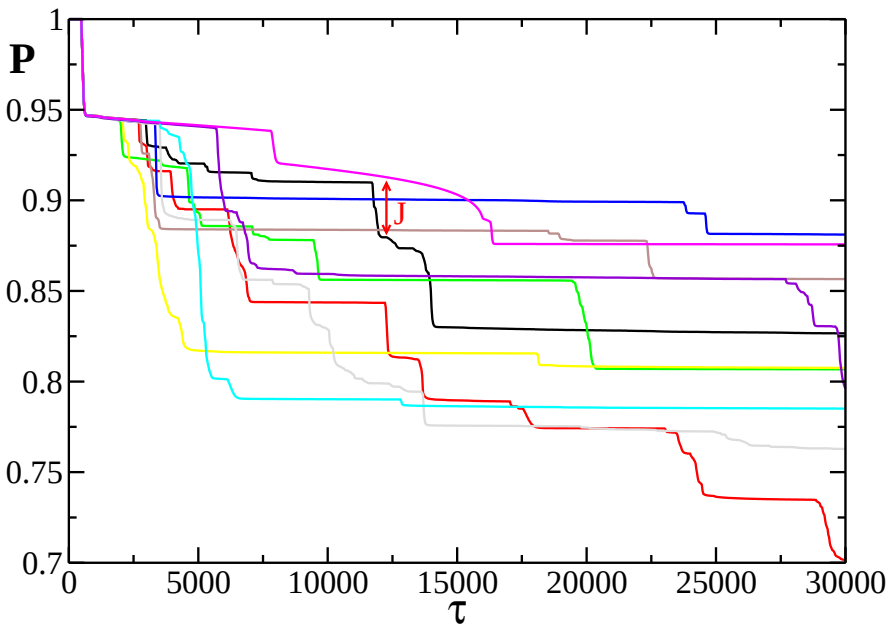

Figure 5.3: An example of avalanches in the survival probability, with jump size J.

$\Lambda \geq 1.0$, the two outer-most breathers act as barriers which trap the atoms in the bulk of the lattice, preventing them from leaking out towards the absorbing boundaries.

In Fig. 5.3, we report (see also [162, 163]) the temporal evolution of $P(\tau)$ for various initial conditions. A striking feature is the appearance of jumps, indicating an avalanche-like behavior where a sudden burst of density (e.g. mass, number of atoms or energy) occurs. The numerical method that we used to evaluate a jump size J is explained in Fig. 5.4. Our target is to analyze the distribution $\mathcal{P}(J)$ of these jumps J.

As we discussed previously, for weak nonlinearity DBs can not form (see Fig. 5.2 for $\Lambda = 0.25$) and $P(\tau)$ decays smoothly, thus leading to no avalanches in the decay. On the other extreme of strong nonlinearity, the number of breathers is of the order of M. In such a case, each breather has a smaller density (due to normalization) and hence it is extremely unlikely to have large jumps in $P(\tau)$.

In the intermediate regime of $\Lambda = \Lambda^* \sim \mathcal{O}(1)$, we found a power-law distribution of

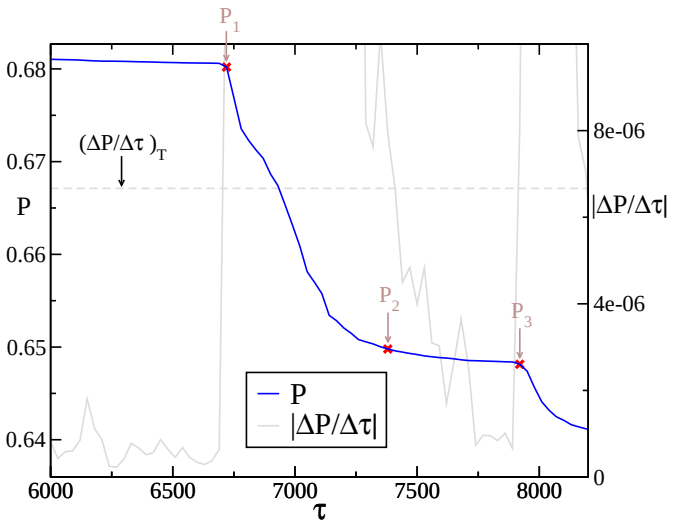

Figure 5.4: Numerical estimation of J. The blue curve is a typical $P(\tau)$ with jumps (left axis) while the grey curve is the absolute value of the numerical derivative $|\Delta P/\Delta\tau|$ (right axis). When $|\Delta P/\Delta\tau|$ rises above a threshold $(\Delta P/\Delta\tau)_T$ (dashed grey line), we register P_1 and when it falls below $(\Delta P/\Delta\tau)_T$, P_2 is registered. A jump J is then estimated to be $J = P_2 - P_1$. The program then continues to register the next point P_3 as the beginning of another jump and so on. The threshold $(\Delta P/\Delta\tau)_T$ used in these calculations was set to be $(\Delta P/\Delta\tau)_T \approx 7 \times 10^{-6}$. We have also checked that our numerical results for the $\mathcal{P}(J)$ do not change for other choices of the threshold.

jumps (see Fig. 5.5)

$$\mathcal{P}(J) \sim J^{-\alpha} \tag{5.9}$$

which can be considered as a signature of a phase transition.

5.2.2 Order Parameter

From the previous section, it is clear that the appearance of a power law distribution in Eq. (5.9) is associated with the existence of DB's. It is, therefore, crucial to quantify their density in terms of the nonlinearity strength, tunneling constant and number of sites. Thus, we propose an order parameter $\mathcal{PR}$ which provides a rough estimate of the

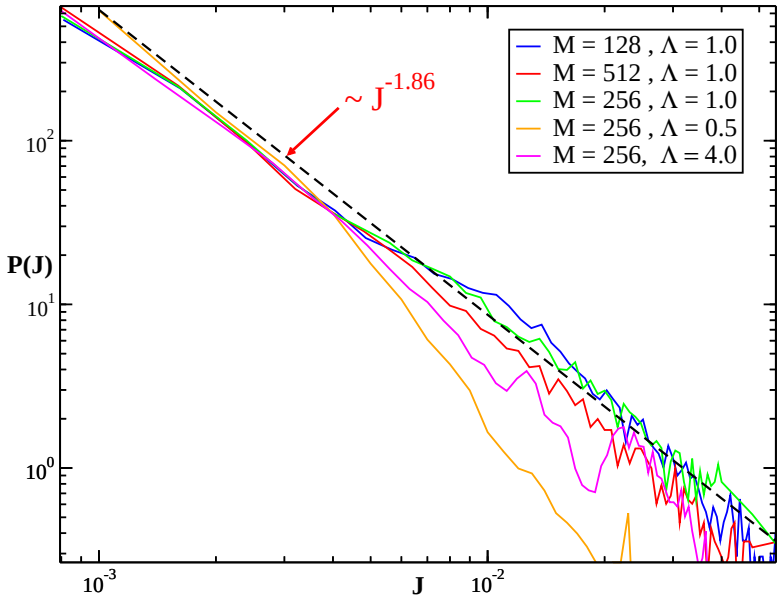

Figure 5.5: Jump distribution $\mathcal{P}(J)$ for different Λ. We observe power-law distribution $\mathcal{P}(J) \sim J^{-\alpha}$ with $\alpha \approx 1.86$ for $\Lambda = 1.0$ whereas for $\Lambda \neq 1.0$, we found deviations from power-law. We set $\gamma = 0.2$ in all cases.

relative number of sites that are occupied by DBs. It is defined as

$$\mathcal{PR} = \left\langle \frac{[P(\tau)]^2}{M \sum_n |\psi_n(\tau)|^4} \right\rangle \tag{5.10}$$

where in the above definition, a time-averaging (after some transient time) is assumed. Note that in the case of $\gamma = 0$ the above quantity is the standard participation ratio (see Eq. (2.19)). The values of $\mathcal{PR}$ for the two extremes of $\Lambda = 0$ (linear lattice) and $\Lambda \gg 1$ (very strong nonlinearity regime) can be calculated analytically, and they are $\mathcal{PR} = 1/2$ and $5/9$ respectively (see Appendix F). The former case correspond to the situation where there is no DB, while in the latter case the number of DBs K is of the order of the total number of lattice sites M. In Fig. 5.6, we report the behavior of $\mathcal{PR}$ as a function of the rescaled nonlinearity Λ. Indeed, the two limits of $\mathcal{PR}$ are confirmed. The transition from one limit to the other is dictated by the scaled nonlinearity Λ.

Now that the limiting cases are understood in the closed system, we turn on the dissipation and evaluate $\mathcal{PR}$ for various Λ's. As can be seen from Fig. 5.6, depending on

the value of Λ, we can still distinguish the two limiting cases. However, an additional situation emerges: For $\Lambda \sim \Lambda_b \approx 0.25$, we observe a dip in the order parameter PR, which takes the value $\mathcal{O}(1/M)$. This corresponds to the creation of only one DB. In fact, as we can see from Fig. 5.6, the transition between the linear regime and the case where one DB is created becomes sharper in the thermodynamic limit. This indicates the existence of a phase transition. We have confirmed that the above behavior of the $\mathcal{PR}$ remains qualitatively the same for various values of γ ranging from 0.01 to 1, and is insensitive to the time window where the evaluation of $\mathcal{PR}$ in Eq. (5.10) is done. In contrast, for $\Lambda \gg 1$, we recover the strong nonlinearity limit where many breathers are found. However, our analysis of $\mathcal{PR}$ was not able to clarify if a similar 'sharp' transition takes place in this limit.

Thus, in the case of $\gamma \neq 0$, we have come out with distinct regimes: $\Lambda < \Lambda_b$, where the system can not support any DB, $\Lambda_b < \Lambda \sim \Lambda^*$ where more than one DB's co-exists with moving breathers, and finally the strong Λ asymptotic regime $\Lambda > \Lambda^* > \Lambda_b$, where the number of DB is comparable to the number of lattice sites M. Our numerical analysis indicated that the regime where the jump distribution $\mathcal{P}(J)$ follows a power law is associated with the second regime.

While a quantitative estimation of the critical nonlinearity Λ^* is still lacking, we can provide a lower-bound for Λ^* by assuming that in the critical regime, the system self-organizes itself into a breather configuration that minimizes the energy. Our calculation in Appendix H implies that this assumption requires $\Lambda^* \geq 1$, which is consistent with our numerical results.

5.3 An Avalanche Event

Let us study in more detail the dynamics that leads to the creation of a single avalanche event. A typical event of an avalanche is depicted in Fig. 5.7, where the process occurs

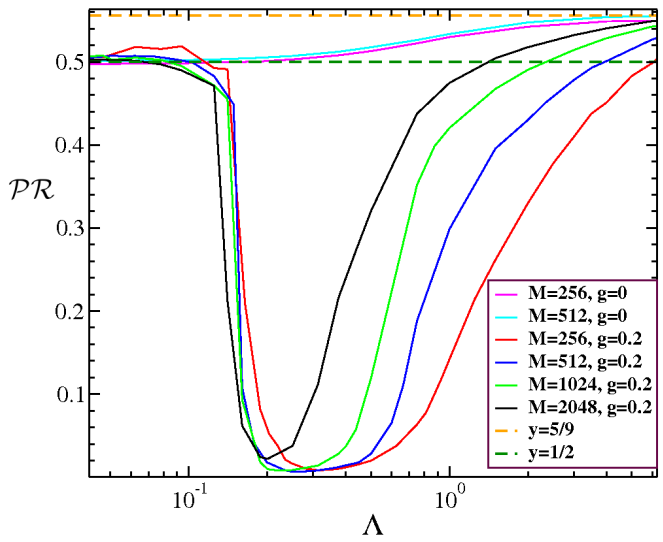

Figure 5.6: $\mathcal{PR}$ vs Λ. Numerical results confirm that in the two limits of Λ, $\mathcal{PR}$ converges to $1/2$ in the linear regime while it approaches $5/9$ in the strong nonlinearity regime. Sharp dips in the open systems (near $\Lambda_b \approx 0.25$) indicate the creation of the first breather. Power-law distribution of jumps has been observed for $\Lambda = \Lambda^* \sim \mathcal{O}(1)$, which is consistent with $\Lambda^* \geq 1$.

in two stages. The first stage involves a collision between a stationary DB and a moving DB (of density δp_{pert}), coming from the bulk of the lattice. In the second stage, a particle density δp_{out}, which is part of the moving DB, tunnels through the stationary DB and migrates to the other neighboring site of the DB. The tunneling density will travel towards the leaking edge of the OL and eventually decay in the form of an atomic burst, which gives rise to a jump in the survival probability.

During the tuneling process, the stationary breather is destabilized and migrates one lattice site inwards before it stabilizes again. One approach to understand the destabilization process and migration of DBs is through the idea of the Peierls-Nabarro (PN) barrier [176, 177]. In essence, high-amplitude excitations with a width of the order of the lattice constant are subjected to a strong spatially periodic force that impedes their movement. This barrier is due to the fact that the intermediate state of a migration process possesses a higher energy content. For a migration to occur, an external energy

source, such as that of a moving breather, is needed to provide temporary increase in the energy of the excitation. This effective pinning energy is not necessarily a fixed barrier caused by the lattice, but also in general depends on the amplitude of the excitation itself [178] together with the condition that the total number of particles in the excitation is conserved during the migration [69].

To give a more concrete illustration, we shall follow Ref. [177] and consider the two configurations: isolated peak (IP) and isolated bond (IB) (see top insets of Fig. 5.8). We start with the IP configuration (which can be seen as a simplified version of a static DB) with $|\psi_n|^2 = \delta_{n,l}\ A_d$, i.e. delta excitation at site l with density A_d. During the migration, the system has to be in an intermediate state of the IB configuration, with half of the particles transferred to site $l+1$, i.e. $|\psi_l|^2 = |\psi_{l+1}|^2 = A_d/2$. One can calculate the energy H_d associated with each configuration, as a function of the initial density at the peak A_d [177]. As we can see in Fig. 5.8, for $A_d < 4$, the IB configuration has higher energy content than the IP configuration, thus providing a energy barrier for migration to happen. Typical static breathers in our numerical simulations fall into this region. Therefore, a static DB, in the absence of external perturbation, stays localized due to its lack of energy to reach an intermediate state of a migration process. When a moving breather perturbs the static breather, it provides the additional energy to overcome the PN barrier, thus enabling a migration event to occur.

5.3.1 Relationship between δp_{out} and δp_{pert}

Since a jump in $P(t)$ corresponds to δp_{out} of an event, we would like to further investigate how δp_{out} is related to δp_{pert}, and strive to understand the physics of jumps through the perturbation. This analysis will prove to be essential for the study of the statistics of jumps later.

We have checked numerically that during a collision process, both the number of particles and the total energy of the three lattice sites ($M = 3$) of the stationary DB (that are

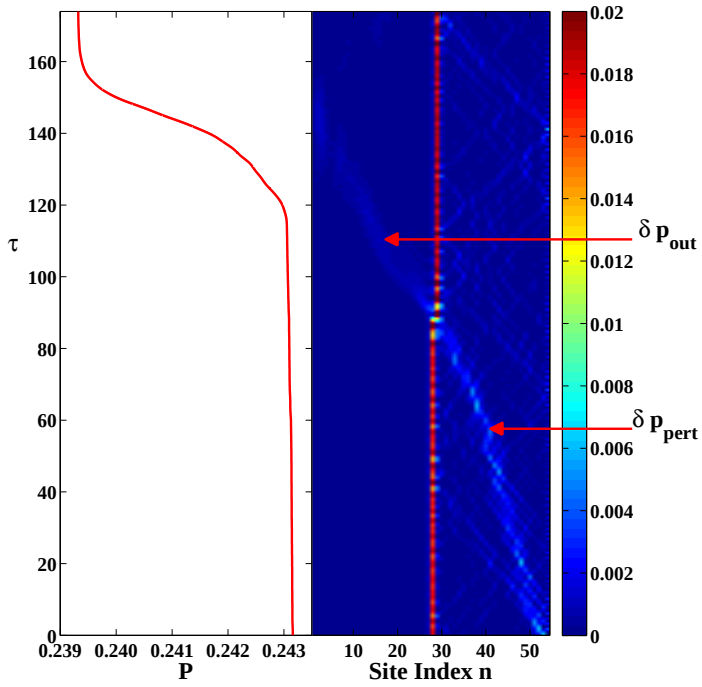

Figure 5.7: Snapshot of an avalanche event. On the left, we are plotting τ vs $P(\tau)$ whereas on the right we are plotting τ vs site index, with the color indicating $N_n(\tau)$ the atomic density at each site. A moving DB of density δp_{pert} comes in from the right and collides with the stationary breather. During the collision, the stationary breather gets destabilized and moves inwards while part of the moving DB (of density δp_{out}) tunnels through the stationary breather and travels towards the edge of the lattice. The arrival of the transmitted density at the edge registers a jump in the survival probability.

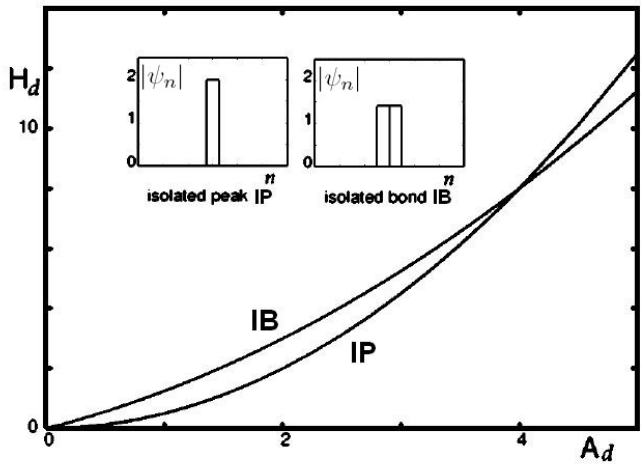

Figure 5.8: Energy H_d vs particle number A_d for IP and IB configuration. For $A_d < 4$, the IP configuration needs extra energy to move to the IB configuration. Since a migration process involves an intermediate IB configuration, in the absence of any external energy source, the excitation stays localized. If this energy mismatch is provided by external perturbation, migration is then allowed to occur. Top insets show an example for each configuration. Figure taken from [177].

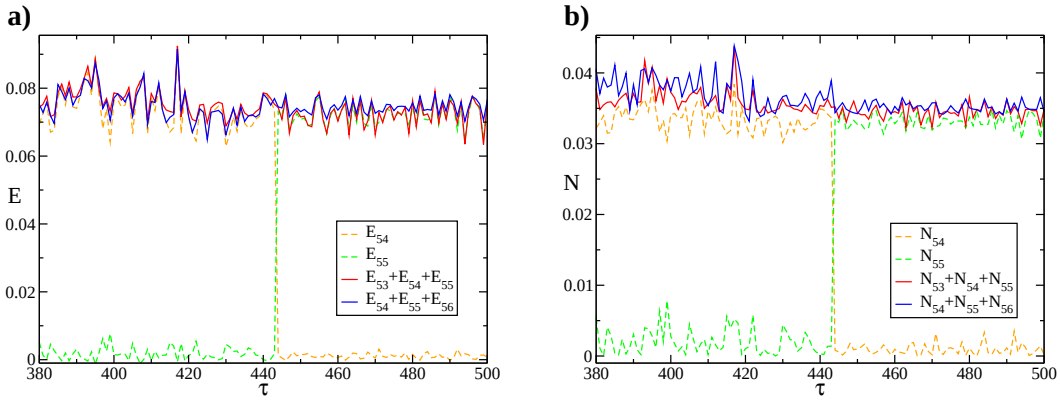

Figure 5.9: Energy and density vs time during an avalanche. Here, E_j is the energy and N_j is the density at site j. Initially the static breather is centered at site 54. At $\tau \approx 442$, an avalanche event is triggered, where the center of the breather migrates inwards to site 55, hence transferring the entire energy and density content to site 55. We observe that the total energy and density of the three sites before and after the avalanche are roughly conserved.

involved in the dynamics) are conserved (see Fig. 5.9). This enables us to turn the study of the collision process between stationary DB and moving breather into a perturbation problem of a reduced ($M = 3$) system [72], i.e. the closed trimer ($\gamma = 0$). In order to simulate a breather using a closed trimer, the initial atomic density is distributed among the three sites such that the system is in a self-trapped state [73, 179] at the second site. This can be easily done by having a large population imbalance between the middle site and each of the neighboring sites [73, 179]. Thus, with large population in the middle site, the closed trimer corresponds to a 3-site breather in our original extended system.

After evolving the trimer in the self-trapped state for some time, we introduce additional density δp_{pert} to the first site, which acts as a perturbation that corresponds to the role of the moving breather in the extended system. Then, the trimer continues to evolve for some time without any further perturbation. We calculate the maximum density that the third site achieves and register it as δp_{out}. We present our results in Fig. 5.10. For

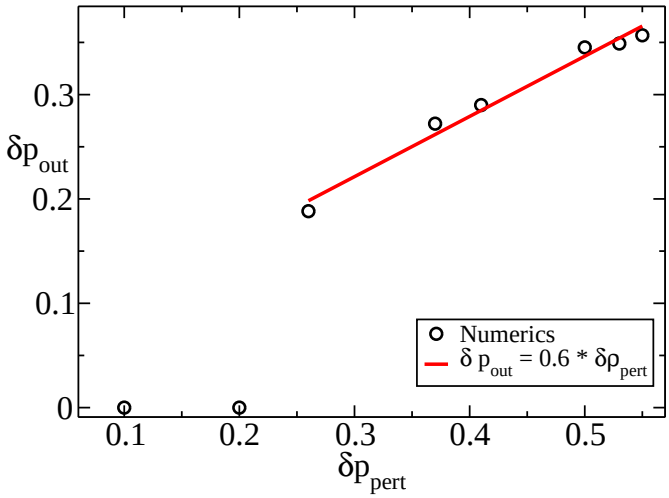

Figure 5.10: Simulation of an avalanche event using a closed trimer. We observed that the addition of $\delta p_{pert} \gtrsim 0.25$ to the first site destabilizes the self-trapped state. Some of the density tunnels through the second site and reaches the third site. We register the maximum density on the third site as δp_{out} and obtain $\delta p_{out} \propto \delta p_{pert}$.

$\delta p_{pert} < 0.25$, no density gets transmitted while above this threshold, one observes that part of the perturbation tunnels through to the third site, with the transmitted density being a fraction of the perturbation, i.e.

$$\delta p_{out} \propto \delta p_{pert} \ . \tag{5.11}$$

5.4 Statistics of Jumps: A Phase Space Picture

Equipped with an understanding of an avalanche event, we now develop a physical understanding on the origin of a power-law distribution of the jumps through an analysis of phase space structure of the reduced trimer system.

In Fig. 5.11, we show a Poincaré section for the trimer at $\Lambda \approx 1.0$, plotting N_2 vs $(\phi_3 - \phi_2)/\pi$ where ϕ's are the angles in Eq. (5.2). The Poincaré section corresponds to the plane $\phi_1 = \phi_3$ and $\dot{\phi}_1 > \dot{\phi}_2$ of the energy surface. It clearly shows a hierarchical mixed

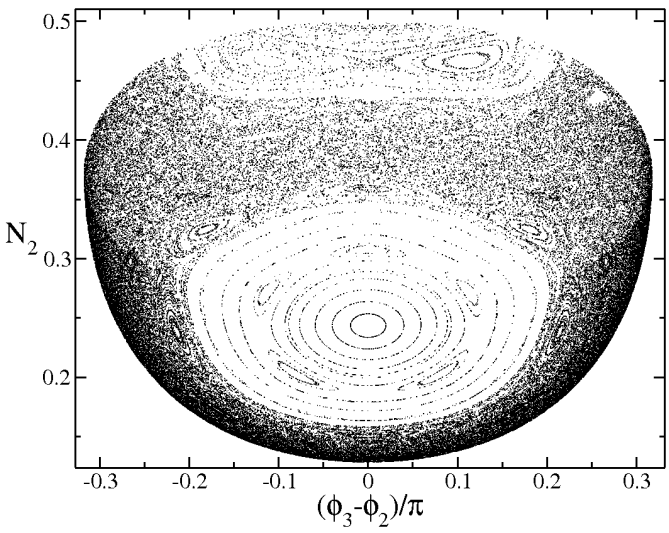

Figure 5.11: Poincaré section for a closed trimer at $\Lambda \approx 1.0$. The Poincaré plot is for the plane $\phi_1 = \phi_3$ and $\dot{\phi}_1 > \dot{\phi}_2$. The total energy of the three sites is chosen to be $E = 0.20$, corresponding to typical energy of a breather in our system.

phase space structure with islands of regular motion (tori) embedded in a sea of chaotic trajectories. Chaotic trajectories have continuous Fourier spectra, parts of which overlap with the linear spectrum of the lattice allowing for resonance phenomena with the linear excitations. In contrast, trajectories inside the islands correspond to stable DBs, provided that their frequency and its multiplies are outside the linear spectrum [72].

Therefore, the destabilization of a stationary DB by a lattice excitation (thermal fluctuation or a moving DB with density δp_{pert}) is possible only if the DB can be pushed out from the regular orbit across the island towards the chaotic sea. The particle's motion then becomes chaotic, allowing for a continuous Fourier spectra and thus for dramatic increase of frequency overlap with the phonon band. This destabilization process lets the pertubation tunnel through and reaches the leakage at the edges, triggering an avalanche.

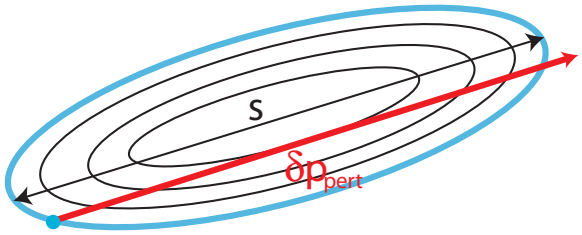

Figure 5.12: Illustration of the arguments leading to Eq. (5.12). The figure shows an island in a background of chaotic sea. Black ellipses correspond to regular orbits in an island, where s is the maximum diameter of the island. The blue ellipse is an example of a regular trajectory of a particle on the island, which corresponds to the case of a DB in our system. To destabilize the DB by pushing it to the chaotic sea and hence coupling it to the phonon bath, the perturbation strength has to be $\delta p_{pert} \sim s$.

Hence, in appropriate plot of Poincaré section[2], the perturbation δp_{pert} needed to destabilize a stationary DB follows the relation $\delta p_{pert} \propto s$ (see Fig. 5.12). Together with Eq. (5.11), we obtain $J \propto s$ and conclude that

$$\mathcal{P}(J) \sim \mathcal{P}(s). \tag{5.12}$$

Therefore, the task to understand the origin of the power-law distribution of jumps $\mathcal{P}(J)$ translates into the study of the distribution of island sizes $\mathcal{P}(s)$.

5.4.1 A Simple Hierarchical Model

Let us consider a simple hierarchical mixed phase space in d dimensions. Let us assume that, due to self-similar structure of the mixed phase space, there exists a well-defined main island of linear size s_k (e.g. the diameter) at each hierarchy level k, with n_k number of sub-islands for each main island (see Fig. 5.13 for illustration). Defining $f_k = \frac{s_{k-1}}{s_k}$, which is the fraction of sizes of main island to sub-island at hierarchy level

[2]Note that in the reduced $M = 3$ system, Arnold diffusion is prohibited.

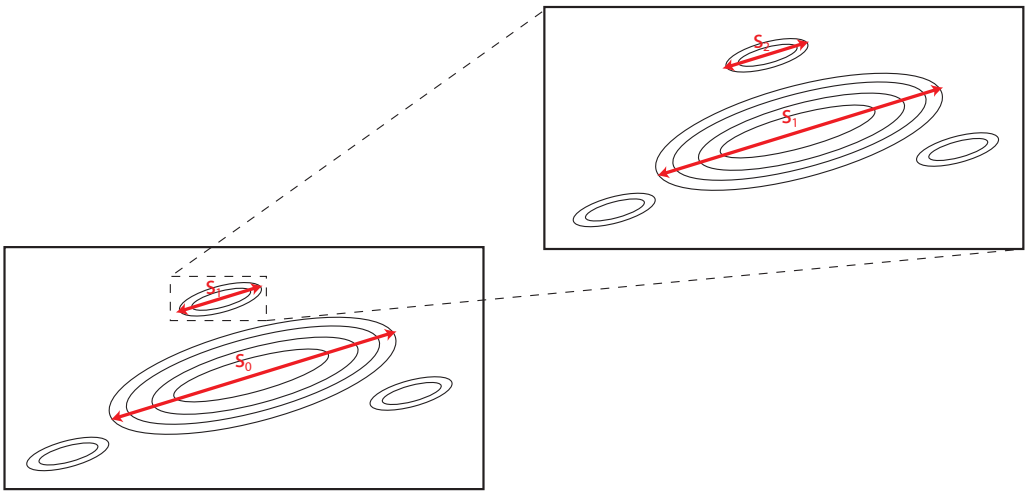

Figure 5.13: Illustration of the simple hierarchical model. This figure shows the example of $n = 3$. The 0-th level main island has diameter s_0 and is surrounded by $n = 3$ sub-islands of size s_1, in a background of chaotic sea. Due to self-similarity, if we zoom into one of the sub-islands, we would recover the self-similar structure of the islands but now with the main island being in the $k = 1$ level with s_1 diameter, surrounded by another $n = 3$ sub-subislands with diameter s_2.

k, we get

$$s(k) = \frac{s_0}{\prod_{i=1}^{k} f_i}. \tag{5.13}$$

The total number of islands up to level k reads

$$p(k) = \prod_{i=1}^{k} n_i \,. \tag{5.14}$$

Without loss of generality, we set $s_0 = 1$, and consider the simplified case of $n_i = n$ and $f_i = f$. Then, $s(k) = f^{-k}$ and $p(k) = n^k$, leading to

$$p(s) = n^{k(s)} = s^{-\frac{\ln n}{\ln f}}, \tag{5.15}$$

where $k(s) = -\frac{\ln s}{\ln f}$.

Thus, for this simple model, we obtain a power law distribution of island size

$$p(s) = s^{-\alpha} \,, \tag{5.16}$$

where $\alpha = -\frac{\ln s}{\ln f}$.

Due to self-similar structure of the phase space, we request that the total number of island diverges. This implies that the integral

$$\int_{s}^{s_{max}} p(s')ds' = s^{-\alpha+1} - s_{max}^{-\alpha+1} \tag{5.17}$$

must diverge for $s \to 0$, leading to

$$\alpha > 1. \tag{5.18}$$

On the other hand, we also request that the total volume of the islands to be finite as the volume of the phase space is finite as well. Specifically, the integral

$$\int_{s}^{s_{max}} (s')^d p(s')ds' \propto s^{-\alpha+1+d} - s_{max}^{-\alpha+1+d} \tag{5.19}$$

has to converge in the limit of $s \to 0$. This requirement leads to the following upper bound for α

$$\alpha < 1 + d \tag{5.20}$$

where d is the dimension of the phase space.

Summarizing the two bounds for the power-law exponent α, we obtain

$$1 < \alpha < 1 + d. \tag{5.21}$$

Thus, for a 2-dimensional phase space, the exponent is expected to be bounded by

$$1 < \alpha < 3 \ . \tag{5.22}$$

We were able to test the above hypothesis on the power-law distribution of island sizes and the bounds in Eq. (5.22) using the kicked rotor. Leaving aside the technicality in the numerical calculation (which is provided in Appendix G), the distribution of the island sizes indeed follows a power-law with $\alpha \approx 1.42$. This is consistent with the bounds in Eq. (5.22). Moreover, as shown in Fig. 5.5, for the DNLSE with dissipation, we obtain a power-law jump distribution with $\alpha \approx 1.86$, which is also in agreement with the bounds given above.

5.5 Conclusions

In conclusion, we have studied the dynamics of BECs in leaking OLs. In particular, we have observed the existence of avalanches in the decay of the atomic population , and provided an explanation of these events using the scenario of a collision process involving a stationary breather and a moving breather. We have found that for a certain range of (a rescaled) nonlinearity $\Lambda^* \sim \mathcal{O}(1)$, there exists a power-law distribution $\mathcal{P}(J) \sim J^{-\alpha}$ for the avalanche, suggesting the existence of a phase transition. We further propose an order parameter $\mathcal{PR}$ which measures the relative number of sites that are occupied by DBs. We have linked the observed power-law distribution of jumps to the hierachical structure of a mixed phase space shown by a reduced system of three nonlinear coupled oscillators. In particular, we have argued that the statistics of jumps

is equivalent to the statistics of island size in this mixed phase space and constructed a simple hierarchical model that shows a power-law distribution of island sizes. This model provides bounds $1 < \alpha < 3$ for the power-law exponent, which are consistent with the power-law distribution of island sizes found in the mixed phase space of the kicked rotor and our power-law jump distribution in the BECs in leaking OLs.

Chapter 6

Conclusions and Outlooks

In conclusion, we have studied wave dynamics and stability of complex systems with a localization-delocalization phase transition, which can be created by tuning an internal or external parameter. Examples are random media where the disorder strength drives the system from a metallic to an insulating phase, a singular potential in classically chaotic systems or a local nonlinearity induced by particle-particle or wave-matter interactions. Due to the fact that at the transition (critical) point, the system shows a scale-free behavior, various interesting statistical properties of the energies and wavefunctions emerge. These have direct influences in the dynamics exhibited by the system.

This thesis was presented in three main parts. In the first part, we have investigated the fidelity decay for systems at the Anderson Metal-Insulator Transition. This quantity measures the stability of the dynamics to external perturbations. Depending on the perturbation strength x, we have identified two main regimes: The Linear Response Theory regime, where perturbation theory is applicable, and the nonperturbative regime. In the latter regime, we have found a novel decay law for the fidelity, which reflects the critical nature of the system.

Next, we studied wavepacket dynamics of the Harper model at a metal-insulator transition and identified the effects of nonlinearity (induced by interatomic or wave-matter interactions) in wavepacket dynamics. Specifically, we have obtained bounds for the power-law exponent of the temporal spreading of the wavepacket variance. These bounds are dictated by the fractal dimension of the LDoS of the linear system at crtically. Above some nonlinearity strength, this nonlinear spreading appears and persists up to time $t^* \sim \chi^{1/D_2^{\mu}}$, which depends parametrically on the nonlinearity strength. After this time, the linear spreading of the second moment is restored while other moments remain affected by the nonlinearity. We also found a scaling relation for the central part of the evolving profile that applies to any time and any nonlinearity strength.

The last part of the thesis deals with the decay process of atomic BECs from leaking optical lattices and the existence of rare events such as avalanches (or jumps) in the outgoing atomic flux. For a certain range of (rescaled) nonlinearity $\Lambda^* \sim \mathcal{O}(1)$, there exists a power-law distribution $\mathcal{P}(J) \sim J^{-\alpha}$ for the avalanches, suggesting the existence of a phase transition. We propose an explanation of this phenomenon based on the phase-space analysis of a reduced three-site system that captures the dynamics of an avalanche event. In particular, we argue that the statistics of jumps is equivalent to the statistics of island size in the mixed phase space of the three-site model. To this end, we have constructed a simple hierarchical model which mimics the 'island-over-island' self-similar structure of a mixed phase-space and gives a power-law distribution of island sizes. Our heurestic modeling allows us to provide bounds on the observed power-law exponent α, i.e. $1 < \alpha < 3$. These bounds are consistent with our observed power-law jump distribution in the BECs in leaking optical lattices.

There is still plenty of work to be done for future research along the direction of this thesis' studies. Despite the success of the RMT approach, the applicability of RMT in modeling dynamical systems at criticality still remains a matter of conjecture. One should be careful under which conditions RMT is applicable. Specifically, one should be aware that there is a hierarchy of challenges where the applicability of the RMT

conjecture should be tested, namely the study of spectral statistics, the study of eigenstates, and the study of quantum dynamics. While the former two issues have been studied extensively [50], the aspect of dynamics is barely treated. As a continuation of the fidelity study of critical systems, we are currently in the process of studying a periodically kicked rotor with a logarithmic potential singularity [180]. The main focus of this on-going project will be to address the issue of correspondence between the RMT model and a dynamical system with critical behavior within the framework of fidelity. Since such system possesses a well-defined classical limit, it is of interest to see up to which point the RMT predictions are valid.

As for the study of wavepacket dynamics, recently there has been much interest in the study of disordered DNLSE [120,121] in this direction. However, the focus of these works have been in the localized regime. It is of immense interest to study the wavepacket dynamics of Anderson systems at critical conditions, such as three dimensional random media at the Anderson Metal-Insulator Transition, in the presence of nonlinearity. We hope that our results of the nonlinear Harper model will shed some light on the interplay of nonlinearity and criticality in these systems.

Finally, on the outlook of future work on the DNLSE with leaking boundaries, many issues in our current work demand more rigorous studies and clarifications. In particular, the distribution of island sizes in mixed space is itself a very important question relevant in various areas in physics. Although the conjecture of power-law distribution of island sizes has been verified numerically in the kicked rotor and our heuristic model provided a satisfactory explanation, more rigorous work along this direction is needed. In addition, the nature and the origin of the phase transition remains an open question, especially on the aspects of symmetry-breaking study and the phase diagram analysis of this system. Another interesting future direction is to investigate the link of the observed phase transition to the physics of self-organized criticality.

The study of wave propagation in complex media is indeed an exciting scientific arena.

Recent experimental achievements in optics and atomic physics have pushed forward our understanding in this area, but at the same time opened up many new and intriguing questions. Among them, one of the most prominent questions would be to understand the interplay between nonlinearity (induced by matter-wave or particle-particle interactions) and disorder. As the poet said, "Hope that your road to Ithaka will be long, full of adventure, full of discovery", so too is the exciting path of scientific endeavor in this direction.

Appendix A

Level Spacing Distributions

We shall now proceed with the calculation, which is often called Wigner's surmise, using 2×2 matrices to predict the distribution of the level spacings $P(S)$ in the GOE and GUE cases. This calculation is based on the discussion in Ref. [78].

Let the Hamiltonian be

$$\mathbf{H} = \begin{pmatrix} H_{11} & H_{12} \\ H_{12}^* & H_{22} \end{pmatrix} = \begin{pmatrix} a+b & x+iy \\ x-iy & a-b \end{pmatrix} \qquad a, b, x, y \in \mathbb{R}.$$

In the GOE case, $\mathbf{H}$ is real and symmetric so y vanishes, whereas for the GUE case $y \neq 0$. Since there are only two eigenvalues associated with a 2×2 matrix, there is only one level spacing to be considered

$$S = E_2 - E_1 = \sqrt{b^2 + x^2 + y^2}. \tag{A.1}$$

Assuming a Gaussian distribution W for the variables b, x and y, we obtain in the GOE

case

$$\begin{aligned} P(S) &= \int_{-\infty}^{\infty}\int_{-\infty}^{\infty} db\ dx\ W(b,x)\ \delta(S-\sqrt{b^2+x^2}) \\ &= 2\pi\int_0^{\infty} dr\ r\frac{1}{\sqrt{2\pi}\sigma}\ e^{-\frac{r^2}{2\sigma^2}}\ \delta(S-r) \\ &= \frac{\sqrt{2\pi}}{\sigma}\ S\ e^{-\frac{S^2}{2\sigma^2}} \\ &= \frac{\pi}{2}S\ e^{-\frac{\pi}{4}S^2} \end{aligned} \tag{A.2}$$

where in the last step, we used the normalization condition of probability function $P(S)$.

Applying the same calculation for the GUE case leads to

$$\begin{aligned} P(S) &= \int_{-\infty}^{\infty}\int_{-\infty}^{\infty}\int_{-\infty}^{\infty} db\ dx\ dy\ W(b,x,y)\ \delta(S-\sqrt{b^2+x^2+y^2}) \\ &= 4\pi\int_0^{\infty} dr\ r^2\frac{1}{\sqrt{2\pi}\sigma}\ e^{-\frac{r^2}{2\sigma^2}}\ \delta(S-r) \\ &= \frac{\sqrt{8\pi}}{\sigma}\ S^2\ e^{-\frac{S^2}{2\sigma^2}} \\ &= \frac{32}{\pi^2}S^2\ e^{-\frac{4}{\pi}S^2}\ . \end{aligned} \tag{A.3}$$

For the case of GSE, one would use a 4×4 matrix and obtain the result

$$P(S) = \frac{2^{18}}{3^6\pi^3}S^4 e^{-\frac{64}{9\pi}S^2}. \tag{A.4}$$

For the sake of completeness, let us calculate the level spacing distribution for an integrable system, where the number of constants of motion equals the number of degrees of freedom. It turns out that the matrix representation of the corresponding Hamiltonian takes a diagonal form due to symmetry considerations. As each eigenvalue corresponds to its own symmetry class, it is reasonable to assume that they are uncorrelated. Therefore, the probability $P(S)dS$ to find an eigenvalue in the interval $[S, S+dS]$, but not in $[0, S]$, can be easily calculated. We divide the interval $[0, S]$ into N equidistant subintervals of length S/N. Since the eigenvalues are uncorrelated, the probability to find *no*

eigenvalue in the interval $[0, S]$ can be written as $\lim_{n\to\infty}\left(1-\frac{S}{N}\right)^N$. Hence, we derive the probability of finding an eigenvalue in the interval $[S, S+dS]$

$$P(S)dS = \lim_{N\to\infty}\left(1-\frac{S}{N}\right)^N dS \tag{A.5}$$

where upon evaluating the limit gives the Poisson nearest neighbor distribution

$$P(S) = e^{-S}. \tag{A.6}$$

Appendix B

Derivation of the DNLSE in Nonlinear Waveguides

Here, we follow the discussion in [9] and consider a system of coupled nonlinear waveguides (see Figure B.1).

From Ref. [181], the amplitude $a_\mu^{(n)}$ of the μth mode of the nth guide satisfies the following equation

$$-i\frac{da_\mu^{(n)}}{dz} = \frac{\omega}{4P_\mu}\int dx\ dy\ \mathbf{E}_\mu^{(n)} \cdot \mathbf{P}', \tag{B.1}$$

where the axes of the guides are along the z direction, $\mathbf{E}_\mu^{(n)}$ the electric field of the μth mode in the nth guide, P_μ is the power in the μth mode and $\mathbf{P}'$ is the perturbing polarization due to linear and nonlinear effects. The nth guide has the perturbing polarization that reads

$$\mathbf{P}'/\varepsilon_0 = \mathbf{E}^{(n)}\delta + (\delta+\varepsilon)\left[\mathbf{E}^{(n+1)} + \mathbf{E}^{(n-1)}\right] + \chi^{(3)}\left[|\mathbf{E}^{(n)}|^2 + |\mathbf{E}^{(n-1)}|^2 + |\mathbf{E}^{(n+1)}|^2\right]\mathbf{E}^{(n)}, \tag{B.2}$$

where ε is the dielectric constant of the host material, $\varepsilon+\delta$ that of the guide material, $\mathbf{E}^{(i)}$ the total field contributed by the ith guide and $\chi^{(3)}$ is the third-order susceptibility [11]. Substituting Eq. (B.2) into Eq. (B.1) then yields

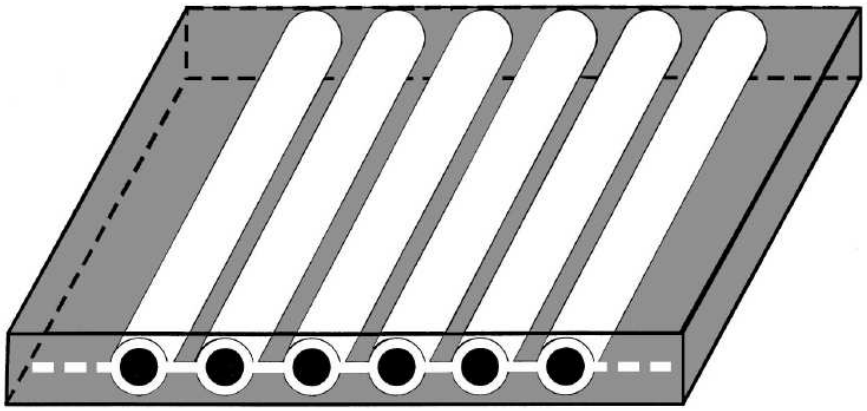

Figure B.1: A system of coupled nonlinear waveguides extending in the z-direction. Figure from [9].

$$\begin{aligned} -i\frac{da_\mu^{(n)}}{dz} &= \frac{\omega\varepsilon_0}{4P_\mu}\int dxdy\left[\delta\left(\mathbf{E}_\mu^{(n)}\right)^*\cdot\mathbf{E}^{(n)}+(\varepsilon+\delta)\left(\mathbf{E}_\mu^{(n)}\right)^*\cdot\left(\mathbf{E}^{(n-1)}+\mathbf{E}^{(n+1)}\right)\right. \\ &\quad \left.+\chi^{(3)}\left(|\mathbf{E}^{(n)}|^2+|\mathbf{E}^{(n-1)}|^2+|\mathbf{E}^{(n+1)}|^2\right)\left\{\left(\mathbf{E}_\mu^{(n)}\right)^*\cdot\mathbf{E}^{(n)}\right\}\right]. \end{aligned} \tag{B.3}$$

If we assume that we are working with the lowest single-mode for each guide, such that $\mathbf{E}^{(n)} = a_1^{(n)}\mathbf{E}_1^{(n)}$ and thus Eq. (B.3) turns into

$$-ida_1^{(n)}/dz = Q_1^{(n)}a_1^{(n)} + Q_{n,n-1}a_1^{(n-1)} + Q_{n,n+1}a_1^{(n+1)} + Q_3^{(n)}|a_1^{(n)}|^2a_1^{(n)} \tag{B.4}$$

with coefficients

$$Q_1^{(n)} = \frac{\omega\varepsilon_0}{4P_1}\int dxdy\delta|\mathbf{E}^{(n)}|^2\,, \tag{B.5}$$

$$Q_3^{(n)} = \frac{\omega\varepsilon_0}{4P_1}\chi^{(3)}\int dxdy\delta|\mathbf{E}^{(n)}|^4\,, \tag{B.6}$$

$$Q_{nl} = \frac{\omega\varepsilon_0}{4P_1}\int dxdy(\varepsilon+\delta)\left(\mathbf{E}^{(n)}\right)^*\cdot\mathbf{E}^{(l)}, \quad (n\neq l). \tag{B.7}$$

$$\tag{B.8}$$

Here, we assume that these coefficients are uniform for each wave guide, such that $Q_1 = Q_1^{(n)}$, $Q_{n,n-1} = Q_{n,n+1} = -V$ and $Q_3^{(n)} = Q_3$ for all n. Then, Eq. (B.4) turns into

(dropping the subscript '1')

$$-ida^{(n)}/dz = Q_1 a_1^{(n)} - V(a^{(n-1)} + a^{(n+1)}) + Q_3|a^{(n)}|^2 a^{(n)}. \tag{B.9}$$

Now, writing $a^{(n)}$ in terms of power and phase variables, $a^{(n)} = \psi_n\sqrt{P}\exp(iQ_n z)$ where P is the total input power and further transforming $\gamma = -Q_3 P$, we arrive at

$$i\frac{d\psi_n}{dz} = \gamma|\psi_n|^2\psi_n + V(\psi_{n+1} - \psi_{n-1}) \tag{B.10}$$

which is just the DNLSE in Eq. (2.50), disguised with the time replaced by the z coordinate and the other variables transformed accordingly. Here, the analogue of norm conservation in the DNLSE is the power conservation

$$\sum_n |\psi_n|^2 = 1. \tag{B.11}$$

These nonlinear coupled waveguides are good candidates for optical switching purpose. In nonlinear lattice, the effect of self-trapping is generic so that in the nonlinear waveguides, the self-trapping effect could be used in the design of optical ultrafast switches with applications in optical computers [10, 181].

Appendix C

Application of the DNLSE in Bose-Einstein Condensates

Here, we shall follow the derivation in [78] of the DNLSE in the decription of BECs loaded in an optical lattice.

To preserve atomic gases in its metastable phase for sufficiently long time, during laser and evaporative cooling, the density of the particle is kept very low (around 10^{14-16} particles/cm^3). This is possible in dilute and cold gases, and as a result three-body collisions are rare events, allowing us to consider only two-body collisions, which can be described by s-wave scattering processes [12].

In the second quantization, the many-body Hamiltonian describing N interacting bosons confined by an external potential is given by

$$\begin{aligned} \hat{H} &= \int d\mathbf{r}\ \hat{\Psi}^\dagger(\mathbf{r}) \left[-\frac{\hbar^2}{2m}\nabla^2 + V_{\text{lat}}(\mathbf{r}) + V_{\text{ext}}(\mathbf{r}) \right] \hat{\Psi}(\mathbf{r}) \\ &\quad + \frac{1}{2} \int\int d\mathbf{r}\ d\mathbf{r}' \hat{\Psi}^\dagger(\mathbf{r}) \hat{\Psi}^\dagger(\mathbf{r}') V(\mathbf{r}-\mathbf{r}') \hat{\Psi}(\mathbf{r}') \hat{\Psi}(\mathbf{r}) \end{aligned} \tag{C.1}$$

where $\hat{\Psi}(\mathbf{r})$ and $\hat{\Psi}^\dagger(\mathbf{r})$ are the bosonic field operators that annihilate and create a particle

at position $\mathbf{r}$ respectively, $V(\mathbf{r}-\mathbf{r}')$ is the two-body inter-atomic potential, $V_{\text{lat}}(\mathbf{r})$ is the optical lattice potential and $V_{\text{ext}}(\mathbf{r})$ describes a possibly additional potential that is slowly varying along the lattice such as the magnetic trap used for evaporative cooling.

Since the dominant inter-atomic interaction comes from s-wave scattering and that the particle density is very low, we can approximate two-body interaction potential $V(\mathbf{r}-\mathbf{r}')$ with a delta-like potential [182]

$$V(\mathbf{r}-\mathbf{r}') \approx \frac{4\pi a_s \hbar^2}{m} \times \delta(\mathbf{r}-\mathbf{r}') \tag{C.2}$$

where a_s is the s-wave scattering length and m is the atomic mass.

With this simplification, we take advantage of the periodic nature of a lattice, i.e. $V_{\text{lat}}(\mathbf{r}) = V_{\text{lat}}(\mathbf{r}+\mathbf{d})$ with lattice vector $\mathbf{d}$. For a *single* atom moving in a potential V_{lat}, we have the Bloch functions $\phi_{\mathbf{q},n}(\mathbf{r}) = e^{i\mathbf{q}\mathbf{r}} u_{\mathbf{q},n}(\mathbf{r})$ with $u_{\mathbf{q},n}(\mathbf{r})$ having the same periodicity as the lattice and $\mathbf{q}$ the quasi-momentum.

Since this work is interested only in the deep lattices, as many experiments are [151,183], it is convenient to work in the Wannier basis where the eigenfunctions are localized at each lattice site. The Wannier-functions are obtained via a uniform transformation of the Bloch basis and reads

$$w_n(\mathbf{r}-\mathbf{r}_i) = \frac{1}{\sqrt{f}} \sum_{\mathbf{q}} e^{-i\mathbf{q}\mathbf{r}_i} \phi_{\mathbf{q},n}(\mathbf{r}) \tag{C.3}$$

where the sum is taken over the quasi-momentum in the first Brillouin zone and f is the number of lattice sites.

Assuming the lattice is deep enough such that the chemcial potential is too small to excite states outside the first Bloch band [184], we can thus expand the field operator $\hat{\Psi}$ in the Hamiltonian (C.1) in the Wannier basis $w_n(\mathbf{r}-\mathbf{r}_i)$, keeping only the lowest band

$$\hat{\Psi}(\mathbf{r}) = \sum_{i=1}^{f} \hat{b}_i w_0(\mathbf{r}-\mathbf{r}_i) \tag{C.4}$$

where $\hat{b}_i$ is the bosonic annhilation operator at site i.

Substituing Eq. (C.4) into Eq. (C.1) yields the Bose-Hubbard Hamiltonian(BHH) [184]

$$\hat{H} = \sum_{i=1}^{f} \nu_i \ \hat{b}_i^\dagger \ \hat{b}_i + \frac{1}{2} \sum_{i=1}^{f} U_i \ \hat{b}_i^\dagger \ \hat{b}_i^\dagger \ \hat{b}_i \ \hat{b}_i - \sum_{<i,j>} k_{ij} \ \hat{b}_i^\dagger \ \hat{b}_j \tag{C.5}$$

with $< i, j >$ denoting summation over adjacent sites $j = i \pm 1$, and the following parameters

$$\begin{aligned} \nu_i &= \int d^3r \ V_{\text{ext}}(\mathbf{r}) |w_0(\mathbf{r} - \mathbf{r}_i)|^2 \\ U_i &= \frac{4\pi a_s \hbar^2}{m} \int d^3r \ |w_0(\mathbf{r} - \mathbf{r}_i)|^4 \\ k_{ij} &= \int d^3r \ w_0^*(\mathbf{r} - \mathbf{r}_i) \left[-\frac{\hbar^2}{2m} \nabla^2 + V_{\text{lat}}(\mathbf{r}) \right] w_0(\mathbf{r} - \mathbf{r}_{j=i\pm1}). \end{aligned} \tag{C.6}$$

From the canonical commutator relations of the bosonic operators $\hat{b}_i$ and $\hat{b}_i^\dagger$

$$[\hat{b}_i, \hat{b}_j^\dagger] = \delta_{i,j} \ , \tag{C.7}$$

and the number operator, defined as

$$\hat{n}_i = \hat{b}_i^\dagger \hat{b}_i, \tag{C.8}$$

we then reach the following

$$\hat{H} = \sum_{i=1}^{f} \nu_i \ \hat{n}_i + \frac{1}{2} \sum_{i=1}^{f} U_i \ \hat{n}_i \ (\hat{n}_i - 1) - \sum_{<i,j>} k_{ij} \ \hat{b}_i^\dagger \ \hat{b}_j \tag{C.9}$$

The ν_i and U_i are the on-site potential and the on-site interaction strength at site i respectively while k_{ij} accounts for the coupling strength that describes the tunneling effect of particle between neighboring sites, which also represents the kinetic energy.

We would like to investigate the semiclasssical limit of the BHH. For simplicity's sake, let us set $U_i = U$ and $k_{ij} = k$ for all i for uniform interaction strength and tunneling rate across the whole lattice. While taking the classical limit $N \to \infty$, we would want the

interaction strength U to be taken into consideration properly. Let us define rescaled creation and annihilation operators

$$\hat{c}_i^\dagger = \frac{1}{\sqrt{N}}\hat{b}_i^\dagger \ ; \qquad \hat{\tilde{n}}_i = \frac{1}{N}\hat{n}_i, \tag{C.10}$$

with N being the total number of bosons. This then leads to the following Hamiltonian

$$\frac{\hat{H}}{N} = \sum_{i=1}^{f} \nu_i \ \hat{\tilde{n}}_i + \frac{UN}{2}\sum_{i=1}^{f} \ \hat{\tilde{n}}_i \ (\hat{\tilde{n}}_i - \frac{1}{N}) - k \sum_{<i,j>} \hat{c}_i^\dagger \hat{c}_j. \tag{C.11}$$

Hence, the appropriate classical limit corresponds to keeping both UN and k constant to preserve the same *effective nonlinearity* in the dynamics.

Now we have the following commutator relations for the rescaled operators

$$[\hat{c}_i, \hat{c}_j^\dagger] = \frac{1}{N}\delta_{i,j} \ , \tag{C.12}$$

which vanishes for large particle number N. Therefore since these two operators commute in the limit $N \to \infty$, we can treat them as c-number.

Now taking the classical limit of $N \to \infty$ but keeping both UN and k constant to obtain the classical Hamiltonian $\mathcal{H}$, we express the c-numbers as

$$\hat{c}_j \mapsto \psi_j \ ; \qquad \hat{c}_j^\dagger \mapsto \psi_j^*, \tag{C.13}$$

where the ψ_j and ψ_j^* are complex amplitudes.

Putting this into Hamiltonian (C.11) leads to

$$\tilde{\mathcal{H}} = \frac{\mathcal{H}}{N} = \sum_{i=1}^{f} \nu_i \ |\psi_i|^2 + \frac{UN}{2}\sum_{i=1}^{f} \ |\psi_i|^4 - k \sum_{<i,j>} \psi_i^* \ \psi_j \ . \tag{C.14}$$

The amplitudes are conjugate variables with respect to the Hamiltonian $i\tilde{\mathcal{H}}$ giving the canonical equations

$$i\frac{\partial \psi_j}{\partial t} = \frac{\partial \tilde{\mathcal{H}}}{\partial \psi_j^*} \ ; \qquad \frac{\partial \psi_j^*}{\partial t} = -\frac{\partial \tilde{\mathcal{H}}}{\partial \psi_j}, \tag{C.15}$$

resulting in the equations of motion:

$$i\frac{\partial \psi_j}{\partial t} = UN|\psi_j|^2\psi_j + \nu_j\psi_j - k(\psi_{j+1} + \psi_{j-1}). \tag{C.16}$$

This is then the DNLSE in Eq. (2.50) with appropriate variable changes.

Appendix D

Fidelity and Decoherence

It is often the case that a quantum system is not perfectly isolated from its environment. The interaction of the system with the environment then influences the outcome of the experiment. In particular, since interference is a very essential and important phenomenon in quantum mechanics, one would like to understand how the enviroment affects interference phenomena in quantum systems. The study of how decoherence, i.e. the loss of interference, is induced through interaction with the environment is indeed a fundamental question in quantum mechanics. Following Ref . [78], we shall discuss the role of fidelity as a measure of decoherence in the prototype example of interference experiment – the Aharonov-Bohm (AB) ring [82, 83] experiment.

A schematic illustration of the AB ring experiment is presented in Fig. D.1. A charge particle travels through a ring geometry from point A to point B either by taking the left path or the right path. One recognizes immediately that this is the familiar double-slit experiment with appropriate interpretations on the physical set-ups. A perpendicular magnetic field is present inside the ring and it is further assumed that the interaction of the system with the bath (i.e. the environment) only occurs along the right path and that the back-reaction of the bath on the system is small [82]. Since this is a two-path experiment, one would expect to observe interference pattern at point B. In the

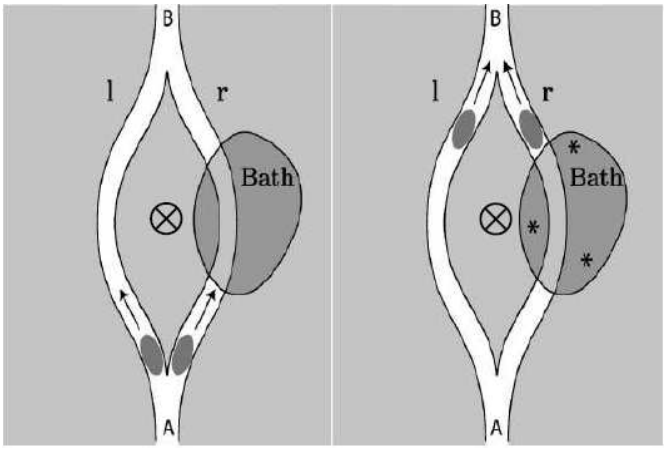

Figure D.1: Schematic illustration of the AB-ring experiment where a particle travels from point A to B through a ring geometry with a perpendicular magnetic field. At B, the interference is measured and the particle can arrive at B through either the left or the right path. The interaction of the system with the bath is assumed to occur along the right bath only. The presence of the bath will affect interference pattern at point B. Figure from [83].

beginning of the experiment, where time $t = 0$, we can describe the whole set-up, i.e. the system with the bath, as a direct product of the system's state with the initial state of the bath $\chi_0(\eta)$ where η is the internal degress of freedom of the bath. The system's state is a superposition of the left path $l(x,t)$ and the right path $r(x,t)$ leading to the overall state

$$\psi_A(t=0) = [l(x=A,t=0) + r(x=A,t=0)] \otimes \chi_0(\eta) \tag{D.1}$$

Assuming the particle will arrive at point B after time T taking either of the path, the wavefunction at point $x = B$ is described by

$$\psi_B(T) = l(B,T) \otimes \chi_l(\eta) + r(B,T) \otimes \chi_r(\eta) \tag{D.2}$$

where in general the bath's state will evolve differently depending on which path the particle takes.

One then can examine the interference term which is just

$$2\ \Re[l^*(B,T)\ r(B,T)] \int d\eta\ \chi_l^*(\eta)\chi_r(\eta) \tag{D.3}$$

where the integration is done over the bath's degrees of freedom because in experiment, one measures only the state of the system and therefore has no information on the state of the bath. Hence, one has to sum over all possible states of the bath and thus 'traces' over the bath.

In the case where the particle has no interaction with the bath, then $\chi_l = \chi_r$ and the integral in Eq. (D.3) will be unity. One then recovers the expression $2\ \Re[l^*(B,T)\ r(B,T)]$ in the standard AB-ring experiment in the absence of interaction with the environment. In the presence of coupling with the bath, however, this term is multiplied by a factor which takes complex values with norm between zero and unity. In the extreme case of this factor being zero, interference pattern is lost !

It is then natural to define this factor as a measure of decoherence. In fact, the *fidelity amplitude* is defined through this multiplicative factor and its absolute-value-square gives the fidelity

$$F(t) = \left| \int d\eta\ \chi_l^*(\eta)\chi_r(\eta) \right|^2 \tag{D.4}$$

Here, the connection between fidelity and decoherence is clear: Fidelity quantifies the strength of interference where high fidelity is equivalent to more dominant interference and low fidelity corresponds to loss of interference.

Here, the interpretation of fidelity is two-fold. One can see it from the perspective of the system or of the environment. In the former interpretation, the partial wave $r(x,t)$ acquires an additional phase due to interaction with the possible dynamics and state of the bath. At the extreme case where this phase is $\pi/2$, the effect is such that the interference is destroyed, leading to complete decoherence. Adopting the latter interpretation from the perspective of the environment, if the bath is not affected by the moving particle, then the interference pattern remains unchanged. However, if the

bath is affected by the particle's motion, then one could extract information about the particle's path. The extreme case, where one knows exactly which path the particle has taken, corresponds to a complete loss of the interference pattern. This reminds us again of the familiar double-slit experiment, where information about the particle's path will cause intereference pattern to be lost.

Appendix E

Derivation of x_c and x_{prt} for the WLRM models

We follow the discussion in Ref. [110] to derive x_c and x_{prt} in the framework of local density of states (LDoS) analysis. The LDoS is a major tool for characterizing parametric evolution of eigenstates. Recall that for the WLRM model, we are dealing with Hamiltonian of the type

$$\mathbf{H} = \mathbf{H_0} + x\mathbf{B}. \tag{E.1}$$

with variance of $\mathbf{B}$ given by

$$\langle \sigma_{nm}^2 \rangle = \frac{1}{1 + |\frac{n-m}{b}|^2}. \tag{E.2}$$

The overlap of the eigenstate $|n(x)\rangle$ (for a given perturbation strength x) with the eigenstate $|m(0)\rangle$ of $x = 0$ Hamiltonian (i.e. the unperturbed Hamiltonian $\mathbf{H_0}$) is given by

$$P(n|m) = |\langle n(x)|\, m(0)\, \rangle|^2 . \tag{E.3}$$

By averaging over the reference level m, up to trivial scaling, this is the so-called LDoS $P(r = n - m)$.

For $x = 0$, it is trivial to see that $P(r) = \delta_{r,0}$, due to orthogonality. As x is increased, using standard first-order perturbation theory, one gets $P_{FOPT} \approx 1$ for $r = 0$, while

$$P_{FOPT}(r) = \frac{x^2 \left|\mathbf{B}_{nm}\right|^2}{(E_n - E_m)^2} = \frac{x^2 b^2}{\Delta^2 \left(b^2 + r^2\right) r^2} \quad \text{for } r \neq 0 \ , \tag{E.4}$$

where Δ is the mean level spacing. We have substituted the variance in Eq. (E.2) into the second equality. However, standard first-order perturbation theory is only valid up to some perturbation strength x_c, where x_c is the pertubation strength needed to mix neighboring levels only. We shall give an estimation of x_c later.

As x is increased beyond x_c, assuming the validity of infinite order perturbation theory, one can show that [110]

$$P_{PRT}(r) = \frac{x^2 \left|\mathbf{B}_{nm}\right|^2}{\Gamma^2 + (E_n - E_m)^2} = \frac{x^2 b^2}{\Delta^2 \left(b^2 + r^2\right) \left[(\Gamma/\Delta)^2 + r^2\right]}. \tag{E.5}$$

The energy scale Γ defines the region where a nonperturbative mixing of levels occurs. By imposing normalization of $P_{PRT}(r)$, we obtain

$$\Gamma = \frac{b\Delta}{2}\left[\sqrt{1 + \frac{4\pi x^2}{b\Delta^2}} - 1\right]. \tag{E.6}$$

For $\Gamma \ll \Delta$, as can been seen from Eq. (E.5), $P_{PRT}(r) \approx P_{FOPT}(r)$. Therefore, we can estimate x_c by requesting that $\Gamma(x_c) \approx \Delta$, thus arriving at

$$x_c \approx \frac{\Delta}{\sqrt{\pi}}\sqrt{1 + 1/b} \ . \tag{E.7}$$

To find an estimate for the perturbation strength x_{prt} up to which the $P_{PRT}(r)$ is valid, we compare the dispersion of $P_{PRT}(r)$

$$\delta E_{PRT} \equiv \Delta \times \sqrt{\sum_r r^2 P_{PRT}(r)} \tag{E.8}$$

with the dispersion of the actual LDoS

$$\delta E = x \sum_{n \neq m} \left|\mathbf{B}_{nm}\right|^2 \ . \tag{E.9}$$

We can approximate the sums above by integrals, and in particular for the WLRM model we obtain

$$\delta E_{PRT} \approx x\sqrt{\pi}b\,(b+\Gamma/\Delta)^{-1/2}\,, \tag{E.10}$$

and

$$\delta E \approx x\sqrt{2b}\,[\pi/2-\arctan(1/b)]^{1/2}\ . \tag{E.11}$$

The border x_{prt} is estimated as the point where $\delta E_{PRT}(x_{prt}) \approx \delta E(x_{prt})$, which leads to

$$x_{prt} \approx \Delta\sqrt{b}\frac{\sqrt{\pi-2\,[\pi/2-\arctan(1/b)]}}{2\,[\pi/2-\arctan(1/b)]}. \tag{E.12}$$

Appendix F

Two Limits of the Participation Ratio

We will approximate the participation ratio $\mathcal{PR}$ for the case of $\gamma = 0$ in the two extremes of Λ.

Firstly, in the strong nonlinearity regime, there are $\mathcal{O}(M)$ number of DB's and each site is effectively decoupled from other sites, so each site will retain the same density for all time. Since the initial condition is such that the distribution of density at each site follows a uniform distribution, at other times, one expects the density to follows a uniform distribution, i.e. $\mathcal{P}(y)$ is constant with $y = \psi_n$. We assume that y's are drawn from a uniform distribution and y runs from $-b$ to $+b$. Therefore,

$$\sum_{n=1}^{M} |\psi_n|^4 = M < |\psi_n|^4 >_n \approx M < |\psi_n|^4 >_{\psi_n} \tag{F.1}$$

In the second step, we assume that taking an average over all sites is approximately the same as taking an average over all possible ψ_n's.

Let us turn the right-hand side of the above equation into an integral,

$$M < |\psi|^4 >_\psi = M \int_{-b}^{b} |\psi|^4 P(\psi) d(\psi) = M \int_{-b}^{b} y^4 P(y) dy = \frac{M}{2b} \int_{-b}^{b} y^4 dy = \frac{M b^4}{5} \tag{F.2}$$

where we have used the fact that $P(y)$ is a uniform distribution and hence $P(y) = 1/2b$.

Applying the same technique for the normalization condition of the number of particles, we get

$$\sum_{n=1}^{M} |\psi_n|^2 = M < |\psi_n|^2 >_n \approx M < |\psi|^2 >_\psi = M \int_{-b}^{b} y^2 P(y) dy = \frac{M}{2b} \int_{-b}^{b} y^2 dy = \frac{Mb^2}{3} = 1 \tag{F.3}$$

which leads to $b = \sqrt{3/M}$. Thus, we obtain

$$M \sum_{n=1}^{M} |\psi_n|^4 \approx \frac{M^2 b^4}{5} = \frac{9}{5} \tag{F.4}$$

and the participation ratio is 5/9.

In the linear regime, we found that the distribution of atomic density follows an exponential distribution, corresponding to the fact that in a linear lattice it is exponentially less likely to find higher excitations. Let $P(x) = Ae^{-Bx}$ where $x = |\psi_n|^2$, and $B > 0$. We should now proceed to determine A and B.

We know that $\int_0^1 P(x)dx = 1$ from normalization of probabillity function. Then,

$$\int_0^1 P(x)dx = A \int_0^1 e^{-Bx} dx = 1 \Rightarrow A = B/(1 - e^{-B}) \tag{F.5}$$

Secondly, we apply the normalization condition for the total number of atoms

$$\sum_{n=1}^{M} |\psi_n|^2 = M < |\psi_n|^2 >_n \approx M < x >_x = M \int_0^1 xP(x)dx = 1 \tag{F.6}$$

But

$$M \int_0^1 xP(x)dx = MA \int_0^1 xe^{-Bx} dx = \frac{-MAe^{-B}}{B} + \frac{M}{B} \int_0^1 P(x)dx \tag{F.7}$$

Notice that the integral term on the right is equal to one, due to normalization of probability distribution. Setting the RHS equal to one and using Eq. (F.5) (i.e. $A = B/(1 - e^{-B})$) to substitue for A, we get

$$\frac{-MAe^{-B}}{B} + \frac{M}{B} = 1 \Rightarrow \frac{-Me^{-B}}{1 - e^{-B}} + \frac{M}{B} = 1 \tag{F.8}$$

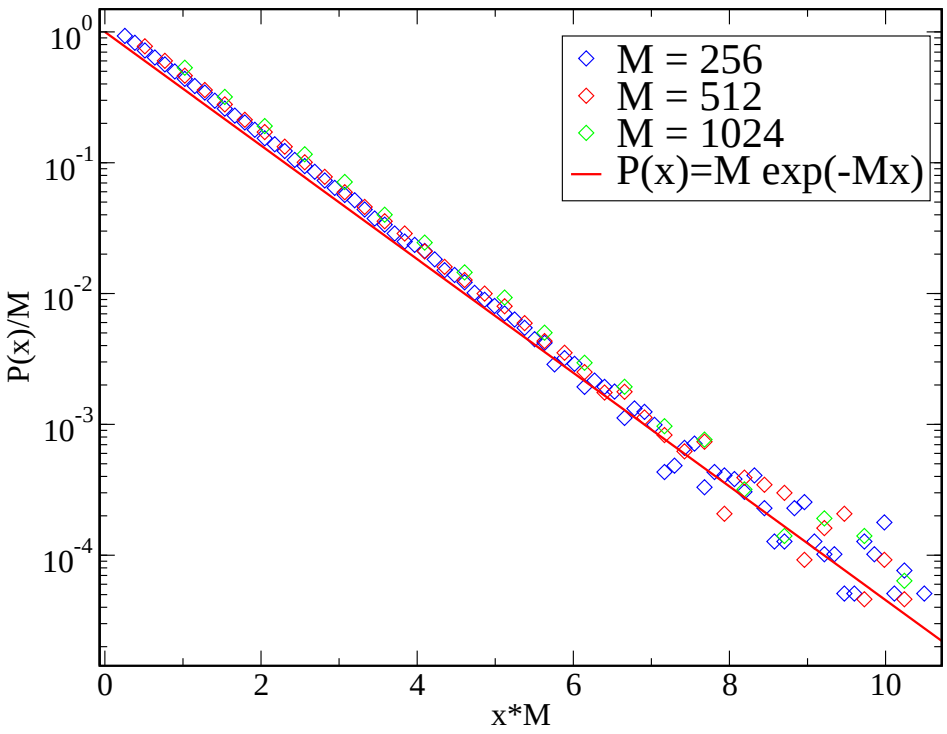

Figure F.1: Distribution of density in the linear regime (i.e. $\Lambda = 0$ and $\gamma = 0$). Here, $x = \psi_n$ and the diamonds are numerical results for different M's. We see excellent agreement between the numerical results and Eq. (F.9).

For $M \to \infty$, $e^{-M} \to 0$. Therefore $\frac{-Me^{-B}}{1-e^{-B}} \approx \frac{-M}{e^M} \to 0$ for $M \to \infty$. Since the first term goes to zero, we obtain $B = M$ as a solution in the thermodynamic limit. In fact, this turns out to be the only solution.

We then get $A = B/(1 - e^{-B}) = M/(1 - e^{-M})$. But $e^{-M} \to 0$ giving $A = M$, and thus

$$P(x) = Me^{-Mx}. \tag{F.9}$$

In fact, numerical results have verified Eq. (F.9) (see Fig. F.1).

To determine $\mathcal{PR}$,

$$\begin{aligned} M < |\psi|^4 >_\psi \approx M \int_0^1 x^2 P(x) dx &= M \int_0^1 x^2 M e^{-Mx} dx \\ &= -Me^{-M} + 2\left(\int_0^1 xMe^{-Mx} dx \right) \quad \text{(F.10)} \\ &= -Me^{-M} + 2\left(M \int_0^1 xP(x) dx \right) \quad \text{(F.11)} \\ & \quad \text{(F.12)} \end{aligned}$$

But the term in the bracket on the right is just the total density and is therefore equal to one, whereas the first term $-M/e^M \to 0$ when $M \to \infty$.

Hence, we have

$$\sum_{n=1}^{M} |\psi_n|^4 \approx M < |\psi|^4 >_\psi = 2 \quad \text{(F.13)}$$

leading to $\mathcal{PR} = \frac{1}{2}$.

Appendix G

Numerical Estimation of Distribution of Island Sizes

Here, we aim to verify the hypothesis that the sizes of islands of a typical Hamiltonian mixed phase space system follow a power-law distribution. This is done through numerical estimation of the distribution of island sizes in the kicked rotor (in the mixed phase space regime).

We consider a region $\mathcal{R}$ (see rectangular region in Fig. G.1) in the phase space of the kicked rotor containing an island (with its daughter islands) originating from a period 1 resonance [1]. We start two trajectories at random initial conditions $\mathbf{r}$ and $\mathbf{r}+\mathbf{s}$ within $\mathcal{R}$ separated by a distance $s = |\mathbf{s}|$. We follow the trajectories up to time T and proclaim a trajectory to be inside an island if it has not left the region $\mathcal{R}$, with less and less error with increasing T. Eventually, we want to take the limit of $T \to \infty$. The quantity we are going to study is

$p_{in,out}(s)$ = Probability that the first trajecteroy is inside an island and the second is not.

[1] For a period N resonance, we could do the same with the N-th iteration of the map.

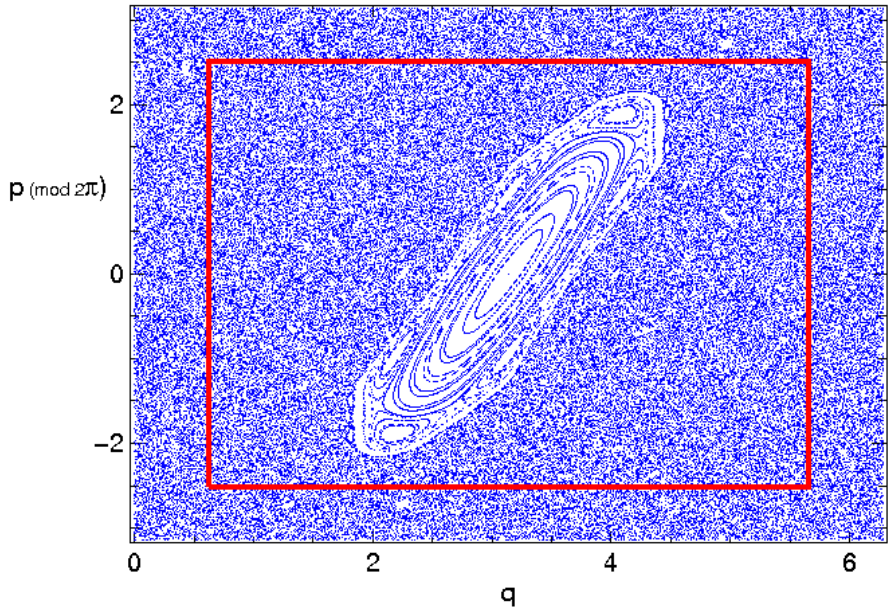

Figure G.1: Region $\mathcal{R}$.

This probes the circumferences of the islands and will help us to determine the distribution of island sizes.

Let $p_I(R)$ be the island size distribution that we are interested in, A_I the total area of islands in $\mathcal{R}$ and A the total area of $\mathcal{R}$. The probability of an arbitrarily chosen point to lie inside an island is $P(\text{in}) = A_I/A$, where $A_I = \int p_I(R)\pi R^2\, dR$.

The probability for a point known to be regular to lie inside an island of linear dimension R (e.g. maximum diameter) is given by

$$P(R|\text{in}) = \frac{p_I(R)\,\pi R^2}{A_I} \ .$$

Now let us start with a point r_0 that is inside an island of size R (see Fig. G.2a). It contributes to $P(R|\text{in})$ with

$$P(r_0, R|\text{in}) = \frac{p_I(R)}{A_I} \ .$$

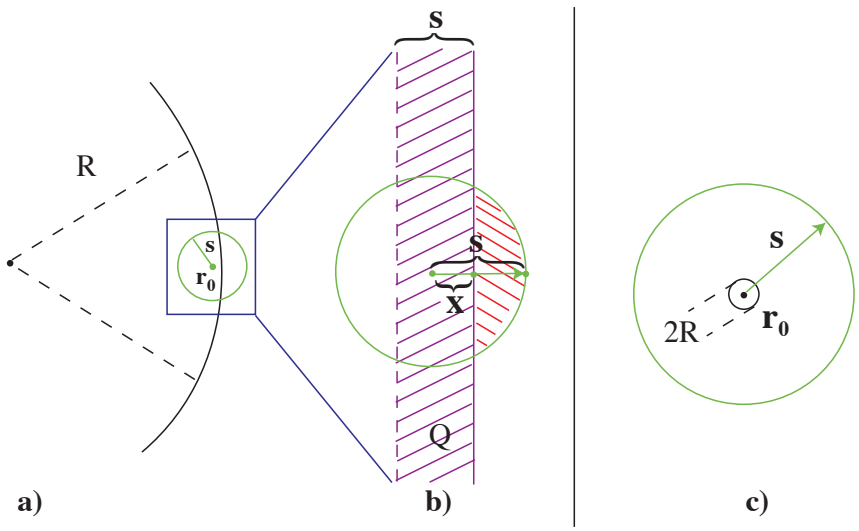

Figure G.2: Sketches for the two cases $R \gg s$ and $R \ll s$

We want to know what is the probability $P_{in,out}(s, R)$ that a point inside a neighborhood of radius s around r_0 lies outside the island, given that r_0 lies inside an island of size R.

First we deal with the case when $R \gg s$. If we approximate the island boundary by a straight line, the read shared area indicated in Fig. G.2b is the area that we are interested in. Thus, for a fixed r_0 in an island of size R, the fraction of area in its s-neighborhood that is outside the island is approximated by

$$P(s, out|r_0, R) = \frac{1}{\pi s^2} \begin{cases} 2\int_x^s \sqrt{s^2 - x'^2} dx' & \text{if } r_0 \in Q \\ 0 & \text{else.} \end{cases}$$

The only non-zero contributions come from the r_0's inside an island and are near the island boundary, i.e. $r_0 \in Q$.

We can thus write

$$\begin{aligned}
P_{in,out}(s,R) &= \iint\limits_{Island} P(r_0,R|\text{in})\,P(s,out|r_0R)d^2r_0 \\
&= \frac{p_I(R)}{A_I}\iint\limits_{Q}\int\limits_{x}^{s}\frac{2}{\pi s^2}\sqrt{s^2-x'^2}dx'd^2r_0 \\
&= \frac{p_I(R)}{A_I}\frac{2}{\pi s^2}\int\limits_{0}^{2\pi R}\int\limits_{0}^{s}\int\limits_{x}^{s}\sqrt{s^2-x'^2}dx'\,dx\,dy \\
&= \frac{p_I(R)}{A_I}\frac{4R}{s^2}\int\limits_{0}^{s}\frac{1}{4}\left(\pi s^2-2x\sqrt{s^2-x^2}-2s^2\arctan\frac{x}{\sqrt{s^2-x^2}}\right)dx \\
&= \frac{p_I(R)}{A_I}\frac{4R}{s^2}\,\frac{1}{4}\left[\pi s^2x+\frac{2}{3}\left(s^2-x^2\right)^{3/2}-2s^2\left(\sqrt{s^2-x^2}+x\arctan\frac{x}{\sqrt{s^2-x^2}}\right)\right]\Bigg|_0^s \\
&= \frac{p_I(R)}{A_I}\frac{4R}{s^2}\frac{s^3}{3}=\frac{4}{3A_I}R\,p_I(R)s\ \ (\text{for } R\gg s)
\end{aligned}$$

In the case of $R \ll s$, we have (see Fig. G.2c)

$$P(s,out|r_0,R)=\frac{\pi s^2-\pi R^2}{\pi s^2}.$$

And thus

$$\begin{aligned}
P_{in,out}(s,R) &= \iint\limits_{Island} P(r_0,R|\text{in})\,P(s,out|r_0R)d^2r_0 \\
&= \frac{p_I(R)}{A_I}\times\frac{s^2-R^2}{s^2}\times\iint\limits_{Island}d^2r_0 \\
&= \frac{\pi R^2}{A_I}p_I(R)\frac{s^2-R^2}{s^2} \\
&= \frac{\pi R^2}{A_I}p_I(R)\left(1-R^2/s^2\right)\ (\text{for } R\ll s).
\end{aligned}$$

In the numerics, we look at point that are on the perimeter of the s-neighborhood, thus we have the contributions from all island sizes, thus we have

$$p_{in,out}(s)=\int\limits_{0}^{R_{max}}\frac{d}{ds}P_{in,out}(s,R)\,dR.$$

Substituting

$$\frac{d}{ds}P_{in,out}(s,R) = \begin{cases} \frac{4}{3A_I} R\, p_I(R) & if\ s \ll R \\ \frac{2\pi R^4}{A_I} p_I(R) \frac{1}{s^3} & if\ s \gg R \end{cases}$$

and splitting the integral (thereby approximating the integral by its two limiting cases), we get

$$p_{in,out}(s) = \int_0^s \frac{2\pi R^4}{A_I} p_I(R) \frac{1}{s^3} dR + \int_s^{R_{max}} \frac{4}{3A_I} R\, p_I(R) dR.$$

We further assume that

$$p_I(R) = \beta\ R^{-\alpha} (\text{with } \alpha < 3),$$

where α is what we will numerically measure. We thus have

$$\begin{aligned} p_{in,out}(s) &= \frac{2\pi\beta}{A_I s^3} \int_0^s R^{4-\alpha} dR + \frac{4\beta}{3A_I} \int_s^{R_{max}} R^{1-\alpha} dR \\ &= \frac{2\pi\beta}{A_I s^3} \frac{s^{5-\alpha}}{5-\alpha} + \frac{4\beta}{3A_I(2-\alpha)} \left[R_{max}^{2-\alpha} - s^{2-\alpha} \right], \end{aligned}$$

and can thus be written in the form

$$p_{in,out}(s) = C_0 + C_1 s^{2-\alpha}. \tag{G.1}$$

Figure G.3 shows the numerical results for $p_{in.,out}(s)$ for three different maximal iteration times T with $K = 3.5$. The constant C_0 was first estimated by a linear fit and then subtracted. For increasing T, the curves fit better and better the form of Eq. (G.1). The numerical value for the exponent (for the largest time T) is $m \approx 0.58$. Thus, for the kicked rotor with $K = 3.5$, we have estimated a power-law distribution of island sizes with an exponent $\alpha = 2 - m = 1.42$.

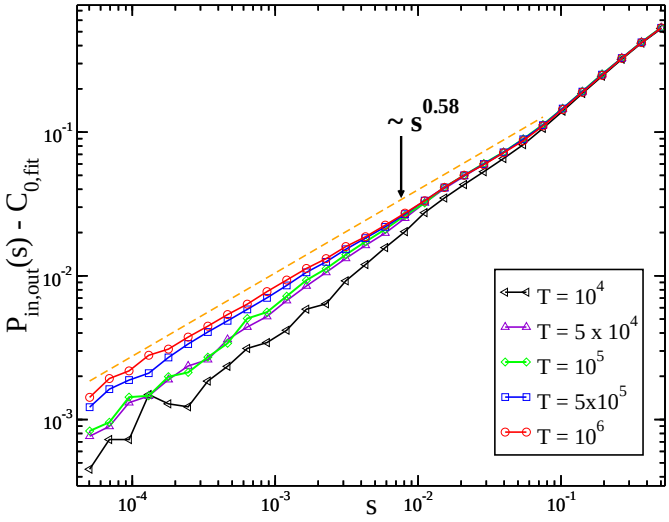

Figure G.3: Numerical estimation of the distribution of island sizes in the kicked rotor. We plot an estimate of the distribution of a measure of circumference of islands vs circumference width. The power-law here gives rise to a power-law distribution of island sizes with exponent $\alpha = 2 - m = 1.42$. The kicking strength $K = 3.5$.

Appendix H

Estimation of the Lower-bound of Λ^*

We will give an estimate for the lower-bound of the critical interaction strength Λ^*. We postulate that at $\Lambda = \Lambda^*$, the system self-organizes to create an optimum number of breathers so as to minimumize the energy.

Let the number of breathers $K < M$ (with $K > 0$) and for simplicity's sake, we assume that each breather is a δ-excitation. Let the typical density of these breathers be $X_b = \langle |\psi_n|^2 \rangle_K$, where the average is taken over K breathers in the system. Let X_s be the average density of the lattice, excluding these K breathers. Then, normalization condition is given by $KX_b + (M - K)X_s = 1$ and thus

$$X_s = \frac{1 - KX_b}{M - K} \tag{H.1}$$

With the above approximations, the Hamiltonian from Eq. (5.1) (with $\mu_n = 0$) then

reads

$$\begin{aligned} \mathcal{H} &= U\left(KX_b^2 + (M-K)X_s^2\right) - TX_s(M-K) \\ \tilde{H} \equiv 2\mathcal{H}/T &= \chi\left(KX_b^2 + (M-K)X_s^2\right) - 2X_s(M-K) \end{aligned} \tag{H.2}$$

Inserting X_s from Eq. (H.1) yields

$$\begin{aligned} \tilde{H} &= \chi\left(KX_b^2 + \frac{(1-KX_b)^2}{M-K}\right) - 2(1-KX_b) \\ &= X_b^2\frac{\chi MK}{M-K} + X_b\left(-\frac{2K\chi}{M-K} + 2K\right) + \frac{\chi}{M-K} - 2\ . \end{aligned}$$

Since the leading coefficient is positive, we seek the configuration of breathers (i.e. the value X_b) that minimizes the energy at $\frac{\partial \tilde{H}}{\partial X_b} = 0$. Simple differentiation gives

$$X_b^{H_{min}} = \frac{1}{M} - \frac{1}{\chi} + \frac{K}{\chi M} \tag{H.3}$$

For such configuration to exist, the condition $X_b \geq 0$ must be fulfilled, leading to

$$\begin{aligned} & 0 \leq X_b^{H_{min}} \\ \Rightarrow\ & 0 \leq \frac{1}{M} - \frac{1}{\chi} + \frac{K}{\chi M} \\ \Rightarrow\ & -K/M + 1 \leq \chi/M \\ \Rightarrow\ & -K/M + 1 \leq \Lambda \end{aligned} \tag{H.4}$$

where we recall that $\Lambda = \chi/M$.

We postulate that in the critical regime where $\Lambda = \Lambda^*$, this optimum configuration of breathers that minimizes the energy exists. Hence, in the thermodynamic limit where $M \gg K$, we have

$$\Lambda^* \geq 1. \tag{H.5}$$

Bibliography

[1] G. S. Ng, J. Bodyfelt, and T. Kottos, Phys. Rev. Lett. **97**, 256404 (2006).

[2] G. S. Ng and T. Kottos, Phys. Rev. B **75**, 205120 (2007).

[3] G. S. Ng, H. Hennig, R. Fleischmann, T. Kottos and T. Geisel (in preparation).

[4] H. J. Jensen, *Self-Organized Criticality* (Cambridge University Press, 1998).

[5] C. Kittel, *Introduction to Solid State Physics* (Wiley, 2004).

[6] P. W. Anderson, Phys. Rev. **109**, 1492 (1958).

[7] S. John, Phys. Rev. Lett. **53**, 2169 (1984).

[8] F. M. Izrailev, Phys. Rep. **196**, 299 (1990).

[9] D. Hennig, G. P. Tsironis, Phys. Rep. **307**, 333 (1999).

[10] M.I. Molina and G.P. Tsironis. Physica D **65** (1993).

[11] P. N. Butcher and D. Cotter, *The Elements of Nonlinear Optics* (Cambridge University Press, 1991).

[12] F. Dalfovo, S. Giorgini and L. P. Pitaevskii, Rev. Mod. Phys. **71**, 463 (1999).

[13] P. W. Anderson, Rev. Mod. Phys. **50**, 191 (1978).

[14] N. F. Mott and W. D. Twose, Adv. Phys. **10**,107 (1961).

[15] R. E. Borland, Proc. R. Soc. London Ser. A **274**, 529 (1963).

[16] E. Abrahams, P. W. Anderson, D. C. Licciardello, and T. V. Ramakrishnan, Phys. REv. Lett. **42**, 673 (1979).

[17] D. J. Thouless, Rep. Prog. Phys. **13**, 93 (1974).

[18] N. F. Mott, M. Pepper, S. Pollitt, R. H. Wallis and C. J. Adkins, Proc. Roy. Soc. London Ser. A **345**, 169 (1975).

[19] N. F. Mott and E. A. Davis, *Electronic Processes in Non-Crystalline Materials*, Clarendon Press, Oxford (1971).

[20] E. N. Economou and M. H. Cohen, Phys. Rev. B **5**, 2931 (1973).

[21] D. C. Licciardello and E. N. Economou, Phys. Rev. B **11**, 3697 (1975).

[22] P. A. Lee and T. V. Ramakrishnan, Rev. Mod. Phys. **57**, 287 (1985).

[23] B. Kramer and A. MacKinnon, Rep. Prog. Phys. **56**, 1469 (1993).

[24] E. N. Economou, *Green's functions in Quantum Physics* (Springer-Verlag, 1990).

[25] P. W. Anderson, Phil. Mag. B, **52**, 505 (1985).

[26] F. Scheffold, R. Lenke, R. Tweer, and G. Maret, Nature **398**, 206 (1999).

[27] D. S. Wiersma, P. Bartolini, A. Lagendijk, and R. Righini, Nature (London) **390**, 671 (1997).

[28] T. Schwartz, G. Bartal, S. Fishman, M. Segev, Nature **446**, 52 (2007).

[29] H. Cao, Y. G. Zhao, H. C. Ong, S. T. Ho, J. Y. Dai, J. Y. Wu, and R. P. H. Chang, Appl. Phys.Lett. **73**, 3656 (1998).

[30] H. Cao, Y. G. Zhao, S. T. Ho, E. W. Seelig, Q. H. Wang, R. P. H. Chang, Phys. Rev. Lett. **82**, 2278 (1999).

[31] V. Milner and A. Z. Genack, Phys. Rev. Lett. **94**, 073901 (2005).

[32] M. Wilson, Phys. Today **60**, 22 (2007).

[33] H. Furstenberg, Trans. Am. Math. Soc. **108**, 377 (1963)

[34] F. Delyon, Y. Levy and B. Souillard, J. Stat. Phys. **41**, 375 (1985); Phys. Rev. Lett., **55**, 618 (1985), and references therein.

[35] D. J. Thouless, J. Phys. C **5**, 77 (1972).

[36] P. Llyod, J. Phys. C **2**, 1717 (1969).

[37] A. M. Garcia-Garcia, and J. Wang, Phys. Rev. Lett. **94**, 244102 (2005).

[38] A. Furusaki, *Recent progress in the theory of Anderson localization*, Hong Kong Forum of Condensed Matter Phyiscs: Past, Present and Future (2006).

[39] E. Ott, *Chaos in Dynamical Systems* (Cambridge University Press, 1993).

[40] D. Braun, E. Hofstetter, G. Montambaux, and A. MacKinnon, Phys. Rev. B **64**, 155107 (2001).

[41] D. G. Polyakov, Phys. Rev. Lett. **81**, 4696 (1998).

[42] R. Ketzmerick, K. Kruse, S. Kraut, and T. Geisel, Phys. Rev. Lett. **79**, 1959 (1997).

[43] J. T. Chalker and G. J. Daniell, Phys. Rev. Lett. **61**, 593 (1988).

[44] J. T. Chalker, Physica (Amsterdam) **167A**, 253 (1990).

[45] B. Huckestein and R. Klesse, Phys. Rev. B **59**, 9714 (1999).

[46] J. A. Mendez-Bermudez and T. Kottos, Phys. Rev. B **72**, 064108 (2005).

[47] R. A. Jalabert and H. M. Pastawski, Phys. Rev. Lett. **86**, 2490 (2001); F. M. Cucchietti, H. M. Pastawski, and R. Jalabert, Physica (Amsterdam) **283A**, 285 (2000); F. M. Cucchietti, H. M. Pastawski, and D. A. Wisniacki, Phys. Rev. E **65**, 046209 (2002).

[48] Ph. Jacquod, I. Adagdeli, and C. W. J. Beenakker, Phys. Rev. Lett. **89**, 154103 (2002); Ph. Jacquod, P. G. Silvestrov, and C. W. J. Beenakker, Phys. Rev. E **64**, 055203(R) (2001).

[49] F. M. Cucchietti, C. H. Lewenkopf, E. R. Mucciolo, H. M. Pastawski, and R. O. Vallejos, Phys. Rev. E **65**, 046209 (2002).

[50] F. Haake, *Quantum Signature of Chaos* (Springer, 2001).

[51] Tsampikos Kottos and Uzy Smilansky, Phys. Rev. Lett. **79**, 4794 (1997); ibid. **85**, 968 (2000).

[52] S. Müller, S. Heusler, P. Braun, F. Haake and A. Altland, Phys. Rev. Lett. **93**, 014103 (2004).

[53] S. Heusler, S. Müller, A. Altland, P. Braun, and F. Haake, Phys. Rev. Lett. **98**, 044103 (2007).

[54] M. Sieber and K. Richter, Phys. Scr. **T90**, 128 (2001).

[55] F. L. Moore, J. C. Robinson, C. F. Bharucha, B. Sundaram, M. G. Raizen, Phys. Rev. Lett. **75**, 4598 (1995).

[56] W. H. Oskay, D. A. Steck, V. Milner, B. G. Klappauf and M. G. Raizen, Optics Communications **179**, 137 (2000).

[57] S. Fishman, D. R. Grempel, and R. E. Prange, Phys. Rev. Lett. **49**, 509 (1982); D. R. Grempel, R. E. Prange and S. Fishman, Phys. Rev. A **29**, 1639 (1984).

[58] Ya. B. Zeldovich, Sov. Phys. JETP **24**, 1006 (1967).

[59] F. M. Izrailev and D. L. Shepelyansky, Teor. Mat. Fiz. **43**, 417 (1980).

[60] H. Weyl, Math. Ann. **77**, 313 (1916).

[61] E. P. Wigner, Ann. Math. **62**, 548 (1955); ibid. **65**, 203 (1957).

[62] M.R. Zirnbauer, J. Math. Phys. **37**, 4989 (1996).

[63] H.-J. Stöckmann, *Quantum Chaos* (Cambridge University Press, 1998).

[64] K. Efetov, *Supersymmetry in Disorder and Chaos* (Cambridge University Press, 1996).

[65] B. I. Shklovskii, B. Shapiro, B. R. Sears, P. Lambrianides, and H. B. Shore, Phys. Rev. B **47**, 11487 (1993)

[66] B. L. Alt'shuler and B. I. Shklovskii, Zh. Eksp. Teor. Fiz. **91**, 220 (1986), Sov. Phys. JETP **64**, 127 (1986); D. Braun, G. Montambaux, and M. Pascaud, Phys. Rev. Lett. **81**, 1062 (1998).

[67] A. D. Mirlin, Y. V. Fyodorov, F.-M. Dittes, J. Quezada and T. H. Seligman, Phys. Rev. E **54**, 3221 (1996).

[68] D. K. Campbell, Nature **432**, 455 (2004).

[69] R. S. Mackay and S. Aubry, Nonlinearity **7**, 1623 (1994)

[70] D. K. Campbell, S. Flach, Y. S. Kivshar, Physics Today **57**, 43 (2004).

[71] S. V. Mingaleev, Y. S. Kivshar, Phys. Rev. Lett. **86**, 5474 (2001); J. W. Fleischer, M. Segev, N. K. Efremidis and D. N. Christodoulides, Nature **422**, 147 (2003); H. Martin, E. D. Eugenieva, Z. Chen and D. N. Christodoulides, Phys. Rev. Lett. **92**, 123902 (2004).

[72] S. Flach and C. R. Willis, Phys. Rep. **295**, 181 (1998); S. Flach, C. R. Willis, E. Olbrich, Phys. Rev. E **49**, 836 (1994).

[73] V. Kenkre and D. Campbell, Phys. Rev. B **34**, 4959 (1986).

[74] A. S. Davydov, J. Theor. Biol. **38**, 559 (1973); A. S. Davidov and N. I. Kislukha, Sov. Phys. JETP **44**, 571 (1976); Phys. Status Solidi B **59**, 465 (1973).

[75] D. N. Christodoulides and R. I. Joseph, Opt. Lett. **13**, 794 (1988); Phys. Rev. Lett. **62**, 1746 (1989); D. Mandelik, H. S. Eisenberg, Y. Silberberg, R. Morandott,

J. S. Aitchinson, ibid. **90**, 053902 (2003); F. Benvenuto et al., Phys. Rev. A **44**, R3423 (1991); D. L. Shepelyansky, Phys. Rev. Lett. **70**, 1787 (1993).

[76] A. Bader and L. Parker, *Joseph Loschmidt, Physicist and Chemist*, Physics Today **54(3)**, 45(2001).

[77] A. Peres, Phys. Rev. A **30**, 1610 (1984).

[78] M. Hiller, *Parametric Bose-Hubbard Hamiltonians: Quantum Dissipation, Irreversibility, and Pumping*, Ph. D.'s Thesis (2007).

[79] H. M. Pastawski, P. R. Levstein, G. Usaj, J. Raya and J. Hirschinger, Phys. Rev. Lett. **70**, 2936 (1993).

[80] R. Balian, *From Microphysics to Macrophysics* (Springer, 1991).

[81] W. H. Zurek, Phys. Today **44**, 36 (1991); D. Cohen and T. Kottos, Phys. Rev. E **69**, 055201(R) (2004); D. Cohen, Phys. Rev. E **65**, 026218 (2002).

[82] A. Stern, Y. Aharonov and Y. Imry, Phys. Rev. A **41**,3436 (1990).

[83] G. A. Fiete and E. J. Heller, Physical Review A **68**, 022112 (2003).

[84] M. A. Nielsen and I. L. Chuang, *Quantum Computation and Quantum Information* (Cambridge University Press,2000).

[85] T. Gorin, T. Prosen, T. H. Seligman, M. Znidaric, quant-ph/0607050 (2006).

[86] S. A. Gardiner, J. I. Cirac and P. Zoller, Phys. Rev. Lett. **79**, 4790 (1997).

[87] M. F. Andersen, A. Kaplan and N. Davidson, Phys. Rev. A **64**, 043801 (2001).

[88] S. Kuhr et al. Phys. Rev. Lett. **91**, 213002 (2003).

[89] R. Schafer et al., New J. Phys. **7**, 152 (2005).

[90] O. Lobkis and R. Weaver, Phys. Rev. Lett. **90**, 254302 (2003).

[91] Ph. Jacquod, I. Adagdeli and C. W. J. Beenakker, Phys. Rev. Lett. **89**, 154103 (2002); Ph. Jacquod, P. G. Silvestrov and C. W. J. Beenakker, Phys. Rev. E **64**, 055203(R) (2001).

[92] P. Jacquod, I. Adagideli and C. W. J. Beenakker, Europhys. Lett.**61**, 729 (2003).

[93] N. R. Cerruti and S. Tomsovic, Phys. Rev. Lett. **88**, 054103 (2002); J. Phys. A: Math. Gen. **36**, 3451 (2003).

[94] T. Gorin, T. Prosen, T. H. Seligman, New J. Phys. **6**, 20 (2004)

[95] T. Prosen, Phys. Rev. E **65**, 036208 (2002); T. Prosen and M. Znidaric, J. Phys. A: Math. Gen. **35**, 1455 (2002); ibid **34**, L681 (2001); T. Prosen and T. H. Seligman, ibid **35**, 4707 (2002); T. Kottos and D. Cohen, Europhys. Lett. **61**, 431 (2003).

[96] G. Benenti and G. Casati, Phys. Rev. E **66**, 066205 (2002); W. Wang and B. Li, ibid. **66**, 056208 (2002).

[97] D. A. Wisniacki and D. Cohen, Phys. Rev. E **66**, 046209 (2002).

[98] H. M. Pastawski, P. R. Levstein and G. Usaj, Phys. Rev. Lett. **75**, 4310 (1995).

[99] J. Vanicek and Eric J. Heller, quant-ph/0302192.

[100] F. M. Cucchietti, C. H. Lewenkopf, E. R. Mucciolo, H. M. Pastawski and R. O.Vallejos, Phys. Rev. E **65**, 046209 (2002).

[101] Y. Adamov, I. V. Gornyi and A. D. Mirlin, Phys. Rev. E **67**, 056217 (2003).

[102] A. D. Mirlin, Phys. Rep. **326**, 259 (2000); B. A. Muzykantskii and D. E. Khmelnitskii, Phys. Rev. B **51**, 5480 (1995); I. E. Smolyarenko and B. L. Altshuler, Phys. Rev. B **55**, 10451 (1997).

[103] V. E. Kravtsov and K. A. Muttalib, Phys. Rev. Lett. **79**, 1913 (1997); V. E. Kravtsov and A. M. Tsvelik, Phys. Rev. B **62**, 9888 (2000).

[104] F. Evers and A. D. Mirlin, Phys. Rev. Lett. **84**, 3690 (2000); E. Cuevas, M. Ortuno, V. Gasparian, and A. Perez-Garrido, ibid. **88**, 016401 (2002).

[105] I. Varga, Phys. Rev. B **66**, 094201 (2002); I. Varga and D. Braun, ibid. **61**, R11859 (2000).

[106] A. D. Mirlin, Y. V. Fyodorov, F.-M. Dittes, J. Quezada, and T. H. Seligman, Phys. Rev. E **54**, 3221 (1996).

[107] B. Huckenstein and R. Klesse, Phys. Rev. B **55**, R7303 (1997).

[108] J. T. Chalker, V. E. Kravtsov and I. V. Lerner, JETP Letters **64**, 386 (1996)

[109] A. D. Mirlin and F. Evers, Phys. Rev. B **62**,7920 (2000).

[110] J. A. Mendez-Bermudez, T. Kottos and D. Cohen, Phys. Rev. E **73**, 036204 (2006).

[111] J. Bodyfelt, expected Ph. D.'s Thesis (2009).

[112] R. Ketzmerick, K. Kruse, S. Kraut and T. Geisel, Phys. Rev. Lett. **79**, 1959 (1997).

[113] J. A. Mendez-Bermudez, unpublished.

[114] R. Peierls, Z. Phys. **80**, 763 (1933).

[115] D. Shechtman, I. Blech, D. Gratias, and J. W. Cahn, Phys. Rev. Lett. **53**, 1951 (1984); J. M. Luck and D. Petritis, J. Stat. Phys. **42**, 289 (1986); J. Bellisard, B. Iochum, E. Scoppola, and D. Testard, Comm. Math. Phys. **125**, 527 (1989).

[116] A. MacKinnon and B. Kramer, Rep. Prog. Phys. **56**, 1469 (1993).

[117] I. Guarneri, Europhys. Lett. **21**, 729 (1993); **10**, 95 (1989); I. Guarneri and G. Mantica, Phys. Rev. Lett. **73**, 3379 (1994); F. Piéchon, Phys. Rev. Lett. **76**, 4372 (1996).

[118] S. N. Evangelou and D. E. Katsanos, J. Phys. A: Math. Gen **26**, L1243 (1993).

[119] J. Zhong, R. B. Diener, D. A. Steck, W. H. Oskay, M. G. Raizen, E. W. Plummer, Z. Zhang, Q. Niu, Phys. Rev. Lett. **86**, 2485 (2001).

[120] A. S. Pikovsky and D. L. Shepelyansky, Phys. Rev. Lett. **100**, 094101 (2008).

[121] G. Kopidakis, S. Komineas, S. Flach and S. Aubry, Phys. Rev. Lett. **100**, 084103 (2008).

[122] St. Pnevmatikos, O. Yanovitskii, Th. Fraggis, E. N. Economou, Phys. Rev. Lett. **68**, 2370 (1992); E. N. Economou, O. Yanovitskii, Th. Fraggis, Phys. Rev. B **47**, 740 (1993).

[123] M. Johansson, M. Hörnquist, R. Riklund, Phys. Rev. B **52**, 231 (1995).

[124] P. G. Harper, Proc. Roy. Soc. London, Ser. A **68**, 874 (1955).

[125] S. Aubry, and G. Andre, Ann. Israel Phys. Soc. **3**, 133 (1980); J. B. Sokolov, Phys. Rep. **126**, 189 (1985).

[126] T. Geisel, R. Ketzmerick and G. Petschel, Phys. Rev. Lett. **66**, 1651 (1991).

[127] Y. Last, Commun. Math. Phys. **164**, 421 (1994).

[128] R. Ketzmerick, K. Kruse, F. Steinbach, and T. Geisel,Phys. Rev. B **58**, 988 (1998).

[129] D. R. Hofstadter, Phys. Rev. B **14**, 2239 (1976).

[130] T. Geisel, R. Ketzmerick and G. Petschel, in *Quantum Chaos: Between Order and Disorder*, edited by J. Casati and B. Chirikov (Cambridge University Press, Cambridge, 1995), pp. 634-659.

[131] S. N. Evangelou and J.-L. Pichard, Phys. Rev. Lett. **84**, 1643 (2000).

[132] M. Weiss, T. Kottos and T. Geisel, Phys. Rev. B, **63** 081306(R) (2001); F. M. Izrailev, T. Kottos, A. Politi and G. P. Tsironis, Phys. Rev. E **55**, 4951 (1997).

[133] P. Schlagheck, T. Paul, Phys. Rev. A **73**, 023619 (2006).

[134] V. M. Kenkre, D. K. Campbell, Phys. Rev. B **34**, 4959 (1985); V. M. Kenkre, G. P. Tsironis, Phys. Rev. B **35**, 1473 (1987); G. P. Tsironis and V. M. Kenkre, Phys. Lett. A **127**, 209 (1998).

[135] L. J. Bernstein, K. W. DeLong, N. Finlayson, Physics Letters A **181**, 135 (1993).

[136] M. I. Molina and G. P. Tsironis, Physica D **65**, 267 (1993); Int. J. Mod. Phys. B **9**, 1899 (1995).

[137] L. Hufnagel, R. Ketzmerick, T. Kottos and T. Geisel, Phys. Rev. E **64**, 012301 (2001).

[138] A. A. Gogolin, Sov. Phys. JETP, **44**, 1003 (1976).

[139] P. K. Datta, K. Kundu, Phys. Rev. B **53**, 14929 (1996).

[140] B. Lindquist, M. Johansson, R. Riklund, Phys. Rev. B **50**, 9860 (1994).

[141] P. K. Datta, A. M. Jayannavar, Phys. Rev. B **58**, 8170 (1998).

[142] Z. Pan, S. Xiong, C. Gong, Phys. Rev. E **56**, 4744 (1997).

[143] J. D. Andersen, V. M. Kenkre, Phys. Rev. B **47**, 11134 (1993).

[144] L. M. Kahn, K. Huang, D. L. Mills, Phys. Rev. B **39**, 12449 (1989); S. Dutta Gupta, D. S. Ray, Phys. Rev. B **38**, 3628 (1988); **40** 10604 (1989).

[145] D. Jaksch, P. Zoller, New Journal of Physics **5**, 56 (2003); R. B. Diener, G. A. Georgakis,J. Zhong, M. Raizen, Q. Niu, Phys. Rev. A **64**, 033416 (2001).

[146] B. P. Anderson, and M. A. Kasevich, Science **282**, 1686 (1998).

[147] D. Jaksch, C. Bruder, J. I. Cirac, C. W. Gardiner, P. Zoller, Phys. Rev. Lett. 81, 3108 (1998).

[148] C. Orzel, A. K. Tuchman, M. L. Fenselau, M. Yasuda, M. A. Kasevich, Science **291**, 2386 (2001).

[149] M. Greiner, O. Mandel, T. Esslinger, T. W. Hansch, I. Bloch, Nature **415**, 39 (2002).

[150] I. Bloch, Nature Phys. **1**, 23-30 (2005).

[151] F. S. Cataliotti, S. Burger, C. Fort, P. Maddaloni, F. Minardi, A. Trombettoni, A. Smerzi, M. Inguscio, Science **293**, 843 (2001).

[152] I. Carusotto and G. C. La Rocca, Phys. Rev. Lett. **84**, 399 (2000).

[153] J. E. Lye, L. Fallani, M. Modugno, D. S. Wiersma, C. Fort, M. Inguscio, Phys. Rev. Lett. **95**, 070401 (2005); C. Fort, L. Fallani, V. Guarrena, J. E. Lye, M. Modugno, D. S. Wiersma, M. Inguscio, Phys. Rev. Lett. **95**, 170410 (2005).

[154] T. Schulte, S. Drenkelforth, J. Kruse, W. Ertmer, J. Arlt, K. Sacha, J. Zakrzewski, M. Lewenstein, Phys. Rev. Lett. **95**, 170411 (2005).

[155] D. Clement, A. F. Varon, M. Hugbart, J. A. Retter, P. Bouyer, L. Sanchez-Palencia, D. M. Gangardt, G. V. Shlyapnikov, A. Aspect, Phys. Rev. Lett. **95**, 170409 (2005).

[156] B. Damski, J. Zakrzewski, L. Santos, P. Zoller, M. Lewenstein, Phys. Rev. Lett. **91**, 080403 (2003).

[157] M. Raizen, C. Salomon, Q. Niu, Phys. Today **50**, 30 (1997); D. S. Wiersma et al., Nature **390**, 671 (1997); K. W. Madison, et al., Phys. Rev. A **60**, R1767 (1999).

[158] N. Friedman et al., Phys. Rev. Lett. **86**, 1518 (2001); A. Kaplan et al., ibid. **87**, 274101 (2001); V. Milner et al., ibid. **86**, 1514 (2001).

[159] T. Baumert et al., Phys. Rev. Lett. **67**, 3753 (1991).

[160] G. Bacher et al., Phys. Rev. Lett. **83**, 4417 (1999); R. Kumar et al., ibid. **81**, 2578 (1998).

[161] A. A. Chabanov, et al., Phys. Rev. Lett. **90**, 203903 (2003); S. E. Skipetrov and B. A. van Tiggelen, ibid. **92**, 113901 (2004); L. Dal Negro et al., ibid. **90**, 055501 (2003); A. Z. Genack, et al., ibid., **82** 715 (1999).

[162] R. Livi, R. Franzosi and G-L Oppo, Phys. Rev. Lett. **97**, 060401 (2006).

[163] R. Franzosi, R. Livi, G-L. Oppo, J. Phys. B: At. Mol. Opt. Phys. **40**, 1195 (2007).

[164] I. Bloch, T. W. Hänsch, T. Esslinger, Phys. Rev. Lett. **82**, 3008 (1999); A. Öttl, S. Ritter, M. Köhl, and T. Esslinger, Phys. Rev. Lett. **95**, 090404 (2005).

[165] G. M. Moy, J. J. Hope, and C. M. Savage, Phys. Rev. A **59**, 667 (1999).

[166] B. I. Swanson, J. A. Brozik, S. P. Love, G. F. Strouse, A. P. Shreve, A. R. Bishop, W.-Z. Wang, and M. I. Salkola, Phys. Rev. Lett. **82**, 3288 (1999); N. K. Voulgarakis, G. Kalosakas, A. R. Bishop, and G. P. Tsironis, Phys. Rev. B **64**, 020301 (2001); K Kladko, J Malek and A R Bishop, J. Phys.: Condens. Matter **11**, L415 (1999).

[167] U. T. Schwarz, L. Q. English, and A. J. Sievers, Phys. Rev. Lett. 83, 223 (1999).

[168] E. Tras, J. J. Mazo, and T. P. Orlando, Phys. Rev. Lett. **84**, 741 (2000); L. M. Flora, J. L. Marn, P. J. Martnez, F. Falo and S. Aubry, Europhys. Lett. **36**, 539 (1996); A. V. Ustinov, Chaos **13**, 716 (2003).

[169] M. Sato, B. E. Hubbard, A. J. Sievers, B. Ilic, D. A. Czaplewski, and H. G. Craighead, Phys. Rev. Lett. **90**, 044102 (2003).

[170] H. S. Eisenberg, Y. Silberberg, R. Morandotti, A. R. Boyd, and J. S. Aitchison, Phys. Rev. Lett. **81**, 3383 (1998); R. Morandotti, U. Peschel, J. S. Aitchison, H. S. Eisenberg, and Y. Silberberg, Phys. Rev. Lett. **83**, 2726 (1999); D. N. Christodoulides and R. I. Joseph, Opt. Lett. **13**, 53 (1988); Yuri S. Kivshar, Opt. Lett. **18**, 1147 (1993).

[171] Jason W. Fleischer, Mordechai Segev, Nikolaos K. Efremidis, and Demetrios N. Christodoulides, Nature 422, **147** (2003); Serge F. Mingaleev and Yuri S. Kivshar, Phys. Rev. Lett. **86**, 5474 (2001).

[172] A. R. Bishop, G. Kalosakas, K. O. Rasmussen, Chaos **13**, 588 (2003).

[173] P. G. Kevrekidis, K. . Rasmussen, and A. R. Bishop, Int. J. Mod. Phys. B **15**, 2833 (2001).

[174] A. J. Sievers, S. Takeno, Phys. Rev. Lett. **61**, 970 (1988); S. Aubry, Physica D **103**, 201 (1997)

[175] G. P. Tsironis, S. Aubry, Phys. Rev. Lett. **77**, 5225 (1996); A. Bikaki, N. K. Voulgarakis, S. Aubry, G. P. Tsironis, Phys. Rev. E **59**, 1234 (1999).

[176] Y. S. Kivshar and D. K. Campbell, Phys. Rev. E **48**, 3077 (1993).

[177] B. Rumpf, Phys. Rev. E **70**, 016609 (2004).

[178] S. Flach and C. R. Willis, Phys. Rev. Lett. **72**, 1777 (1994).

[179] G. P. Tsironis, *Dynamical Studies of the Discrete Nonlinear Schrödinger Equation*, Series of Scientific Monographites (1994).

[180] G. S. Ng, C. West, T. Prozen, and T. Kottos, in progress (2008).

[181] S. M. Jensen, IEEE J. Quant. Electron. QE-**18** 1580 (1982).

[182] A. J. Leggett, Rev. Mod. Phys. **73**, 307 (2001).

[183] F. S. Cataliotti, L. Fallani, F. Ferlaino, C. Fort, P. Maddaloni and M. Inguscio, New J. Phys. **5**, 71 (2001);M. Greiner, O. Mandel, T. Esslinger, T. W. Hänsch and I. Bloch, Nature **415**, 39 (2002); C. Ozrel, A. K. Tuchman, M. L. Fenselau, M. Yasua and M. A. Kasevich, Science **291**, 2386 (2001); A. Trombettoni and A. Smerzi, Phys. Rev. Lett. **86**, 2353 (2001).

[184] D. Jaksch, C. Bruder, J. I. Cirac, C. W. Gardiner and P. Zoller, Phys. Rev. Lett. **81**, 3108 (1998); G. J. Milburn, J. Corney, E. M. Wright and D. F. Walls, Phys. Rev. A **55**, 4318 (1997).